Simulation of a search for the Standard Model Higgs boson in the $H \to ZZ \to 4e, 4\mu, 2e\,2\mu$ channels at the ATLAS experiment at LHC

Olav M. K. Mundal
University of Oslo
February 2005

Thesis presented for the Cand.Scient. degree
in Experimental Particle Physics

Abstract

The Higgs mechanism has been introduced in particle physics to generate the masses of the fundamental particles. Even though the realization of this mechanism in Nature is supported indirectly by several observations, the discovery of the Higgs boson itself has not been made. Such a discovery will be a crucial step in establishing this theoretical concept.

The channel $H \rightarrow ZZ \rightarrow 4l$ is one of the channels with the greatest discovery potential at the ATLAS at LHC if the Higgs mass is above $2m_Z$.

This thesis presents a simulation study of a Standard Model Higgs boson simulated with fast simulation of the detector. It is assumed that the Higgs boson has mass in the range 200 GeV-600 GeV and decays subsequently into two Z^0-bosons and four leptons.

The lineshape of the signal is studied for different masses of the Higgs boson and the background is studied when different cuts are applied. The significance is calculated for several Higgs masses by fitting the simulated signal+background histograms with appropriate functions and integrating this function in a certain mass window.

Acknowledgements

First of fall I want to thank my supervisor, Professor Lars Bugge for introducing me to the interesting field of Higgs physics and accepting me as his master student. During these one and a half years he has always been willing to answer my questions and to comment on my work.
Thanks also to the Group for Experimental Particle Physics for letting me attend conferences and going to CERN on several occasions.

The group of Experimental Particle Physics at the University of Oslo consists of many interesting persons. My fellow master students Robindra Prabhu, Marianne Johansen and Mustafa Hussain deserve special remark. Without them life would have been boring, and doing this master thesis would have been impossible. Your help, encouragement and sharing of frustrations have many times just been the kick to move on.
I also want to mention Børge Gjelsten, Sigve Haug, Samir Ferrag, Katarzyna Pajchel, Yurij Pylypchenko and Esben Lund who have helped me a lot and always been ready to answer my questions. Thank you!
My other friends at the Department of Physics should not be forgotten. Øystein Prytz, Annett Thøgersen, Ingvild Thue Jensen, Klaus Magnus Johansen, Margit Elisabet Dyrland and all the others who have contributed to making it such a cheerful time.

Bjarte Mohn and Ola Øye at the University of Bergen have also always been ready to answer questions about a variety of subjects and I am really grateful for their help. Many other people in the world of particle physics have also been to great help.

Finally, I express my thanks to my family; my sisters, my mother and Finn, and my father whose constant support and encouragement has been invaluable and helped me through many difficult times.

Contents

Chapter 1

Introduction

The idea that a basic simplicity governs the apparent complexity and diversity of the universe seems to have always been an important aspect of natural philosophy. Less evident is the realization of that idea in terms of irreducible elements as the fundamental building blocks of all matter, because equally plausible is the notion of an indefinitely divisible matter, conserving all of its properties at all levels of fragmentation.
It was probably the discovery of the atom and certainly the discovery of the electron and the proton that finally gave a decisive argument in favour of the concept of the fundamental constituents of matter or elementary particles. In any case, this constant search for order and simplicity has acted as a powerful driving force for progress in physics.

The history of the physics of the infinitely small is largely the history of the uncovering of successive layers of structure, each one a new microcosmos existing within older, less fundamental worlds. The notion of what constitutes an elementary particle in fact is not static, but evolves with time, changing in step with technological advances, or more precisely with the growth in the power of the sources of energy that become available to the experimenter. The higher the energy of the particle beam used to illuminate or probe the object under study is, the shorter are the wavelengths associated with the incoming particles and the finer the resolutions obtained in the measure. Thus, it is successively discovered that matter is built up from molecules; that the molecules are composed of atoms; the atoms of electrons and nuclei; and the nuclei of protons and neutrons. As the power of the modern particle accelerators keeps on increasing, it has become possible to accelerate particles to higher and higher velocities, to attain resolutions surpassing 10^{-16} centimeters and to observe more violent collisions between particles, which have revealed all the wonders of the subatomic universe, not only in the presence of ever finer structure levels, but also in the existence at every level of new particles of ever greater masses. Particle physics has become synonymous with high-energy physics.

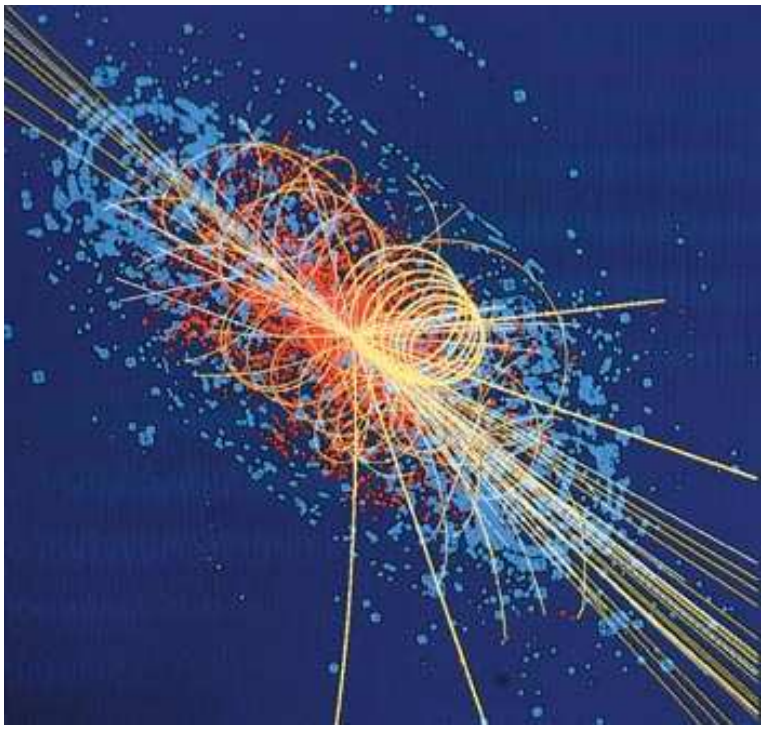

Figure 1.1: Simulated decay of a Higgs particle in the CMS detector, the other multi-purpose detector being built at CERN. From interactions.org

1.1 The standard Model

All known particle physics phenomena are very well described by the Standard Model of Particle Physics, from now on abbreviated SM.
The SM describes the elemenary particles and provides a theoretical framework for various phenomena, such as charge, interactions and mass, and has successfully passed very precise tests which at present are at the 0.1% level. However, the introduction of mass in SM is not yet fully understood, as we do not have experimental proof for the Higgs boson. We understand by elementary particles the point-like constituents of matter with no known substructure up to the present limits of $10^{-18} - 10^{-19} m$.

In the Standard Model, the elementary particles come in two types. Fermions, which are the very building blocks of nature and which all have spin $s = \frac{1}{2}$, and the kind of particles that are intermediate interaction particles and all have $s = 1$ (gauge bosons). In addition there is the Higgs boson with $s = 0$.

1.1.1 The fermions

The fermions come in two forms: leptons and quarks.
There are six different leptons, the most famous being the electron. The other charged leptons are the muon and the tau. The leptons are divided into three dublets: each

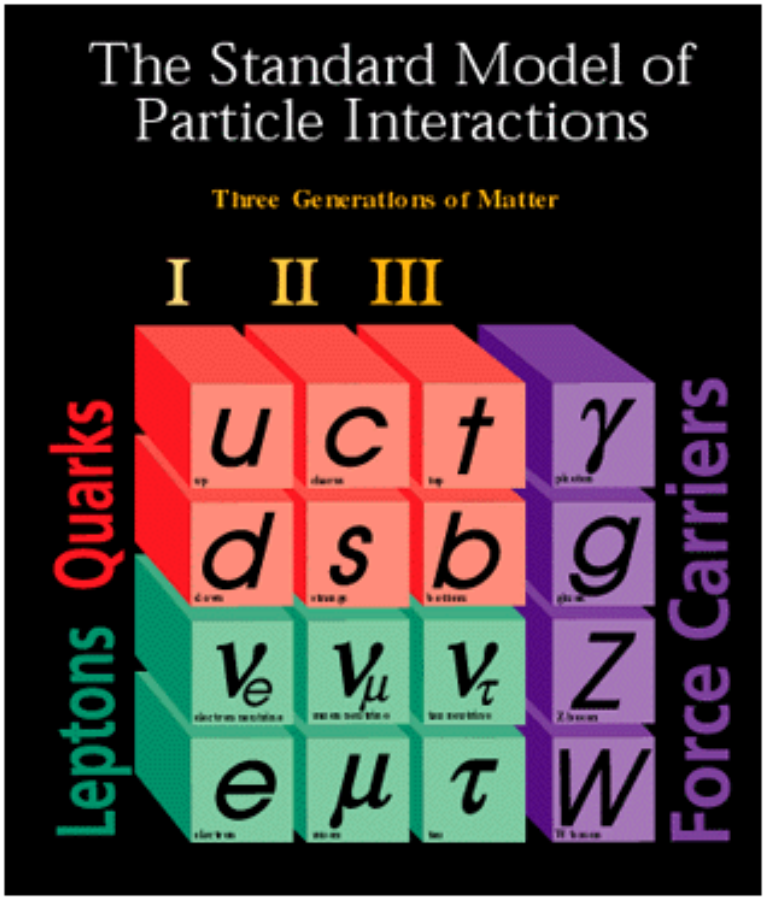

Figure 1.2: The different particles in the standard model. The quarks and leptons have half integer spin, while the gauge bosons on the right side all have spin one. From www.fnal.gov/pub/ inquiring/physics/theory/

consisting of the charged lepton and its associated neutral neutrino.

$$\begin{pmatrix} \nu_e \\ e \end{pmatrix}, \begin{pmatrix} \nu_\mu \\ \mu \end{pmatrix}, \begin{pmatrix} \nu_\tau \\ \tau \end{pmatrix}$$

Each family also has a family with anti-leptons. To each lepton family we associate a lepton number which is very nearly conserved in all known interactions. The charged lepton and the corresponding neutrino have the same lepton number.

There are six quarks, too, and they are also divided into three families.

$$\begin{pmatrix} u \\ d \end{pmatrix}, \begin{pmatrix} c \\ s \end{pmatrix}, \begin{pmatrix} t \\ b \end{pmatrix}$$

The quarks have an additional quantum number, the colour, and there is strong evidence for the number of colours being equal to three. However, we only see colourless particles, colour singlets. This leads to the hypothesis of colour confinement: all particles in nature are colourless. Coloured particles, quarks and gluons can only exist in bound states. The ALICE experiment at LHC will try to explore the phenomenon of colour confinement which we do not understand and are unable to derive from first principles. Particles built from quarks and gluons are referred to as hadrons, of which there are two types: mesons ($q\overline{q}$) and baryons (qqq). [1]

1.1.2 The bosons

We are able to identify four fundamental forces in nature.

- The electromagnetic force, which is successfully described by QED.
- The strong force, which is the force between quarks.
- The weak force, which governs the properties of decaying particles, such as the beta decay of the neutron.
- The gravitational force, which is described classically by Einstein's general theory of relativity. The SM does not include gravity and compared to the other forces, gravity is extremely weak.

In the SM all these forces are mediated by the exchange of a forcecarrier and the second kind of elementary particles are these intermediate interaction particles.[2] The photon, γ, is the exchanged particle in the electromagnetic interactions, the eight gluons g_α; $\alpha = 1, .., 8$ mediate the strong interactions among quarks, and the three weak

[1] Particles consisting of for example four quarks and one anti-quark are not excluded in SM and there is some experimental evidence for the existence of the socalled *pentaquarks*.

[2] No experimental evidence have been found in support for a forcecarrier for gravity. These supposed particles are called *gravitons*.

bosons, W^+, W^-, Z^0 are the corresponding intermediate bosons of the weak interactions.

The range of theese interactions goes from very short to infinite. The range of the electromagnetic interaction is infinite as it corresponds to an interaction mediated by a massless gauge boson.
The range of the weak interactions is very short, about 10^{-16} cm, due to the exchange of very massive gauge particles, the $W^{\pm}$ and Z^0 and, finally, the strong interactions whose range is not infinite, as one mayby would think since the gluons are massless, but finite due to the extra physical property of colour confinement.

Regarding the strength of the three interactons, the electromagnetic interactions are governed by the size of the electromagnetic coupling constant e, or equivalently $\alpha = \frac{e^2}{4\pi}$ which at low energies is given by the fine structure constant, $\alpha(Q = m_e) = \frac{1}{137}$.
The weak interactions at energies much lower than the exchanged gauge boson mass, M_V, have an effective strength given by the Fermi constant $G_F = 1.167 \times 10^{-5} GeV^{-2}$.
The name of strong interactions is due to their comparative stronger strength than the other interactions. This strength is governed by the size of the strong coupling constant g_S or equivalently $\alpha_S = \frac{g_s^2}{4\pi}$ and it varies from large values at low energies to the vanishing asymptotic limit $\alpha_S(Q \to \infty) \to 0$. This last limit indicates that the quarks behave as free particles when they are observed at infinitely large energies or, equivalently, at infinitely short distances. This is known as the phenomenon of asymptotic freedom.
The charge in QED is the familiar electrical charge which the photon couples to. The photon itself carry no electrical charge and self interaction between photons is therefore not possible. For the strong interactions, however, the situation is different. The gluons themselves carry the strong charge, which is the colour. This allows the gluons to interact with other gluons and this gives rise to phenomena not allowed by QED, for example four jet events where a gluon has splitted into two gluons.

1.1.3 The concept of force and The Gauge bosons

The SM is a quantum field theory where particles exist as excitations of fields.
The concept of a field was originally introduced in classical physics to account for the interaction between two bodies separated by a finite distance. In classical physics the electric field $E(x,t)$, for instance, is a three-component function defined at each space-time point, and the interaction between two charged bodies, 1 and 2, is to be viewed as the interaction of body 2 with the electric field created by body 1.
In the quantum theory, however, the field concept acquires a new dimension. As originally formulated in the late 1920's and the early 1930's, the basic idea of quantum field theory is that we associate particles with fields such as the electromagnetic field. Quantum mechanical excitations of a field appear as particles of definite mass and spin. The requirements imposed by quantum field theory, when combined with other general principles such as Lorentz invariance and the probabilistic interpretation of state vectors, severely restrict the class of particles that are permitted to exist in nature:

- For every charged particle there must exist an antiparticle with opposite charge

and with the same mass and lifetime.

- The particles that occur in nature must obey the spin-statistics theorem which states that half-integer spin particles must obey Fermi-Dirac statistics, whereas integer spin particles must obey Bose-Einstein statistics.

We have mentioned that particles are quantizations of fields and indicated that when some force acts between particles, the force is mediated by one of the forcecarriers, one of the gauge bosons.
These fields are introduced in the theory when we impose the demand of local gauge symmetry. When performing an arbitrary local phase transformation of for example a Lagrangian density, the physics should not change. This means that the equations should look the same in different frames connected by a Lorentz transformation. In order to do this, we have to introduce a gauge field. This is done by substituting the ordinary derivative by a modified derivative. These new gauge fields, or interaction fields, give rise to the gauge bosons which act as force carriers.

It is a fact that several areas of common ground are shared by the electromagnetic and weak interactions and the likeness between the treatments of the two interactions encourage the view that the two theories may have a common origin in a single body of principles. Despite the apparant differences in range and strength it has been shown that these two forces are different manifestations of a single unified interaction.
The unified theory of the electroweak interaction is a renormalizable quantum field theory in which the interactions of quarks and leptons are mediated by a unified electroweak field having four charge-specific degrees of freedom. Four different charge-bearing quanta are associated with this generalized field. The quanta W^+, W^-, W^0 and B^0 are required to be massless particles. Two of these quanta become the known W^+ and W^-. The remaining two are neutral and can therefore be mixed in a various combined states. The couplings to the electromagnetic currents of quarks and leptons select a particular combination of B^0 and W^0 for identification as the photon

$$\gamma = B^0 cos\,\theta_w + W^0 sin\,\theta_w \tag{1.1}$$

This is a rotation defined by the weak mixing angle θ_w, a parameter of the theory to be determined by experiment. Another rotated combination of B^0 and W^0, orthogonal to γ, identifies another neutral entity:

$$Z = -B^0 sin\,\theta_w + W^0 cos\,\theta_w \tag{1.2}$$

The Z^0 is referred to as the neutral current while the $W^\pm$ are referred to as charged currents. One of the two vital ingredients of the electroweak theory is the principle by which the quanta are introduced originally as massless particles. The other is the mechanism by which the weak quanta and other particles that should have mass acquire mass. The first principle is local gauge invariance and the latter is sponataneous symmetry breaking.

Conservation laws and symmetry principles are very important in physics. According to

Noether's theorem there is a conserved quantity to every symmetry principle. We separate between internal symmetries and space-time symmetries. Examples of space-time symmetries are Lorentz invariance, translational invariance and rotational invariance. Each of these give rise to a conserved quantity. Internal symmetries are symmetries that act not in the physical space but in an internal space. For example $SU(3)$ colour symmetry is an internal symmetry. Another example is if the Lagrangian is invariant under a global phase transformation, electrical charge is conserved.
If a local type of conservation law is allowed, as previously commented on, the system is forced to include a mediating field whose response to the symmetry operation is such as to compensate for the variation of the symmetry from point to point. This field enables the local symmetry to propagate through the system and provide a mechanism for interaction. This is Gauge symmetry.

1.2 The Need to Understand Mass

As was briefly mentioned above, the SM introduces the concept of mass in a way that predicts the existence of a particle, the Higgs boson, which so far has escaped experimental observation.

In the sixties, the Scottish physicist Peter Higgs came up with a model in which particle masses arise in a beautiful, but complex progression. He starts with a particle that has only mass, and no other characteristics, such as charge, that distinguish particles from empty space. We call this particle H. H interacts with other particles; for example if H is near an electron, there is a force between the two.

In the mathematics of quantum mechanics describing creation and annihilation of elementary particles, as observed at accelerators, particles at particular points arise from fields spread over space and time. Higgs found that parameters in the equations for the field associated with the particle H can be chosen in such a way that the lowest energy state of that field is one with the field not zero. It is surprising that the field is not zero in empty space, and the result is: all particles that can interact with H gain mass from the interaction.

Thus mathematics links the existence of H to a contribution to the mass of all particles with which H interacts. A picture that corresponds to the mathematics is of the lowest energy state, empty space, having H particles with no energy on their own. Other particles get their masses by interacting with this collection of zero-energy H particles. The mass (or inertia or resistance to change in motion) of a particle comes from its being grabbed at by Higgs particles when we try and move it.

If particles do get their masses from interacting with the empty space Higgs field, then the Higgs particle must exist; but we can't be certain without finding the Higgs. We have other hints about the Higgs; for example, if it exists, it plays a role in unifying different forces. However, we believe that nature could contrive to get the results that

would flow from the Higgs in other ways. In fact, proving the Higgs particle does not exist would be scientifically every bit as valuable as proving it does.

1.3 New physics at LHC

Although this report mainly will be concerned with the search for the Higgs boson, the existence of this particle is not the only field of interest at the new LHC accelerator.

In chapter two, the most important features of the LHC accelerator and the ATLAS detector will be discussed. For now, it will be discussed what we are hoping to see at LHC when it starts taking data.

An LHC experiment must have the ability to find the unexpected. New phenomena of whatever type will decay into the particles of the standard model. In order to meet all the requirements of the physics goals, the detector must have great flexibility. The varied physics signatures for these processes require the ability to reconstruct and measure final states involving the following

- Charged leptons including the tau
- The electroweak gauge bosons W, Z and γ.
- Jets coming from the production at high transverse momentum of quarks and gluons.
- Jets that have b-quarks within them.
- Missing transverse energy carried off by weakly interacting neutral particles such as neutrinos.

Four large-scale experiments will be running at the LHC. ATLAS and CMS are the two multipurpose detectors for pp collisions while LHCb will be looking into the physics of B-hadrons. ALICE is a heavy-ion experiment which will study the behaviour of nuclear matter at high densities and energies. There are strong physics motivations behind the LHC, [22]:

- The origin of particle masses. Despite the success of the Standard Model, the origin of particle masses and hierarchy of leptons, quarks and gauge bosons is still troublesome. A way to break the electroweak symmetry in the SM was provided in the late sixties by Peter Higgs, and the mechanism (referred to as the Higgs mechanism) gives particles their mass. A direct consequence of this mechanism is the existence of a scalar particle, called the Higgs boson, [8]. The theory does not specify the mass of the Higgs boson itself, but it should not exceed 1 TeV to preserve unitarity at high energies. This particle has not been found yet, and LHC is designed to search for it over the entire energy range.

- Physics beyond the Standard Model. Even though the Higgs mechanism provides a way to endow particles with mass it has little physical justification. Indeed there are several reasons to believe that the Standard Model is not the ultimate theory. The LHC is meant also to look into possible physics beyond the SM, and the detectors will search for manifestations of theories that predict new physics at an energy accessible for LHC. These theories include searches for Supersymmetry, Black Holes, extra dimensions, Gravitons.

- Open questions. The high energy range of the LHC allows for testing open questions like for example: are quarks and leptons really fundamental? Could it be more than three families of quarks and leptons? Why is there an asymmetry between matter and antimatter in the universe?

- Precision measurements. Another way to check the Standard Model is to perform precision measurements on its predictions. Any deviations from the theory would be a sign for new physics. At the LHC, known particles like W and Z bosons, top and b-quarks will be produced in huge quantities enabling precise measurements on for example Triple Gauge Couplings and the strong coupling constant.

The experimental observation of one or several Higgs bosons at LHC will be fundamental for a better understanding of the mechanism of electroweak symmetry-breaking. In the Standard Model, one doublet of scalar fields is assumed which leads to the existence of one neutral scalar particle, H, the Higgs boson. On the basis of present theoretical knowledge, the Higgs sector in the Standard Model remains largely unconstrained. The Higgs-boson mass, m_H, is not theoretically predicted. However, from unitary arguments an upper limit of 1TeV can be derived. Requirements of the stability of the electroweak vacuum and the perturbative validity of the Standard Model allows to set upper and lower bounds depending on the cutoff value chosen for the energy scale Λ up to which the Standard Model is assumed to be valid. Experimentally, constraints on the Standard Model Higgs-boson mass are derived directly from searches at LEP2. [7]

1.4 Beyond the standard model

It is appropriate to briefly mention what scenarios beyond the Standard Model one might face when the LHC starts. The discussian here is mostly based on [5], [18] and [20].
The success of the standard model of strong, weak and electromagnetic interactions has drawn increased attention to its limitations and the theory is considered not as a fundamental theory but merely as an efficient low energy approach to more fundamental theories. We will briefly comment on the questions left unanswered by the SM:

- The Hierarchy Problem: Loop corrections to the Higgs mass is of the order up to the energy scale the SM is considered valid. This mixing of energy scales (the electroweak and the GUT scale) is called 'The Hierarcy Problem'. The divergence in the perturbation series is quadratic in the cutoff Λ (the scale at which new

physics should appear), while other divergences in the SM are only proportional to log Λ. Finetuning is a solution to this problem, but it does not seem very likely. The reason is that Finetuning implies that the difference of two squared masses of order 10^{15} GeV each should be of order the mass of the W boson squared, in which case one keeps the Higgs boson mass at a reasonable level.

- The SM contains 19 unpredicted parameters, which is considered a bit unaestethic. In its simplest version, the model has 19 parameters, the three coupling constants of the gauge theory $SU(3) \times SU(2) \times U(1)$, three lepton [3] and six quark masses, the mass of the Z boson which sets the scale of weak interactions, the four parameters which describes the rotation from the weak to the mass eigenstates of the charge $-\frac{1}{3}$ quarks (CKM matrix). All of these parameters are determined with varying errors. Of the two remaining, one, a CP violating parameter associated with the strong interactions, must be very small. The last parameter is associated with the mechanism responsible for the breakdown of the electroweak $SU(2) \times U(1)$ to $U(1)_{em}$. This can be taken as the mass of the Higgs boson. The couplings of the Higgs boson are determined once its mass is given.

- There is an asymmetry between matter and anti-matter in the universe.

- Why are there exactly three generations of fermions? And what is the origin of the mixing between the quarks, parametrized by the CKM matrix?

- What is the nature of QCD confinement?

- Do the leptons and quarks have a finer substructure?

- Is it possible to unify the strong and electroweak force and describe them all with one coupling constant at higher energies? In that case, one cannot distinguish between the forces and the three forces have melted into one force.

1.4.1 Different SM extensions

Despite the immense success of the SM the model can not be totally correct. Although the theory is in very precise agreement with experiments at the energy levels accessible so far, it is not believed that the SM can be extrapolated to higher energies and that the SM is only an effective theory working well at lower energies. Instead of rejecting the theory, however, one wants to extend the theory to cope with the problems mentioned above.

GUT models

GUT models (Grand Unified Theories) aim to describe three of the four forces in one single framework by the same parameters. Gravity is left out. At very high energies,

[3] The neutrinos are now believed to have a non-vanishing mass which gives three additional mass parameters.

the so-called GUT scale, M_{GUT} $10^{15} - 10^{16}$ GeV; the three coupling constants meet at one value if SUSY is invoked.
There are many problems with these GUT theories, and perhaps the most serious problem is that it predicts the existence of magnetic monopoles which are not observed, [18]

Super Symmetry

Supersymmetry is the most extensively considered SM extension and it implies phenomenologically that for every boson (fermion) in the model, there exists a fermion (boson) partner with exactly the same mass and quantum numbers, except that the spin is changed by $\pm\frac{1}{2}$.
Supersymmetry solves the hierarchy problem and only requires $|m^2_{sparticle} - m^2_{particle}| \leq 1\,TeV^2$. [18] When superpartners to all SM particles are introduced, each term in the perturbation series will be cancelled by an opposite sign term due to the new superpartners.

SUSY introduces many new particles. All the supersymmetric partners of hte original bosons are called the same as the boson, only that the suffix '-on' is replaced by '-ino', so *gluon* becomes *gluino*. The superpartners of the fermions are called hte same as their partners except that an 's' is added in the front so *quarks* become *squarks*.
Supersymmetric particles come in addition to the SM paricles:

- Three generations of spin zero squark singlets and doublets
- Three generations spin zero slepton singlets and doublets
- Two spin $\frac{1}{2}$ Higgsino doublets
- Three spin $\frac{1}{2}$ winos
- One spin $\frac{1}{2}$ bino and eight gluinos

When the electroweak symmetry is broken, the gauginos (winos and binos) mix with the Higgsinos to form neutralinos ($\overline{\chi_i^0}$) and two charginos ($\overline{\chi_i^\pm}$).
There is, however, a catch. The most general SUSY Lagrangian is not in agreement with experiments since it contains renormalizable Lepton and Baryon number violating interactions, [20]. One has tried to detect proton decay, for example, without success. In order to save the day, one introduces a discrete symmetry, $R-$ parity, under which the Lagrangian is required to be invariant. Without going into details, this saves the proton. In addition, a dark matter candidate is introduced. The decay chain of any sparticle ends with an LSP (lightest supersymmetric particle) which is stable.

Technicolour Models

Technicolour is an alternative way to break electroweak symmetry. By introducing a universal $SU(3)$ interaction at high energies, the particles in the SM acquire mass without violating the gauge invariance of the Lagrangian. There is no need for a Higgs particle and the hierarchy problem does not exist.

New gaugebosons

An important question is wether there are any new gauge bosons beyond the ones associated with the $SU(3)_C \times SU(2)_W \times U(1)_Y$ gauge group. New gauge bosons are predicted within many theories beyond the SM.
The simplest way of extending the SM gauge structure is to include a second U(1) group. The associated gauge boson, labelled $Z^{'}$, is a spin 1 particle with no electrical charge. If the new gauge coupling is not much smaller than unity, then the U(1) group must be spontaneously broken at a scale larger than the electroweak scale in order to account for the nonobservation of $Z^{'}$ at LEP and run one at Tevatron.

Radions

It is a serious problem of modern physics that the general theory of relativity and quantum mechanics not have been unified into one theory. In these attempts, theories with more than three spatial dimensions are introduced. In string theory, for example, there can be as many as nine spatial dimensions.
In string theory, fundamental particles are replaced by one-dimensional 'superstrings'. Different SM particles appear as different oscillations of the string. The extra dimensions are very small and are curled together which explains their invisibilaty. They can not be seen at scales larger than the Planck length 10^{-35} m, which is far out of reach of what is experimentally measurable. [4]

One of the biggest problem with unifying the force of gravity with the other three forces is the weakness of gravity compared to the other forces. The weak scale is of order 10^3 GeV and the scale of gravity, the Planck scale is of order 10^{19} GeV. [5]
An alternative scenario to string theory are the socalled ADD-scenario and the Randall Sundrum Scenario. In these theories space-time and the Planck scale are itself changed. We have very little knowledge of how gravity acts at small distances. It could be that gravity propagates into extra dimensions, for example, but this might not be possible for the other forces.
In the Randall Sundrum scenario there is one extra spatial dimension which is compactified [5]. In the formalism, a geometrical exponential factor is introduced and the stabilization of the compactification radius is crucial.
A way to solve this is to introduce a bulk [6]scalar field with interactions localized on the

[4] At LEP the limit was pushed down to 10^{-19} m.
[5] Compactification: that the extra dimensions curl up and become extremely small.
[6] A bulk field is a field that propagates in all dimensions.

two branes [7] that can generate the required potential to stabilize the scalar field. As a consequence the quantum of the modulus field acquires mass and the massive scalar particle associated with it is denoted the radion, ϕ.
The radion is expected to be light and could be found at the LHC. Its coupling to fermions and gauge bosons is related to that of the SM Higgs through a rescaling of the Higgs couplings. The radion might also mix with the Higgs. The radions are produced mainly by the gluon-gluon fusion process, and the cross section is about 100 times larger than for the Higgs boson and the Higgs and the radion have nearly the same decay channels. If the radion is somewhat heavier than the Higgs, it might decay into two Higgs bosons.
Since the radions and the Higgs look so much alike with similar characteristics and interactions it is of crucial importance to be able to distinguish between them.

[7] Brane: generalization of a membrane into higher dimensions. A p-brane has (p+1) dimensions

Chapter 2

The ATLAS detector

In this chapter the most important features of the ATLAS detector will be discussed and the emphasis will be on the parts of the detector which are relevant for the channel studied in this project. This implies that the Inner Detector (ID), the electro-magnetic calorimeter and the muon chambers will be most thoroughly discussed.

The ATLAS detector is a general-purpose detector designed to exploit the full physics potential at the LHC accelerator at CERN which will start in 2007. The 45 metre long ATLAS detector is one of the largest and most elaborate particle physics experiments ever designed.
At LHC the colliding particles collide head-on in colliding beams so the shape of the detector is cylindrical. The detector is conveniently separated in a barrel part and end cap parts at the ends.

2.1 LHC

The Large Hadron Collidor (LHC) is a proton-proton collider with 14 TeV centre of mass energy. However, as protons are composite objects, the hard collision does not involve the full momentum of the protons. The partons (quarks and gluons) that make up the proton, each carry a fraction of the proton momentum. Effectively, the maximum energy that becomes available in the collision is therefore $\sqrt{x_1 x_2 s}$, where x_1 and x_2 are the momentum fraction carried by both partons.
The design luminosity for the LHC is $\mathcal{L} = 10^{34} cm^{-2} s^{-1}$. It is a two-ring accelerator and collider, and it is installed in the 27 km long tunnel originally used for the LEP electron positron collider.
To bend the 7 TeV proton beams around the ring, extremely large magnetic fields are needed. Specially designed superconducting dipoles provide an magnetic field approximately 8 T strong for both beams.
The LHC experiments (ATLAS, CMS, LHC-b and ALICE) will have to face two main experimental difficulties: pile-up and large QCD background. The first is related to the very big machine luminosity while the large QCD background comes from the nature of proton-proton collisions and the internal structure of protons [22].
We will briefly comment on these problems:

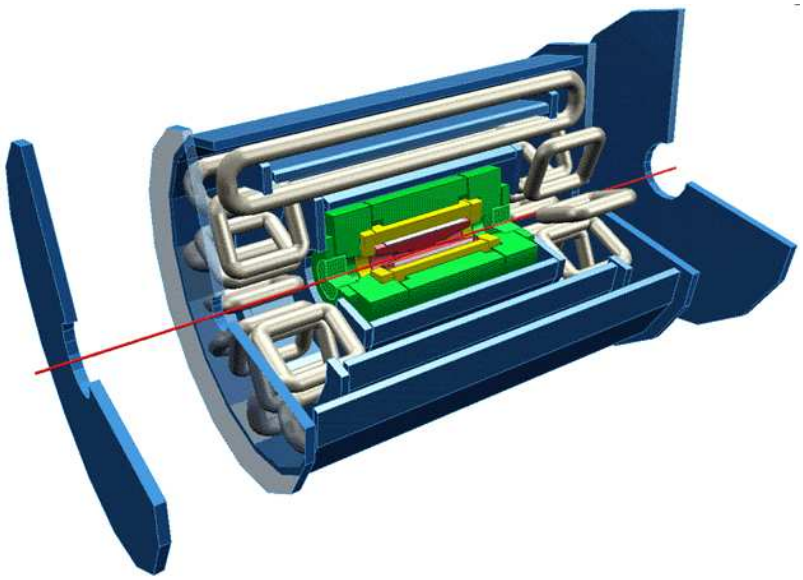

Figure 2.1: The ATLAS detector

Figure 2.2: CERN seen from the air. The large white building in front-left is the ATLAS building. In the background are the Jura mountains.

- Pile-up. Protons are grouped in bunches of 10^{11} protons colliding at a given interaction point every 25 ns. The interaction rate is 10^9 events per second at high luminosity. This gives on average 25 soft interactions (minimum bias events, low p_T) occuring simultaneously at each crossing. The soft interactions give rise, every 25 ns, to about 1000 charged particles in the detector over the pseudo-rapidity region $|\eta| < 2.5$. Therefore, when a high-pT event is produced during a bunch-crossing, this event is overlapped, on average, with 25 additional soft events. These events are called pile-up.

- QCD background. The rate of high-pT events at a hadron collider is dominated by QCD jet production. Since jet-production is a strong interaction the cross-sections are large and, in addition, many channels contribute to the final states.
  Therefore there is no hope to detect for example a Higgs boson decaying into jets unless it is produced in association with additional particles. Decays to leptons and photons have to be used instead. Since such decays usually have a smaller branching ratio than decays into quarks, the prize to pay to get rid of the QCD background is a smaller cross section and fewer interesting events.

2.2 The different parts of the ATLAS detector

The ATLAS detector consists of three major components, refs [2], [7]:

- *The Inner Detector.* The Inner Detector (ID) records the tracks of charged particles. A strong magnetic field (approximately 2 T) created by a solenoid causes the particles to bend, and the curvatures of these tracks allow the momentum and electric charge of each particle to be determined. The ID consists of three subdetectors covering the range $|\eta| < 2.5$. The three subdetectors are The Pixel Detector, The SemiConductor Tracker (SCT) and The Transition Radiation Tracker (TRT). See figure 2.3 for a picture of the inner detector.

- *The Calorimeters.* The Calorimeters absorb and measure the energies of most charged and neutral particles. Energy deposits in any part of the calorimeter are detected and converted to electrical signals which are read out by data-taking electronics.
  One calorimeter measures the energy of electrons, positrons and photons (The ElectroMagnetic calorimeter) and the other measures the total energy of hadrons (The Hadronic Calorimeter).

- *The Muon Spectrometer.* The Muon Spectrometer identifies muons and measures their momenta. Muons pass through the calorimeters without being absorbed because of the low cross section for electromagnetic interactions for muons. Muon detectors outside the calorimeter measure the trajectories of muons as they are bent by the toroid magnet system, allowing their momenta to be calculated with high precision.

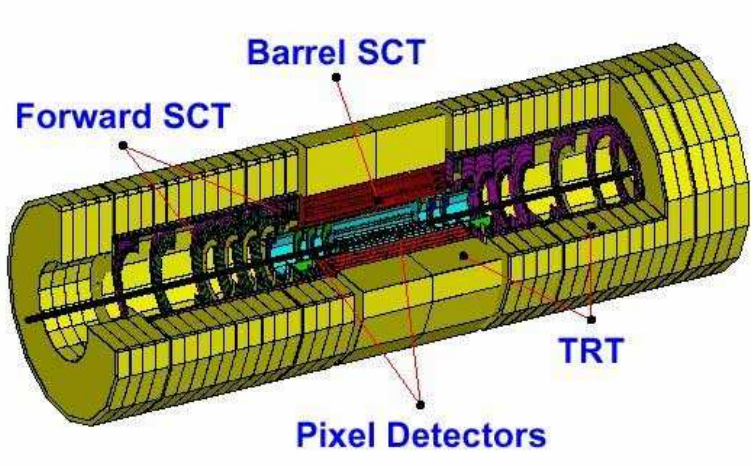

Figure 2.3: The inner detector

2.2.1 The Inner Detector

The Inner Detector (ID) is the subdetector closest to the beam-pipe, and it is mounted inside the inner detector cavity which is 7 m long and 2.3 m in diameter. Its outer dimensions are limited by the inner dimensions of the cryostat container in the Liquid Argon EM Calorimeter and the end-cap calorimeters. Mechanically, the ID consists of three units: a barrel part extending over ± 80 cm and two identical end-caps covering the rest of the cylindrical cavity.
Pattern recognition, momentum and vertex measurements and electron identification are the main objectives of the ID. This is achieved by the combination of discrete high-resolution semiconductor pixel and strip detectors by the Pixel Detector and the SemiConductor Tracker in the inner part. Further out, in the Transition Radiation Tracker (TRT), there are continuous straw-tube tracking detectors which also have the ability for transition radiation detection for the electron identification.
In the barrel region, the high-precision detector layers are arranged on concentric cylinders around the beam axis, while the end-cap detectors are mounted on disks perpendicular to the beam axis. The pixel layers are segmented in $R\phi$ and z, while the SCT detector uses small angle stereo strips to measure both coordinates, with one set of strips in each layer measuring ϕ. The barrel TRT straws are parallel to the beam direction. On the end-cap, the strip detectors have one set of strips running radially and a set of stereo strips at an angle of 40 mrad. The continuous tracking consists of radial straws arranged into wheels.

Pixel Detector

The pixel detectors provide three high resolution three-dimensional space points as close to the interaction point as possible because of the high track density in this region. High granularity and unambiguous determination of two coordinates are vital in the high occupancy environment at small radii.

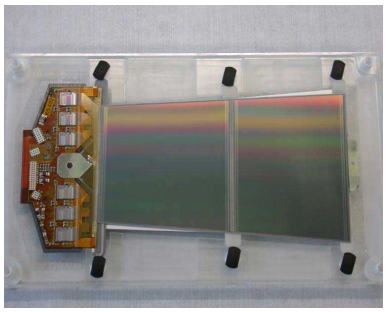

Figure 2.4: An SCT module

The innermost layer in the barrel (B-layer) is important when measuring secondary vertices produced by short-lived particles such as B hadrons and τ leptons. The B-layer covers the rapidity range $|\eta| < 2.5$.
The readout chips for the Data Acquisition system has individual circuits for each pixel element, including buffering to store the data while awaiting the level-1 trigger decision. The readout chips need to be radiation hardened to cope with 300 kGy of ionising radiation and over 5×10^{14} neutrons per cm^2 over ten years.

The pixel system contains a total of 140 million detector elements contained in about 1500 barrel modules and 700 disk modules. The pixel modules are designed to be identical in the barrel and on the disks. Each detector element is 50 μm in the $R\phi$ direction and 300 μm in z giving a very accurate measurement of hits in the pixels.
Each layer is equipped with detectors consisting of a silicon diode segmented in small rectangular pixels. Charged particles traversing the diode deposit a small signal through ionisation. Applying a reverse bias voltage the liberated carriers drift to the segmented readout plane of the detector.

Semiconductor Tracker

The SCT consists of four double layers of silicon strips which enables the SCT to provide eight precision measurements per track in the intermediate radial range, contributing to the measurement of momentum, impact parameter and vertex position, as well as providing good pattern recognition by the use of high granularity. Each double layer consists of strips aligned in the azimuthal direction and strips rotated by a 40 mrad stereo angle with respect to the first set.
The detector contains 6.2 million readout channels, and tracks can be distinguished if separated by more than 200 μm. The spatial resolution is 16 μm in $R\phi$ and 580 μm in z. Each module consists of four p-on-n silicon detectors. On each side of the module, two detectors are wire-bonded together and glued together back-to-back at a 40 mrad angle. Figure 2.4 shows an SCT module.
The Pixel and SCT subdetectors are jointly referred to as the Precision tracker. Both require a very high degree of stability, cold operation of the detectors and the removal of the heat generated by the electronics and the detector leakage current. The structures

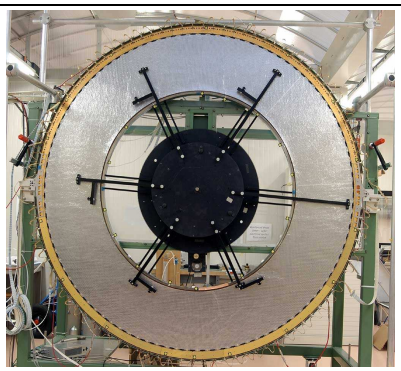

Figure 2.5: Transition Radiation Tracker

are therefore designed with materials with as low coefficient of thermal expansion as possible.

Transition Radiation Tracker

The Transition Radiation Tracker, TRT, see figure 2.5, is based on the use of gas-filled straw detectors which can operate at the very high rates of particle flux expected at the LHC. Adding xenon gas to the gas mixture increases the capability for electron identification. This is because xenon gas is good for detecting transition radiation photons created by the electrons. A large number of measurements, typically 36, can be made on every track and this continuous tracking assures a very good pattern recognition performance.

Each straw is 4 mm in diameter and equipped with a 30 μm diameter gold-plated W-Re wire, giving a fast response and good mechanical and electrical properties. The barrel contains about 50000 straws, each divided in two at the centre in order to reduce the occupancy. Read out electronics is mounted at each end. The end-caps contain 320000 radial straws with the readout at the outer radius. Each electronic channel provides a drift-time measurement, giving a spatial resolution of 170 μm per straw.
There are also two independent thresholds which allows the discrimination between tracking hits and transition-radiation hits. The tracking hits pass the lower threshold and the transition radiation hits pass the higher one. Transition radiation occurs when charged, high-energetic particles traverse the interface between substances with different dielectric properties. The charged particle emits radiation with energy proportional to the γ [1]of the particle, and so for most particle energies is only significant for electrons with their very small mass.

2.2.2 The Calorimeters

The calorimeter system is to measure the energy and $\theta - \phi$ direction of all particles and jets, except muons, formed in the collision. The energy measurement is based on the

[1] $\gamma = \frac{1}{\sqrt{1-(\frac{v}{c})^2}}$

formation of a shower, a cascade of particles, when relativistic particles traverse dense matter.
Electrons and photons create a shower through pair production, $\gamma \rightarrow e^+ + e^-$ and bremsstrahlung, $e \rightarrow e\,\gamma$ in the electric field of the nucleus. The energy loss for a particle in a given material is characterised by the radiation length X_0.

The EM Calorimeter is a lead/liquid-argon detector with an accordion geometry shown in figure 2.6.
For $|\eta| < 1.8$, the EM Calorimeter is preceded by a presampler detector, installed immediately behind the cryostat cold wall. The presampler is used to correct for the energy loss of the particles in the material upstream of the calorimeter. The particles traverse a great amount of material when passing through the Inner Detector and cryostats. This makes them lose energy and the task of the presampler is to adjust for this energy loss, so the energy measurement in the calorimeter is as accurate as possible.

The hadronic barrel calorimeter is a cylinder divided into three sections: the central barrel and two identical extended barrels. It is based on a sampling technique with plastic scintillator plates (tiles) embedded in an iron absorber. At larger pseudorapidities, where higher radiation resistance is needed, the intrinsically radiation-hard LAr technology is used for all the calorimeters.
The EM barrel is contained in a barrel cryostat. The solenoid is also integrated in the vacuum of the barrel cryostat and is placed in front of the EM calorimeter. The barrel and extended barrel hadronic calorimeters support the LAr cryostats and also act as the main solenoid flux return.
An advantage for calorimeters at high energies is that, where the relative resolution in the tracking devices is $\Delta p/p \propto p$, the resolution in the calorimeters is $\Delta E/E \propto 1/\sqrt{E}$, so it gets better with higher energies.

The Electromagnetic Calorimeter

The electromagnetic calorimeter is involved in many measurements in ATLAS. Precise measurements of the energy of electrons and photons are vital for the invariant mass reconstruction of Higgs in $H \rightarrow ZZ^{(*)} \rightarrow 4e$ and $H \rightarrow \gamma\gamma$. In the case of $H \rightarrow \gamma\gamma$, an excellent invariant mass resolution is needed to identify the signal from the irreducible continuum $\gamma\gamma$ background. The aims as defined in the TDR are

$$\frac{\Delta E}{E} \approx \frac{10\%}{\sqrt{E}} \oplus 1\%$$

where the first term is a statistical term and the second is a constant term due to systematic uncertainties, [7]. E is the energy in GeV.
The barrel of the EM Calorimeter is made up from two half barrels separated by a small gap (6 mm) at z=0 and covers the region $|\eta| < 1.475$. The two end caps are each mechanically divided into two coaxial wheels; and outer wheel covering $1.375 < |\eta| < 2.5$ and an inner wheel covering $2.5 < |\eta| < 3.2$.

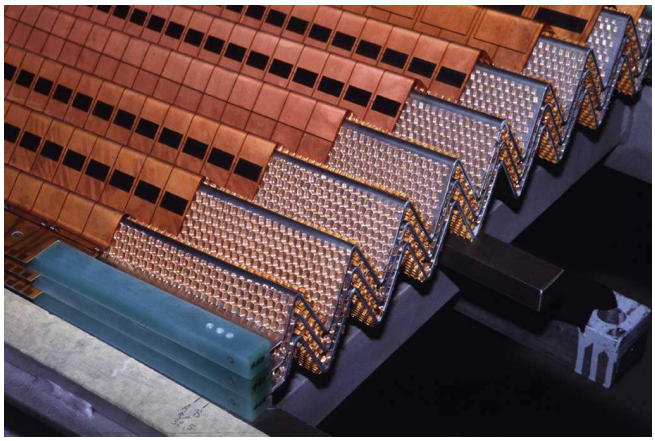

Figure 2.6: A part of the accordion shaped EM calorimeter.

The EM calorimeter consists of thin lead plates (∼1.5mm thick) immersed in a bath of liquid argon and separated by sensing devices. It is accordion shaped in order to give complete ϕ symmetry without azimuthal cracks. The accordian structure is shown in figure 2.6.
When high energy photons, electrons and positrons traverse the lead, they produce an electron shower. The large number of electrons and positrons produced in the shower is proportional to the incident energy. Their presence is detected by a sensing system between the lead plates, the electrodes, because the gaps between the plates are subjected to a large electric field. The electrical signals constitute a current which is sent to preamplifiers located outside the cryostats.

The Hadronic Calorimeters

The barrel section of the Hadronic Calorimeter is also called the tile calorimeter due to the technique used. It is a sampling calorimeter using iron as absorber and plastic scintillating tiles (plates) as the active medium. The tiles are 3 mm thick and two of the sides are read out by wavelength shifting fibres into two separate photomultipliers. The tile calorimeter is composed of one central barrel and two extended barrels.

The hadronic calorimeter absorbs and measures the energies of hadrons, including protons and neutrons, pions [2] and kaons. The EndCap hadronic calorimeters consist of copper absorbers immersed in LAr. Interactions of high energy hadrons in the plates transform the incident energy into a hadronic shower. To contain the shower, the mass of the hadronic calorimeter is quite large (typical 80 tons). The shower, when traversing the liquid, causes a trail of electron-ion pairs along its path which migrates to the readout electrode.

[2] $\pi^0 \rightarrow \gamma\gamma$ gives rise to electromagnetic showers seen in the EM Cal. π^0 produced in the hadronic calorimeter can for example be seen as two electromagnetic showers in the hadronic cal.

A good di-jet invariant mass resolution in the $H \rightarrow b\bar{b}$ channel is vital for the detection of the standard model Higgs boson in the low and intermediate mass range. The energy resolution for $|\eta| < 3$ in the Hadronic Calorimeter is

$$\frac{\Delta E}{E} \approx \frac{50\%}{\sqrt{E}} \oplus 3\%$$

where the energy is given in GeV, [24]
A hermetic hadronic calorimeter with a large rapidity coverage is crucial to the measurement of missing transverse momentum (p_T^{miss}) of the event.

2.2.3 Muon Spectrometer

The calorimeter is surrounded by the muon spectrometer. The Muon Spectrometer is based on the magnetic deflection of muon tracks in the field of the toroid magnets. The momentum resolution achieved is very good due to three stations of high-precision tracking chambers, and multiple scattering is reduced due to a light and open structure. The muon's dominant energy loss in matter is ionisation and the cross section for this is small. Therefore it is possible for the muon to go through the entire detector.

For a heavy standard model Higgs decaying into four muons, a clean signature as possible is important. Combining the measurements of the muon spectrometer and the inner detector, the momentum resolution of isolated muons is expected to be of the order of a few %. A picture of the Muon Spectrometer is shown in figure 2.7.
In the barrel region, tracks are measured in chambers arranged in three cylindrical layers and in the end-cap region the chambers are installed vertically, also in three stations. Over most of the η-range, a precision measurement of the track coordinates in the principal bending direction of the magnetic field is provided by Monitored Drift Tubes (MDTs). At large ηs and close to the interaction point, Cathode Strip Chambers (CSCs) with higher granularity are used. The MDTs provide a single-wire resolution of $\sim 80\mu$m. The MDTs are supposed to achieve an accuracy of $\sim 30\mu$m.
The trigger system covers the pseudorapidity range $|\eta| < 2.4$. Resistive Plate Chambers (RPCs) are used in the barrel and Thin Gap Chambers (TGCs) are used in the end cap regions.

The basic detection elements of the MDT chambers are aluminium tubes filled with gas and with a central W-Re wire in the middle. The CSCs are multi-wire proportional chambers with cathode strip readout. The precision coordinate is obtained by measuring the charge induced on the segmented cathode by the avalanche formed on the anode wire. Good spatial resolution is achieved by segmentation of the readout cathode and by charge interpolation between neighbouring strips.

The basic RPC unit is a narrow gas gap formed by two parallel resistive bakelite plates, separated by insulating spacers. Each chamber is made from two detector layers and four readout strips. The primary ionisation electrons are multiplied into avalanches

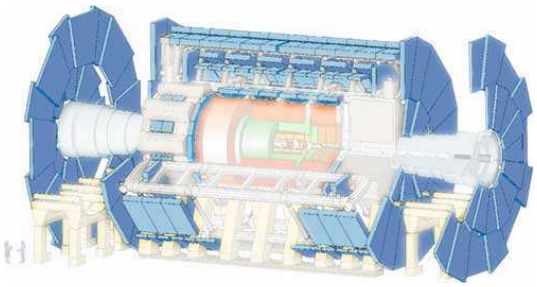

Figure 2.7: The Muon Spectrometer of the ATLAS-detector. The blue parts correspond to the spectrometer.

Figure 2.8: The solenoid magnet of the ATLAS detector.

by a high, uniform field. The TGCs are similar in design to multi-wire proportional chambers. Signals from the anode wires provide the trigger information together with readout strips arranged orthogonal to the wires. These readout strips are also used to measure the second coordinate.

2.2.4 The magnet systems

The magnet system is a joint arrangement of a Central Solenoid (CS), providing the inner detector with magnetic field, surrounded by three large air-core toroids generating the magnetic field for the muon spectrometer. The toroids are divided into one Barrel Toroid (BT) and two End Cap Toroids (ECT). The overall sizes of the magnet system are 26 m in length and 20 m in diameter. The CS extends over a length of 5.3 m and has a core of 2.4 m. It provides a central field of around 2 T along the beam axis. The CS design has been of high importance and due to its position in front of the EM calorimeter, the CS is designed to be as thin as possible without sacrificing operational safety and reliability.

The BT is a large construction with its 25.3 metres of length and 20.1 metres of outer diameter. It consists of eight coils assembled radially and symmetrically around the beam axis. It produces an approximately cylindrical field around the detector.

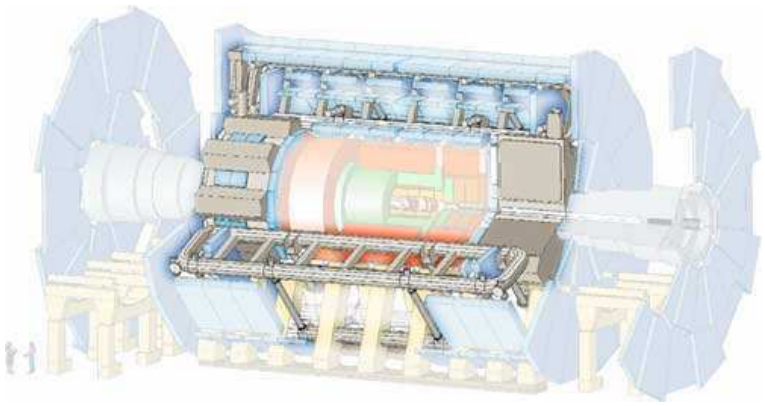

Figure 2.9: The toroids of the ATLAS detector.

The ECT are also made up from eight racetrack, double-pancake coils in an aluminium alloy inside a large cryostat. These coils are rotated 22.5 degrees with respect to the BT coils in order to provide radial overlap and to optimize the bending power in the interface regions of both coil systems. The ECTs provide a peak magnitic field of 4.1 T and a bending power of 4 to 8 Tm. They are 5 m long and the outer diameter is 10.7 m. The ECTs are inserted in the barrel toroid at each end and line up with the CS.

2.2.5 Trigger and data-acquisition system

The ATLAS trigger and data-acquisition (DAQ) system is based on three levels of online event selection. Each trigger level refines the decisions made at the previous level and, where necessary, applies additional selection criteria. The three levels are referred to as Level One trigger (LVL1), Level Two trigger (LVL2) and Event Filter (EF). The LVL2 trigger and Event Filter comprise the ATLAS High Level Trigger system. Figure 2.10 gives a schematic view of the trigger.

Starting from an initial bunchcrossing rate at 40 MHz, corresponding to an interaction rate of $10^9 Hz$ at design luminosity, the rate of selected events must be reduced to about 100 Hz for permanent storage. This requires an overall rejection factor of 10^7 against minimum bias events and very high efficiency must be retained for the rare and interesting new physics events.

The observation of new heavy objects with masses of O(1) TeV will involve very high p_T signatures. This is not a problem for the online selection. However, the challenge is the efficient and unbiased selection of lighter objects with masses of O(100) GeV. The ATLAS trigger relies on the concept of physics objects (muons, electrons, jets, etc) and most of the selection criteria used are based on the selection of at most a few high p_T objects, such as charged leptons, photons, jets, or other high p_T criteria such as missing

and total transverse energy.[3]

Candidate objects are typically first identified and crudely reconstructed at LVL1. The LVL1 trigger makes an initial selection based on reduced granularity information from a subset of detectors. Processing in the HLT progressively refines the reconstruction, rejecting fake objects and improving the precision on measured parameters such as E_T. Events selected by LVL1 are read out from the front-end electronics systems of the detectors into readout drivers (RODs) and then into readout buffers (ROBs). All the detector data for the bunch crossing selected by the LVL1 are held in the ROBs until a decision has been made by the LVL2 trigger. The LVL2 trigger makes use of region-of-interest (RoI) information provided by the LVL1 trigger. Using the RoI information, the LVL2 trigger selectively accesses data from the ROBs, moving only the data that are required in order to make the LVL2 decision. If the event is accepted by LVL2, it is transferred by the DAQ system to storage associated with the EF which constitutes the third level of event selection. The process of moving data from the ROBs to the EF is called event building. Before event building each event is composed of many fragments, with one fragment in each ROB. After the event building the full event is stored in a single memory accessible by an EF processor.

[3]Transverse energy is defined as Energy multiplied with $sin\theta$ where θ is the angle between p_z and p of a particle.

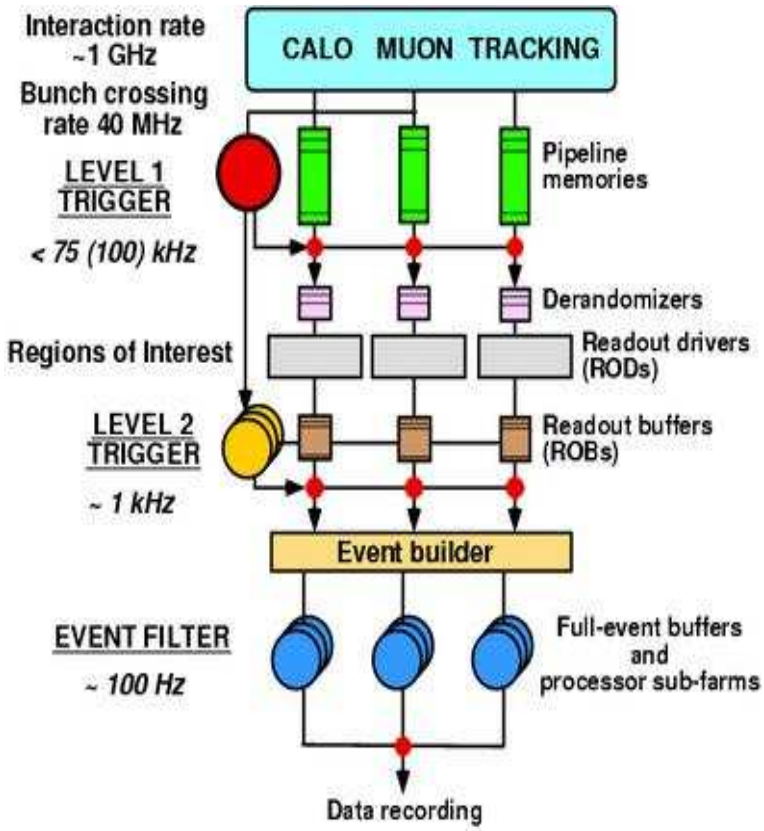

Figure 2.10: The trigger and DAQ system is based on three levels of online event selection. From an interacting rate of $\sim 10^9 Hz$ the rate of selected events must be reduced to $\sim 100 Hz$ for permanent storage. A functional view of the system is shown in this figure.

Chapter 3

Theory

When a gauge-invariant and renormalizable unified theory for the weak and electromagnetic interactions is derived, all leptons, quarks and gauge bosons come out massless. In reality, only photons are massless so something is wrong![1] In order to keep the theory renormalizable, it is very important to introduce the masses by a mechanism which retains the gauge invariance of the Lagrangian. The mechanism of spontaneous symmetry breaking provides such a mechanism.

We first investigate the principle of spontaneous symmetry breaking before it is applied to the electroweak theory and then giving mass to all particles.

3.1 Spontaneous symmetry breaking

In order to explain the idea of spontaneous symmetry breaking, we consider a system where the Lagrangian, L, possesses a symmetry. That means that the Lagrangian is invariant under the corresponding symmetry transformations. For example, L might be spherically symmetric and therefore invariant under rotations.
In classifying the energy levels of this system, essentially two situations can occur:

- If a given energy level is non-degenerate, the corresponding energy eigenstate is unique and invariant under the symmetry transformations of L.
- If an energy level is degenerate, the corresponding eigenstates are not invariant but transform linearly among themselves under the symmetrytransformations of L.

Consider the lowest energy level of the system. If it is non-degenerate, the state of lowest energy is unique. If it is degenerate there is no unique eigenstate to represent the ground state. If we in the case of degeneracy arbitrarily select one of the states as the

[1] Neutrinos are believed to have a small but non-zero mass.

ground state, then the ground state no longer shares the symmetries of L. This way of obtaining an asymmetric ground state, is known as *spontaneous symmetry breaking*. The asymmetry is due to the arbitrary choice of one of the degenerate states. Note that the Lagrangian density still is invariant under the symmetry operation.

The state of lowest energy is the vacuum and spontaneous symmetry breaking is only applicable if the vacuum state is non-unique. We therefore assume that the vacuum expectation value of one quantized field is non-vanishing.
If this is to be the case, the field must be a scalar field, $\phi(x)$, and its vacuum expectation value must be constant:

$$< 0|\phi(x)|0 >= c \tag{3.1}$$

The vacuum expectation value of any spinor field $\psi(x)$ or any vector field $V^{\mu}(x)$ must vanish, however.

The simplest example of a field theory exhibiting spontaneous symmetry breaking is the Goldstone model whose Lagrangian is given by

$$\mathcal{L}(x) = [\partial^{\mu}\phi^{*}(x)][\partial_{\mu}\phi(x)] - \mu^{2}|\phi(x)|^{2} - \lambda|\phi^{4}(x)| \tag{3.2}$$

$\phi = \phi_1 + i\phi_2$ is a complex scalar field, and μ and λ are arbitrary real parameters.
If we as a start consider a classical field theory, ϕ is a classical field and μ is not interpreted as a particle mass.
The Lagrangian density is invariant under the global U(1) phase transformations.

$$\phi(x) \rightarrow \phi^{'}(x) = \phi(x)exp(i\alpha) \tag{3.3}$$

$$\phi^{*}(x) \rightarrow \phi^{*^{'}} = \phi^{*}(x)exp(-i\alpha) \tag{3.4}$$

This symmetry is going to be spontaneously broken.

For the energy of the field to be bounded from below, we require $\lambda > 0$.
We derive the Hamiltonian density for this system by using

$$\mathcal{H} = \frac{\partial\mathcal{L}}{\partial\dot{\phi}}\dot{\phi} - \mathcal{L} \tag{3.5}$$

and split it into two parts where one of the parts, $V(\phi)$ is the potential energy density of the field. The expression for $V(\phi)$ is given by

$$V(\phi) = \mu^{2}|\phi(x)|^{2} + \lambda|\phi(x)|^{4} \tag{3.6}$$

For the energy to be bounded from below, $\lambda > 0$. The minimum value of $\mathcal{H}(x)$, and hence of the total energy of the field, corresponds to that constant value of $\phi(x)$ which minimizes $V(\phi)$. Two different situations occur, depending on the sign of μ^2.

- $\mu^2 > 0$. In this case, the two terms in $V(\phi)$ are also positive definite. The corresponding potential energy surface $V(\phi)$ as a function of $\phi_1(x)$ and $\phi_2(x)$. $V(\phi)$ looks like a parabola and has an absolute minimum for the unique value $\phi(x) = 0$. This implies that spontaneous symmetry breaking cannot occur.

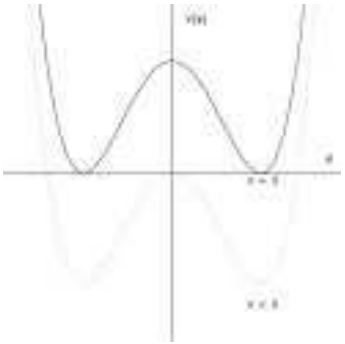

Figure 3.1: The potential energy

- When $\mu^2 < 0$, the situation is totally different. The potential energy surface for this case is shown in figure 3.1. $V(\phi)$ possesses a local maximum at $\phi(x) = 0$ and a whole circle of absolute minima at

$$\phi(x) = \phi_0 = \left(\frac{-\mu^2}{2\lambda}\right)^{\frac{1}{2}} exp(i\theta) \tag{3.7}$$

where the phase angle θ defines a direction in the complex ϕ-plane. We see that the state of lowest energy, the vacuum state, is not unique in this case. Spontaneous symmetry breaking will occur if we choose one particular direction ϕ to represent the vacuum ground state. Because of the invariance of the Lagrangian density under the global phase transformation above, the value of θ chosen is not significant and we shall take $\theta = 0$, so that

$$\phi_0 = \left(\frac{-\mu^2}{2\lambda}\right)^{\frac{1}{2}} = \frac{1}{\sqrt{2}}v \tag{3.8}$$

is purely real.

We now introduce two real fields $\sigma(x)$ and $\eta(x)$ through the relation

$$\phi(x) = \frac{1}{\sqrt{2}}[v + \sigma(x) + i\eta(x)] \tag{3.9}$$

$\sigma(x)$ and $\eta(x)$ measure the deviations of the field $\phi(x)$ from the equilibrium ground state configuration $\phi(x) = \phi_0$. In terms of these fields, the Lagrangian density becomes

$$\mathcal{L} = \frac{1}{2}[\partial^\mu\sigma(x)][\partial_\mu\sigma(x)] - \frac{1}{2}(2\lambda v^2)\sigma^2(x) \tag{3.10}$$

$$+\frac{1}{2}[\partial^\mu\eta(x)][\partial_\mu\eta(x)] \tag{3.11}$$

$$-\lambda v\sigma(x)[\sigma^2(x) + \eta^2(x)] - \frac{1}{4}\lambda[\sigma^2(x) + \eta^2(x)]^2 \tag{3.12}$$

where a constant term is neglected.
The two expressions for the Lagrangian are equivalent and they must therefor lead to the same physical results. We treat the terms quadratic in σ and η in equation 3.10 as the free Lagrangian density. It is now seen that $\sigma(x)$ and $\eta(x)$ are real Klein Gordon fields so on quantization they give rize to neutral spin 0 particles since both fields are real. The σ boson has real, positive mass $\sqrt{2\lambda v^2}$ and the η boson is massless. There is a theorem by Goldstone which states that for every spontaneously broken continuous symmetry, the theory must contain a massless particle. Here, one symmetry (the invariance of the vacuum) has been broken, and consequently one Goldstone boson, η, appears. No Goldstone bosons are observed in nature, so we have to get rid of them somehow.

3.2 The Higgs Model

The Goldstone Model is easily generalized to be invariant under U(1) gauge transformations. As always, we introduce a gauge field, $A_\mu(x)$ and replace the ordinary derivatives in the Goldstone Lagrangian density by the covariant derivatives

$$D_\mu = [\partial_\mu + iqA_\mu(x)] \tag{3.13}$$

We also have to add the Lagrangian density of the free gauge field

$$-\frac{1}{4}F_{\mu\nu}(x)F^{\mu\nu}(x) \tag{3.14}$$

where

$$F_{\mu\nu}(x) = \partial_\nu A_\mu(x) - \partial_\mu A_\nu(x) \tag{3.15}$$

In this way we obtain the Lagrangian density

$$\mathcal{L}(x) = [D^\mu\phi(x)]^*[D_\mu\phi(x)] - \mu^2|\phi(x)|^2 - \lambda|\phi(x)|^4 - \frac{1}{4}F_{\mu\nu}(x)F^{\mu\nu} \tag{3.16}$$

which defines the Higgs model. The Lagrangian above is invariant under the U(1) gauge transformations

$$\phi(x) \to \phi'(x) = \phi(x)\exp(-iqf(x)) \tag{3.17}$$
$$\phi^*(x) \to \phi^{*'}(x) = \phi^*(x)\exp(iqf(x)) \tag{3.18}$$
$$A_\mu \to A'_\mu = A_\mu + \partial_\mu f(x) \tag{3.19}$$

The starting point is as in the analysis of the Goldsone model. We take $\lambda > 0$ and consider the cases where $\mu^2 > 0$ and $\mu^2 < 0$ separately. In the first case, the state of lowest energy corresponds to both $\phi(x)$ and $A_\mu(x)$ vanishing, so that spontaneous symmetry breaking cannot occur.
For μ^2, the vacuum state is not unique which leads to spontaneous symmetry breaking. To ensure Lorentz invariance, the vector field $A_\mu(x)$ must vanish for the vacuum. We obtain a circle of minimum $\mathcal{H}$ corresponding to $\phi(x)$ taking on the values ϕ_0. As for the

Goldstone model, we choose the real and positive value $\left(\frac{-\mu^2}{2\lambda}\right)^{\frac{1}{2}} = \frac{1}{\sqrt{2}}v$. We define the real fields $\sigma(x)$ and $\eta(x)$ by

$$\phi(x) = \frac{1}{2}\left[v + \sigma(x) + i\eta(x)\right] \tag{3.20}$$

as before.
In terms of these fields, the Lagrangian density becomes

$$\mathcal{L}(x) = \frac{1}{2}[\partial^\mu\sigma(x)][\partial_\mu\sigma(x)] - \frac{1}{2}(2\lambda v^2)\sigma^2(x) \tag{3.21}$$

$$-\frac{1}{4}F_{\mu\nu}(x)F^{\mu\nu}(x) + \frac{1}{2}(qv)^2A_\mu(x)A^\mu(x) \tag{3.22}$$

$$+\frac{1}{2}[\partial^\mu\eta(x)][\partial_\mu\eta(x)] \tag{3.23}$$

$$+qvA^\mu(x)\partial_\nu\eta(x) + interaction\ terms. \tag{3.24}$$

The direct interpretation of equation 3.21 is not straightforward. The difficulties arise because of the product term $A^\mu\partial_\nu\eta(x)$. These fields are not independent and one cannot conclude that the second and third lines of the Lagrangian describe massive vector bosons and massless scalar bosons, respectively.
If the degrees of freedom for the Lagrangian density are counted, the problems become even more apparent. Equation 3.16 has four degrees of freedom: two from the complex scalar field $\phi(x)$, and two from the real massless vector field $A_\mu(x)$.
In equation 3.21, however, the real scalar fields $\sigma(x)$ and $\eta(x)$ each represents one degree and the real massive vector field A_μ contributes three degrees of freedom, corresponding of the three independent polarization states. This makes up a total of five degrees of freedom. We must conclude that the Lagrangian density 3.21 contains an unphysical field which does not represent real particles and which has to be eliminated.

The scalar field $\eta(x)$ can be eliminated from the Lagrangian 3.21. For any complex field $\phi(x)$, a gauge transformation of the form 3.17 can be found which transforms $\phi(x)$ into a real field of the form

$$\phi(x) = \frac{1}{\sqrt{(2)}}[v + \sigma(x)] \tag{3.25}$$

This is the so-called *unitary gauge*. When equation 3.25 is substituted into equation 3.16, quadratic terms and higher-order interaction terms are separated.

$$\mathcal{L} = \mathcal{L}_0(x) + \mathcal{L}_I(x) \tag{3.26}$$

where

$$\mathcal{L}_0(x) = \frac{1}{2}[\partial^\mu\sigma(x)][\partial_\mu\sigma(x)] - \frac{1}{2}(2\lambda v^2)\sigma^2(x) - \frac{1}{4}F_{\mu\nu}(x)F^{\mu\nu}(x) + \frac{1}{2}(qv)^2A_\mu(x)A^\mu(x) \tag{3.27}$$

and

$$\mathcal{L}_I = -\lambda v\sigma^3(x) - \frac{1}{4}\lambda\sigma^4(x) + \frac{1}{2}q^2A_\mu(x)A^\mu(x)[2v\sigma(x) + \sigma^2(x)] \tag{3.28}$$

We interpret $\mathcal{L}_0(x)$ as the free-field Lagrangian density of a real Klein-Gordon field $\sigma(x)$ and a real massive vector field $A_\mu(x)$. On quantizing $\mathcal{L}_0(x)$, $\sigma(x)$ gives rise to neutral scalar bosons of mass $\sqrt{2\lambda v^2}$, and $A_\mu(x)$ to neutral vector bosons of mass $|qv|$.

3.3 The electroweak theory

We are then in the situation where we have obtained a Lagrangian density for a real scalar field and a massive real vector field, starting from the Lagrangian density for a complex scalar field and a massless real vector field. In both cases, the number of degrees of freedom is four. Of the two degrees of freedom of the complex field $\phi(x)$, one has been taken up by the vector field $A_\mu(x)$ which has become massive in the process; the other shows up as the real field $\sigma(x)$.
This phenomenon by which a vector boson acquires mass without destroying the gauge invariance of the Lagrangian density is known as the *Higgs mechanism*, and the massive spin 0 boson associated with the field $\sigma(x)$ is called a *Higgs boson*.
The Higgs mechanism does not generate Goldstone bosons. In essence, the field $\eta(x)$ which in the Goldstone model was associated with the massless Goldstone bosons, has been eliminated by gauge invariance, and the degree of freedom of $\eta(x)$ has been transferred to the vector field $A_\mu(x)$.

When the Higgs mechanism is applied to the electroweak theory, all particles known to have mass acquire mass.
The Lagrangian for the unified model of electromagnetic and weak interactions of massless leptons and massless gauge bosons can be written

$$\mathcal{L} = \mathcal{L}^L + \mathcal{L}^B \tag{3.29}$$

where $\mathcal{L}^{\mathcal{L}}$ is the standard leptonic Lagrangian density and $\mathcal{L}^{\mathcal{B}}$ is the gauge-boson Lagrangian density in electroweak theory.
The Lagrangian density 3.29 is invariant under the $SU(2)\times U(1)$ gauge transformations of electroweak theory.

The necessary formalism is an immediate extension of that of the Higgs model. To break the gauge invariance spontaneously, we must again introduce a Higgs field which has to be a field with several components since we now want to break the $SU(2)$ symmetry.

$$\Phi(x) = \begin{pmatrix} \phi_a(x) \\ \phi_b(x) \end{pmatrix},$$

where $\phi_a(x)$ and $\phi_b(x)$ are scalar fields under Lorentz transformations.
The transformation laws of $\Phi(x)$ under $SU(2)\times U(1)$ gauge transformations are

$$\Phi(x) \rightarrow \Phi^{'}(x) = exp[ig\tau_j\omega_j(x)/2]\Phi(x) \tag{3.30}$$
$$\Phi^{\dagger}(x) \rightarrow \Phi^{\dagger'}(x) = \Phi^{\dagger}(x)exp[-ig\tau_j\omega_j(x)/2] \tag{3.31}$$

and under U(1) weak hypercharge transformations according to

$$\Phi(x) \rightarrow \Phi^{'}(x) = exp[ig^{'}Yf(x)]\Phi(x) \tag{3.32}$$
$$\Phi^{\dagger}(x) \rightarrow \Phi^{\dagger'}(x) = \Phi^{\dagger}(x)exp[-ig^{'}Yf(x)] \tag{3.33}$$

where Y is the weak hypercharge of the field $\Phi(x)$.

We now want to generalize the Lagrangian density to include the Higgs field $\Phi(x)$ and its interactions with the gauge-boson fields, and to continue to be $SU(2) \times U(1)$ gauge-invariant. Equation 3.29 is already gauge invariant and a generalization that shares gauge invariance is

$$\mathcal{L} = \mathcal{L}^L + \mathcal{L}^B + \mathcal{L}^H \tag{3.34}$$

where

$$\mathcal{L}^H(x) = [D^\mu \Phi(x)]^\dagger [D_\mu \Phi(x)] - \mu^2 \Phi^\dagger(x)\Phi(x) - \lambda[\Phi^\dagger(x)\Phi(x)]^2 \tag{3.35}$$

where the covariant derivative $D^\mu \Phi(x)$ is defined by

$$D^\mu \Phi(x) = [\partial^\mu + ig\tau_j W_j^\mu(x)/2 + ig' Y B^\mu(x)]\Phi(x) \tag{3.36}$$

For $\lambda > 0$ and $\mu^2 < 0$, the classical energy density is a minimum for a constant Higgs field

$$\Phi(x) = \Phi_0 = \begin{pmatrix} \phi_a^0 \\ \phi_b \end{pmatrix}$$

with

$$\Phi_0^\dagger \Phi_0 = |\phi_a^0|^2 + |\phi_b^0|^2 = \frac{-\mu^2}{2\lambda} \tag{3.37}$$

The Higgs field of the vacuum ground state is in general not invariant under $SU(2) \times U(1)$ gauge transformations. However, it must be invariant under U(1) electromagnetic gauge transformations in order to ensure zero mass for the photon and conservation of the electrical charge.

Again, an arbitrary Higgs field $\Phi(x)$ is parametrized in terms of its deviations from the vacuum field Φ_0 in the form

$$\Phi(x) = 2^{-\frac{1}{2}} \begin{pmatrix} \eta_1(x) + i\eta_2(x) \\ v + \sigma(x) + i\eta_3(x) \end{pmatrix}$$

By means of this equation, we can express the Lagrangian density in terms of the four real fields $\sigma(x)$ and $\eta_i(x), i = 1, 2, 3$. The interpretation and quantization of these fields lead to the same difficulties as in previous sections. The way to resolve them, is the same and the unitary gauge is once again employed.

As in the previous case, the fields $\eta_i(x), i = 1, 2, 3$, are unphysical fields. In the unitary gauge, they are transformed away. The W and Z bosons then aquire their masses while the photon remains massless since the electromagnetic gauge symmetry has not been spontaneously broken.

To obtain non-vanishing lepton masses, however, the Lagrangian density has to be augmented by adding a suitable term to it. This is done by introducing the term $\mathcal{L}^{LH}$.

$$\mathcal{L} = \mathcal{L}^L + \mathcal{L}^B + \mathcal{L}^H + \mathcal{L}^{LH} \tag{3.38}$$

The lepton and Higgs field are coupled through Yukawa interactions, described by the Lagrangian density

$$\mathcal{L}^{LH}(x) = -g_l[\overline{\Psi}_l^L(x)\psi_l^R(x)\Phi(x) + \Phi^\dagger(x)\overline{\psi}_l^R(x)\Psi_l^L(x)] \tag{3.39}$$
$$-g_{\nu_l}[\overline{\Psi_l^L}(x)\psi_{\nu_l}^R(x)\tilde{\Phi}(x) + \tilde{\Phi}^\dagger(x)\overline{\psi_{\nu_l}^R}(x)\Psi_l^L(x)] \tag{3.40}$$

where g_l and g_{ν_l} are dimensionless coupling constants, summations over $l = e, \mu$ are implied and R and L means right and left components of the fields. $\tilde{\Phi}$ is defined by

$$\tilde{\Phi}(x) = \begin{pmatrix} \phi_b^*(x) \\ -\phi_a^*(x) \end{pmatrix}$$

The Lagrangian density $\mathcal{L}^{LH}$ is invariant under $SU(2) \times U(1)$ gauge transformations.

When the total electroweak Lagrangian is transformed into the unitary gauge, we obtain a rather lengthy expression which conveniently is separated into free fields and interaction terms. Both parts contain expressions for the Higgs field. That is, there is free Higgs field part and terms that show how the Higgs interact with other particles and itself.

$$\mathcal{L} = \mathcal{L}_0 + \mathcal{L}_I \tag{3.41}$$

where

$$\mathcal{L}_0 = \overline{\psi_l}(i\gamma_\mu\partial^\mu - m_l)\psi_l + \overline{\psi}_{\nu_l}(i\gamma_\mu\partial^\mu - m_{\nu_l})\psi_{\nu_l} \tag{3.42}$$
$$-\frac{1}{4}F_{\mu\nu}F^{\mu\nu} \tag{3.43}$$
$$-\frac{1}{2}F_{W\mu\nu}^\dagger F_W^{\mu\nu} + m_W^2 W_\mu^\dagger W^\mu \tag{3.44}$$
$$-\frac{1}{4}Z_{\mu\nu}Z^{\mu\nu} + \frac{1}{2}m_Z^2 Z_\mu Z^\mu \tag{3.45}$$
$$+\frac{1}{2}(\partial^\mu\sigma)(\partial_\mu\sigma) - \frac{1}{2}m_H^2\sigma^2 \tag{3.46}$$

and where

$$\mathcal{L}_I = \mathcal{L}^{LB} + \mathcal{L}^{BB} + \mathcal{L}^{HH} + \mathcal{L}^{HB} + \mathcal{L}^{HL} \tag{3.47}$$

The interpretation of these equations is that they constitute the Lagrangian density of free fields which can be quantized in the usual way. For example, term 3.42 are just the Lagrangian densities of charged leptons with mass m_l and neutrinos with mass m_{ν_l} while 3.43 describe massless photons. Term 3.44 describes charged vector bosons with mass m_W, equation 3.45 describe neutral vector bosons of mass m_Z and the term 3.46 describes a neutral spin 0 boson of mass m_H.
The term 3.47 is the interaction Lagrangian density of the standard electroweak theory. For example, $\mathcal{L}^{LB}$ is the interaction of leptons with gauge bosons.

It is a remarkable feature of this expression that it allows for a determination of the masses of the vector bosons, $W^{\pm}$ and Z. This is because the parameters m_W and m_Z introduced in 3.42 - 3.46 are defined through basic parameters of the theory.

$$m_W = \frac{vg}{2} \tag{3.48}$$

which becomes

$$m_W = \left(\frac{\alpha\pi}{G\sqrt{2}}\right)^2 \frac{1}{sin\theta_w} \tag{3.49}$$

where $\alpha = 1/137.04$, the fine structure constant, G is the Fermi coupling constant, $G = 1.166 * 10^{-5} GeV^{-2}$. θ_w, the weak mixing angle, was first determined by neutrino scattering, so m_W could be determined. It is also of course possible to measure m_W and $m_Z = m_W/sin\,\theta_w$ and then determine the weak mixing angle. Especially m_Z was very precise measured at LEP. [2]
The fact that these masses can be predicted represents strong evidence in support of the electroweak theory. But, of course, the experimental discovery of the Higgs boson is the last and ultimate confirmation.

[2]In 3.49 radiative corrections are neglected. When the renormalized masses and charges are used, correction terms of order in α will appear.

Chapter 4

Higgs phenomenology

The possible decay-channels for a Higgs-boson are strongly dependent on the mass of the Higgs. The LEP experiment at CERN which completed data-taking in November 2000, was able to set a lower bound for the mass of the Higgs at 114.1 GeV at 95% confidence level. An upper limit of 1 TeV is derived from unitarity arguments. The total width of Higgs approaches the value of the mass itself for a very heavy particle.

The difference between the total cross section between interesting events such as Higgs production and background events is often greater than ten orders of magnitude. Most of the interactions are only interactions between gluons and quarks where very little energy is transferred. These are called minimum bias events and only low momentum hadrons are produced. To extract the signal above the very dominant QCD background requires very clean signatures. One of these is the identification of leptons with high transverse momentum. Leptons have a very low rate in minimum bias events but can be found in selected decay modes of many physics processes. This need for identifying leptons has greatly influenced the design of the ATLAS detector.

4.1 The results from other experiments.

The LEP experiments completed data taking in November 2000 after 11 years of running. The center of mass energy was pushed to 209 GeV and the luminosity reached about $687 pb^{-1}$. LEP was a electron-positron collider and LHC is now being built in the same tunnel where LEP was placed.
Just before shut-down, hints of a Higgs boson discovery around 116 GeV appeared. However, the runs did not continue into 2001, [30].

In September 2000, ALEPH presented a data excess consistent with the reaction $e^+e^- \rightarrow HZ \rightarrow b\bar{b}q\overline{q}$ for a Higgs boson mass of about 115 GeV. [1]. The other experiments did not confirm these observations. In November 2000, L3 provided support for a signal observation with a $HZ \rightarrow b\overline{b}\nu\overline{\nu}$ candidate at the same mass. However, the observations were not enough to claim discovery of a Higgs boson because the observations only gave

[1] The LEP experiments were: ALEPH, DELPHI, L3 and OPAL

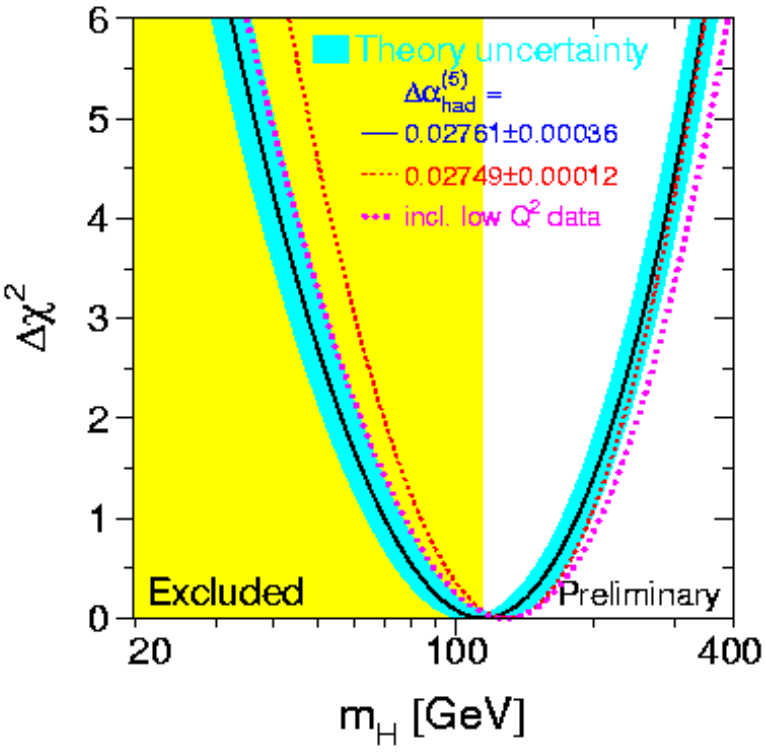

Figure 4.1: The figure shows the $\Delta\chi^2$ curve based on results from LEP, SLD, CDF and D0 as a function of the Higgs-mass, assuming the SM to be the correct theory of nature. The preferred value of its mass (corresponding to the minimum of the curve), is at 114 GeV with an experimental uncertainty of +69 and -45 GeV. from http://lepewwg.web.cern.ch/LEPEWWG/

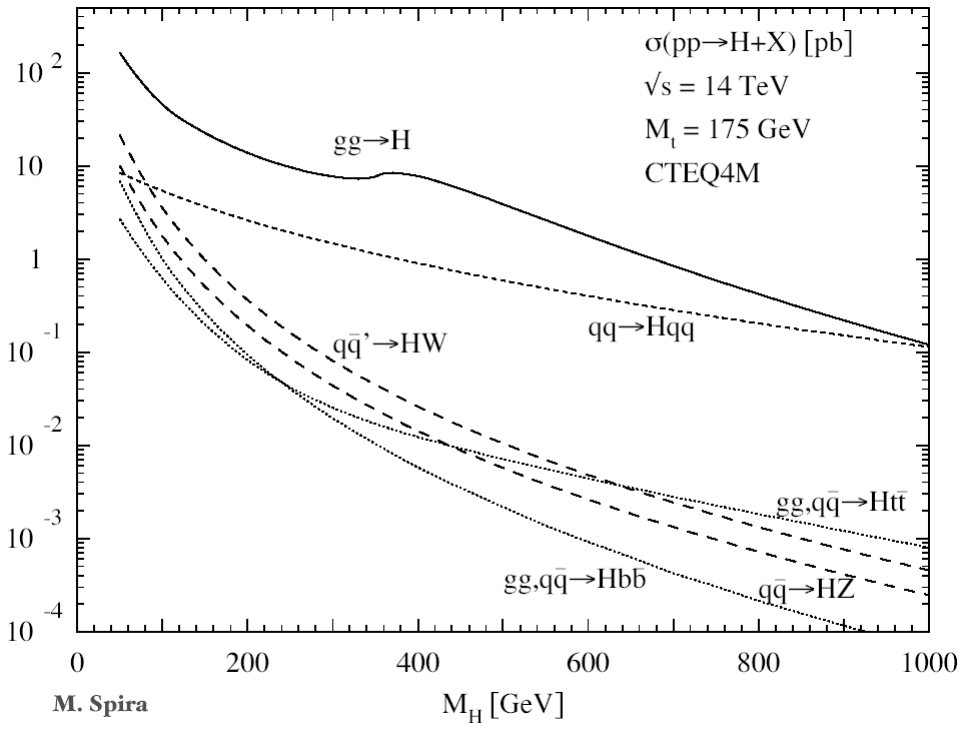

Figure 4.2: Higgs production cross sections, from [4]

a significance of 2.1 sigmas for a Higgs with mass 115 GeV.
The achievement was to exclude a Higgs boson below a mass of 114.1 GeV at 95% Confidence Level (the yellow part in figure 4.1. Figure 4.1 shows the best fit of the Standard Model to the LEP data.

4.2 Higgs production

The production of the Standard Model Higgs boson at LHC is expected to proceed mainly through the diagrams shown in figure 4.3.

Gluon-gluon fusion through a quark loop is the dominant production channel for all masses. The loop is totally dominated by the top quark because of the strong Higgs coupling to the heavy top quark, [11].
Vector boson fusion becomes increasingly important with increasing Higgs boson masses, attaining a cross section similar to that of gluon-gluon fusion for m_H $1TeV$. This process leads to the very distinctive signature of two jets from the two remaining quarks, emitted at small angle with the beam axis. The associated Higgs production with a $t\bar{t}$ or a W/Z boson has a significantly smaller cross section but gives rise to final states which are relatively easy to extract from the background because of the additional signature produced in the decay of the accompanying particles, [4].

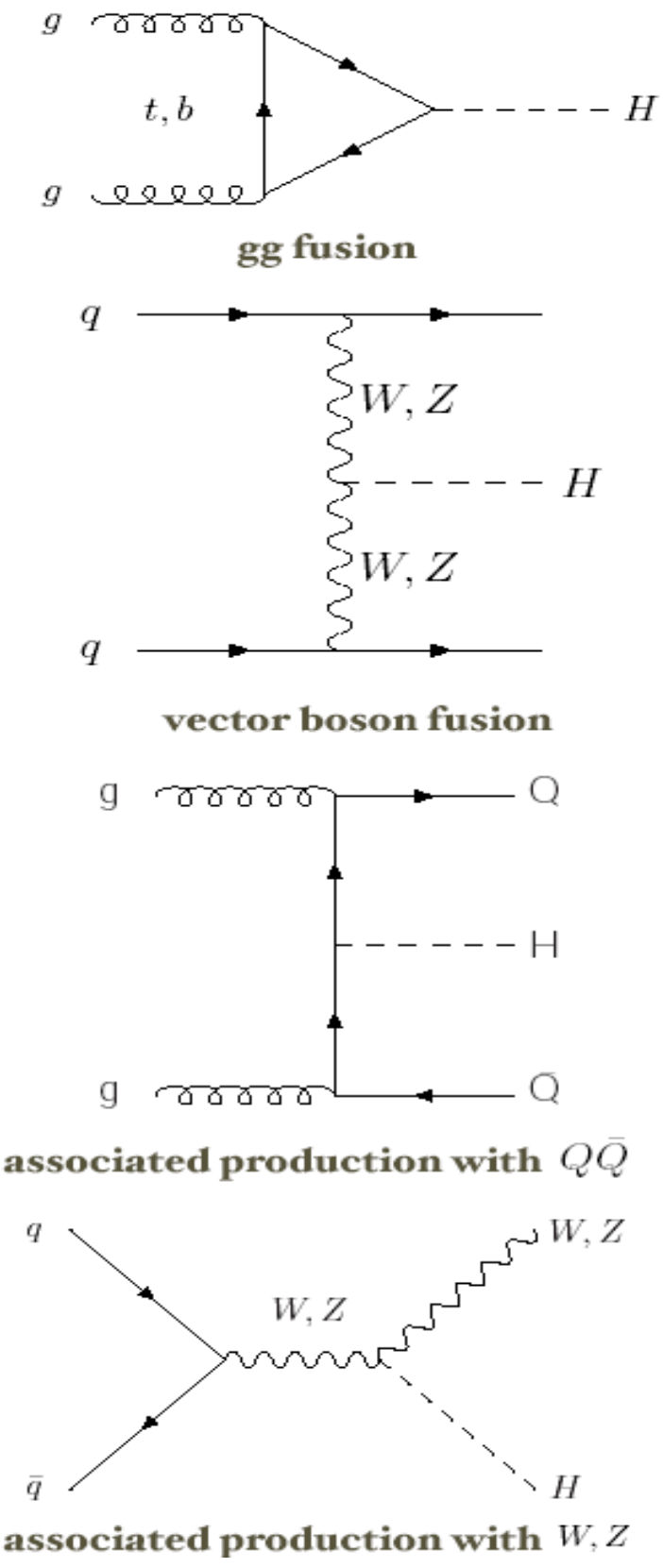

Figure 4.3: .Feynman diagrams of the most important Higgs production processes in a hadron collider.

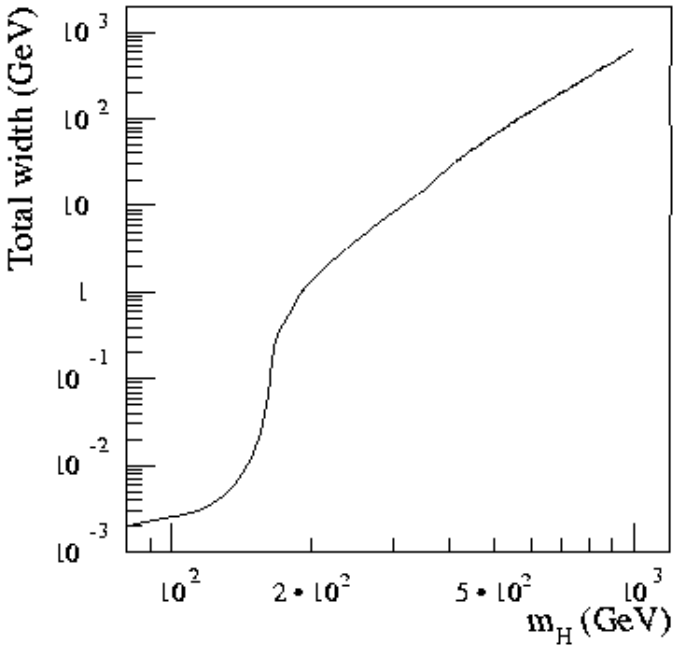

Figure 4.4: The total width of the Standard Model Higgs. Note that the width approaches the mass itself for a very heavy Higgs. From [4]

4.3 Higgs width

The width of a heavy Higgs is proportional to m_H^3 and the exact expression is given by, [4],

$$\Gamma_H = \frac{3g^2}{128\pi m_W^2} * m_H^3 \approx 0.5(TeV)^{-2} * m_H^3 \tag{4.1}$$

The total width is to a good approximation a sum of the partial widths of the three most important decay channels for a Higgs in this mass range: $H \to ZZ$, $H \to WW$, $H \to t\bar{t}$. Since the coupling to the gauge bosons is proportional to the square of the boson mass, these decays are the most important, and these processes dominate the width.
Since the width is proportional to the m_H^3 for a heavy Higgsboson, it is clear this effect will be more important for the width than the experimental resolution for a heavy Higgs.

4.4 Higgs coupling

If the SU(2) doublet Higgs field acquires a vacuum expectation value, couplings to gauge bosons and fermions arise directly from equations 3.42 through 3.47.
From these equations, one can find the coupling of the Higgs to other particles. One finds, for example, that the Higgs does not couple directly to photons, so the $H \to \gamma\gamma$ has to proceed some other mechanism, for example a t-quark loop.

The couplings to leptons are specified by the vertex factor -im/v, where m is the relevant lepton mass. The coupling of Higgs to quarks is of the same form. The vertex factor can be written

$$\frac{-ie * m_f}{2sin\theta_w m_W} \tag{4.2}$$

where θ_w is the Weinberg angle and m_W is the mass of the W boson.

The Higgs-fermion coupling is seen from equation 4.2 to be of order $m_f \ll m_w$, a condition which is satisfied for neutrinos, electrons and muons, and the light quarks. Hence, althogh it is possible to produce Higgs bosons in reactions initiated by these particles, the production rates are extremely small. For example, the contribution to the process $e^+e^- \rightarrow f\overline{f}$ coming from the Feynman diagram below will be extremely small, even for e^+e^- collisions at the total CoM energy $\sqrt{s} = m_H$, where the probability of the H resonance being formed is the largest.

The case is different for gauge bosons, however. It can be shown from the expressions for couplings between Higgs and vector bosons that the coupling is proportional to the squares of the masses of the gauge bosons.

4.5 Higgs decay in general

The Higgs boson decays into pairs of all massive particles. Through loop diagrams it can also decay into pairs of massless gluons and photons. An example of the latter is $H \rightarrow \gamma\gamma$ through a top-quark or W loop.
After a discovery of a Higgs particle it will be important to detect several decay channels to see wether the coupling strength is in proportion to the mass for all fermions as the standard model predicts, or not.

The width of the Higgs particle increases with increasing mass of the Higgs and approaches the value of the mass itself for a very heavy Higgs.
Also the branching ratios change dramatically across the possible range of the Higgs mass. This fact makes it necessary for different search strategies in different mass regimes.
Three main regions can be identified:

- m_H<120 GeV: the $H \rightarrow b\overline{b}$ decay mode dominates, since b-quarks are the most massive fermions kinematically accessible in this region.
- 130 GeV <m_H< 2*m_Z: the decays $H \rightarrow WW^{(*)}$ and $H \rightarrow ZZ^*$, where one of the vector bosons can be virtual, become important and eventually dominate.
- m_H > 2*m_Z: the Higgs boson decays mainly into WW or ZZ pairs, where both bosons are real.

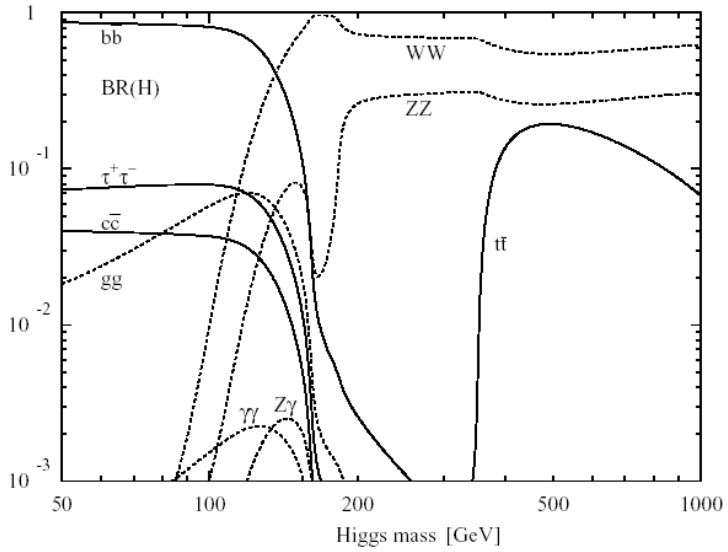

Figure 4.5: Branching ratios for the Higgs as a function of Higgs mass. Note that the cross section increases when the full phase space opens up for two real Z bosons. The dip in the branching ratios into Z is due to the increased probability for decay into W when the full phase space opens up for the W boson.

Decays such as H$\rightarrow \gamma\gamma$ are rare but provide clean signatures against the background. This is discussed below.
Higgs seeks to decay to as heavy particles as kinemetically allowed. In the mass range discussed in this thesis, the heaviest particles allowed are the top-quark, the Z^0 boson and the $W^{\pm}$. The coupling to the $t-$quark is linear, as seen from equation 4.3, [8], [4].

$$\frac{ig\,m_t}{2\,m_W} \tag{4.3}$$

However, the couplings to the gauge bosons are proportional to the mass of the W-boson squared. The vertex factor for $H \rightarrow ZZ$ is proportional with the expression given by 4.4 and the vertex factor for $H \rightarrow WW$ is proportional to 4.5.

$$\sim \frac{m_W^2}{cos^2\,\theta} = \sim m_Z^2 \tag{4.4}$$

$$\sim m_W^2 \tag{4.5}$$

Even though the $m_Z > m_W$ we see from figure 4.5 that the probability for decay into a pair of W-bosons is greater than for decaying into two Z bosons. The reason for this is that the matrix element for the $H \rightarrow ZZ$ should be multiplied with $\frac{1}{2}$ since the two Z bosons are identical particles appearing in the final state, [4].

4.6 Search strategy

The main channels which will be used at LHC to look for a Standard Model Higgs boson can be classified as follows, [11], [22]:

- Low mass region (m_H<130 GeV). Two decay modes are experimentally important in this region: $H \to b\bar{b}$ and $H \to \gamma\gamma$.
  The first one has a branching ratio close to 1 in most of this region, and therefore inclusive Higgs production followed by $H \to b\bar{b}$ has a large cross section (20pb). However, since the signal-to-background ratio for the inclusive production is smaller than 10^{-5}, it will be impossible to observe this channel above the QCD background. Even at trigger level it is impossible to select it because $H \to b\bar{b}$ does not have any high jet energy or isolated lepton in the final state that could be used as a trigger.
  However, the associated production $t\bar{t}H, WH, ZH$ with $H \to b\bar{b}$ with an additonal lepton coming from the decay of the accompanying particles, give rise to final states which can be extracted above the background. These processes have a much smaller cross section (<1pb), though. It also solves the trigger problem because requiring a high energy lepton from the $t-$quark of from the gauge bosons serves as trigger.
  The next step is to identify jets with b-quarks and b-tagging is used. B-tagging is based on the long lifetime of the b-quarks which causes secondary vertices. The jets from a b-decay do not come from the primary vertex, but a secondary one, because the b-quark travels around a cm before it decays.
  Since the Higgs mass has to be reconstructed from two jets, the resulting mass peak will be wide. This is because reconstruction from jets gives trouble with invisible energy from escaping neutrinos and energy lost outside the jet cone. In $Ht\bar{t}$ one also faces the problem of combinatorics since the $t-$quarks also decay into b-quarks and there is an ambiguity in chosing which b-jet to associate with the Higgs.

  The $H \to \gamma\gamma$ channel has a branching ratio at the level of 10^{-3} and therefore a small cross-section (50 fb). However, the signal-to-background ratio (10^{-2}) is much more favourable than for the $b\bar{b}$ channel. The trigger in this case is two isolated electromagnetic clusters in the EM Calorimeter and the background is mainly from direct photon production and jets faking photons.

- Intermediate mass region (130GeV <m_H<$2m_Z$). The most promising channels for the experimental searches are $H \to WW^* \to 2l + 2\nu$ and $H \to ZZ^* \to 4l$.

- High mass region ($m_H > 2m_Z$). This is the best region to discover a Higgs boson signal at the LHC, since the $H \to ZZ \to 4l$ channel gives rise to a gold-plated signature, almost background free. For very large masses ($m_H > 500GeV$) searches for this decay mode will be supplemented by searches for other channels, such as $H \to ZZ \to ll\nu\nu$ and $H \to WW \to l\nu jj$. These processes have a larger branching ratio and therefore can compensate for the decrease in the production cross section for Higgs when the Higgs mass increases.

The channel $H \rightarrow ZZ^{(*)} \rightarrow 4l$ can be observed in the mass region 120-700 GeV and gives rise to a very distinctive signature, consisting of four leptons. Electrons and muons are required since final states of taus do not allow clean reconstruction of the Higgs mass peak and are also contaminated by larger QCD backgrounds. The invariant mass of the four leptons are consistent with the nominal Higgs boson mass. The expected backgrounds and therefore the search criteria depend on the Higgs mass. We will below look at the two possibilities: one where both Z are on mass shell and one where one of the Zs is off mass shell.

4.6.1 Higgs-decay where one Z is off mass-shell

This channel provides a rather clean signature in the mass region between 120 GeV and 180 GeV. From figure 4.5, we see that the branching ratio for $H \rightarrow ZZ^*$ is quite big. A dip occurs however where the channel $H \rightarrow WW$ opens up.
A good mass resolution is required to reduce the continuum background, since the experimental resolution dominates over the intrinsic Higgs width in this mass range.
There are both reducible and irreducible background. The irreducible background stems from the continuum producion of ZZ^* and Zγ^* where these in turn decay into 4 leptons. The reducible backgrounds are from $t\bar{t}$ and $Zb\bar{b}$ production. Because of the large top production cross-section, the $t\bar{t}$ dominates. In addition to this, there is a source of background when two real Zs decay and one or possibly both decay into a pair of τ´s with subsequent leptonic decays into 4 leptons.
The main cuts to reduce the background are:

- Two isolated leptons with p_T>20 GeV and $|\eta|$<2.5 are required to trigger the experiment.
- Two additional isolated leptons with p_T>7 Gev and $|\eta|$<2.5 are required.
- One pair of leptons of right combination of charge and flavour is required to have an invariant mass in a window around the Z mass, defined as $m_Z \pm m_{12}$. This cut rejects most of the non-resonant $t\bar{t}$ background.
- The other pair of leptons is required to have an invariant mass above a certain treshold, above 20 GeV. This cut reduces considerably background both from $t\bar{t}$, $Zb\bar{b}$ and Zγ^*.

4.6.2 Higgs-decay where both Zs are on mass-shell

If $m_H > 2m_Z$, then both Z bosons in the final state are real and two pairs of leptons with same flavour and opposite sign should have an invariant mass compatible with the Z mass. In this region the backgrounds, such as irreducible $pp \rightarrow ZZ \rightarrow 4l$ are small. Furthermore, the intrinsic Higgs width is larger than the experimental mass resolution, therefore the detector performance is not critical.
The expected background is dominated by the continuum production of Z boson pairs

from $q\overline{q}$ and gg-fusion. In this mass region, the natural width of the Higgs boson grows rapidly with increasing m_H and dominates the experimental mass resolution for $m_H > 300GeV$. The momenta of the final-state leptons are high and their measurement does not put severe requirements on the detector performance. Therefore, the discovery potential in this channel is primarily determined by the integrated luminosity. We will in later chapter in detail study how a discovery of the Higgs might be done in this channel.

4.7 Limitations on the Higgs mass

Since the input parameters of the Standard Model are not predicted, the Higgs boson mass is unknown, but may be written as a function of the vacuum expectation value ν of the Higgs field, [29].

$$m_H = \sqrt{2\,\lambda}\nu \tag{4.6}$$

The current value of ν is 246 GeV, [29]
An upper limit on the Higgs mass can be given from several arguments. The socalled triviality bound is derived by considering the one-loop renormalization group equation and what is called the triviality argument, [4], [29]. An upper limit on the Higgs mass can then be derived

$$m_H^2 \leq \frac{4\nu^2\pi^2}{3\,ln\left(\frac{Q}{\nu}\right)} \tag{4.7}$$

where ν is the vacuum expectation value of the Higgs field and Q is the cut off energy. A 1TeV cutoff yields an upper bound about 750 GeV.
Another consistency argument refers to vacuum stability. The requirement that the vacuum is stable, limits m_H from below.
A third argument considers $WW \rightarrow WW$ scattering, [4]. To conserve unitarity, it is required that the scattering amplitude for this process is below unity. It can be shown that this puts a limit, $m_H < 1$ TeV.

Experimental lower bounds are set by experimental data. LEP2 and Tevatron provide these.

Chapter 5

Simulation and analysis tools

This study has been done using the PYTHIA 6.1 Monte Carlo generator and the ATHENA version 8.0.5 for the simulation of the ATLAS detector.

5.1 Event generator

The PYTHIA Monte Carlo generator can be used to generate high-energy-physics events. The emphasis is on multiparticle production in collisions between elementary particles which in this study is proton-proton collisions with the centre-of-mass energy 14 TeV, [21].
In an event generator, the objective is to use computers to generate events as detailed as could be observed by a perfect detector. This is done in several steps by factorizing the full problem into a number of components, each of which can be handled reasonably accurately. Basically, this means that the hard process is used as input to generate bremsstrahlung corrections, and that the result of this is then left to hadronize.

The Monte Carlo method is a numerical technique for calculating probabilities by using sequences of random numbers. For the case of a single, random variable, the procedure might be divided into three stages. First, a series of random values $r_1, r_2, ...$ is generated according to a uniform distribution in the interval $0 < r < 1$. Next, the sequence $r_1, r_2, ...$ is used to determine another sequence $x_1, x_2, ...$ such that the x values are distributed according to some probability density function. The values of x can be regarded as simulated measurements, and from them the probabilities for x to take on values in a certain region can be estimated.
When the Monte Carlo method is used to simulate experimental data, one can most easily think of the procedure as a computer implementation of an intrinsically random process. Probabilities are naturally interpreted as relative frequencies of outcomes of a repeatable experiment, and the experiment is simply repeated many times on the computer, [12].

To first approximation, all processes in PYTHIA have a simple structure at the level of interactions between the fundamental objects of nature, quarks, leptons and gauge

bosons. We might visualize the process at the LHC as proton-proton collisions. However, corrections to this picture is necessary. For example:

- Firstly, there are bremsstrahlung-type modifications, i.e. the emission of additional final-state particles by branchings such as $e \to e\gamma$ or $q \to qg$. Because of the largeness of the strong coupling constant, α_s, and because of the gluon self-coupling, QCD emission of quarks and gluons is especially prolific. We therefore speak about parton showers when one single parton may give rise to a whole bunch of partons in the final state.
- Secondly, there are true higher-order corrections which involve a combination of loop graphs and the soft parts of the bremsstrahlung graphs above, a combination needed to cancel some divergences.
- Thirdly, quarks and gluons are confined.

An eventgenerator can be used in many different ways. The main applications can be classified as below:

- To give physicists a feeling for the kind of events one may expect to find, and at what rates.
- As a help in the planning of a new detector, so that detector performance is optimized, within other constraints, for the study of interesting physics scenarios.
- As a tool for devising the analysis strategies that should be used on real data, so that signal-to-background conditions are optimized.
- As a method for estimating detector acceptance corrections that have to be applied to raw data, in order to extract the true physics signal.
- As a convenient framework within which to interpret the observed phenomena in terms of a more fundamental underlying theory.

5.2 The ATHENA framework

The event generator gives us the physics of a bare collision. In order to be able to extract information from a collision in an experiment, large detectors are used. In a simulation study, it is therefore important to analyze how the detector is affecting what happened in the collision and how the results will look for us.

The official code for fast simulation in ATLAS is Athena-Atlfast, an Object Oriented package written in C++. This code comes from a pre-existing Fortran version.
The purpose of the ATHENA architecture framework is to provide software which fulfils the requirements of the physicist developer and physiscist analysist in the construction

and use of programs for performing common tasks, such as reconstruction, detector simulation, visualization etc.

ATHENA has an object-oriented design, guaranteeing ease of use, flexibility and well-specified methods for using the services that the architecture provides.
The application framework consists of a number of component software blocks which have functionality provided by well-defined interfaces. These interfaces are the component's link to the outside world. Communication to and from this object can only take place in accordance with the rules specified by the methods defined on the interface.
Thus, the functionality of each software component is 'encapsulated' within the object, and any user of this object therefore does not, and should not, know how the object is performing its task.
This increases ease of use, as only the methods specified on the interface need to be known to make use of the object. Indeed, the functionality may change without the user ever realising, [28].

5.3 ATLFAST, design and functionality

The ATLFAST detector simulation package is a tool for simulating the key aspects of the ATLAS detector response in a parametrised way. It provides a list of stable, final-state particles from the event generator, [24]. More specific, using a list of monte carlo particles from PYTHIA, it produces the following output information:

- reconstructed jets
- isolated electrons and photons
- isolated and non-isolated muons
- missing transverse energy
- simple trigger response
- charged track parameters

In the analysis, ATLFAST is invoked after PYTHIA. ATLFAST is essentially a program for fast detector simulation and physics analysis. It can be used for fast event-simulation including the most crucial aspcts mentioned above. Jet reconstruction in the calorimeters, momentum/energy smearing for leptons and photons, magnetic field effects and missing transverse energy. It is important to note that ATLFAST offers only an approximate, parametrized simulation of the detector. A more realistic situation is to use full simulation.

The level of simulation is somewhere between parton-level and full simulation. It is as accurate as the full simulation at mass resolution, jet reconstruction efficiency and

missing transverse energy resolution. At reproducing efficiencies for lepton and photon isolation it is not as accurate as full simulation, however. The detector effects are simplified in ATLFAST compared to full simulation. It leaves out all effects due to details in the shape of particle showers in the calorimeters and charged track multiplicity in jets. The parameterization of photon, electron and muon momentum resolution, the hadronic calorimeter energy resolution and the effect of the ATLAS magnetic field on jet reconstruction are reasonably accurate, [18], [24].

5.4 The analysis software: ROOT

ROOT is an object-oriented framework aimed at solving the data analysis challenges of high-energy physics.
The phrase *framework* means that the basic utilities and services, such as I/O and graphics are provided by the program and the user does not have to make these things himself. ROOT, being a HEP analysis framework, provides a large selection of HEP specific utilities such as histograms and fitting.
The drawback of a framework is of course that the user is constrained to it and has to learn the framework interfaces.

Object-Oriented Programming offers considerable benefits compared to the old Procedure-Oriented Programming. Among these advanteges are

- Encapsulation: forces data abstraction and increases opportunity for reuse
- Sub classes and inheritance: make it possible to extend and modify objects
- Class hierarchies: provides a flexible mechanism for modelling real-world objects

In this study, version 3.10/01 of ROOT from October 2003 is used, [23] .

5.5 Higgs width calculation with Hdecay

Hdecay is a program for Higgs boson decays in the Standard Model and its supersymmetric extensions. The program is self-contained (with all subroutines included), and calculates the decay widths and branching raios according to the current level of theoretical knowledge.

Hdecay is written in FORTRAN 77. A small input file is used to tell the program what kind of Higgs boson that is to be considered and also the mass range of interest. The output is written to text files giving the calculated branching ratios and total width, [25]

Chapter 6

Some aspects of full simulation; detector performance

After a detailed simulation at parton level, the detector is simulated, as described in the previous chapter. Though ATLFAST might be a reasonably accurate approximation of the detector, full simulation might be called for in many circumstances.
An accurate description of the detector as possible might prove valuable in many stages of the experiment. Full simulation might reveal problems in the design with respect to the physics potential at a time when it is still possible to do something about it. The quality of the reconstruction can also be checked as well as the impact on the physics due to fakes and known detector imperfections. When the detector is running, a careful simulation is important for calibrations and the general understanding of the data. Ideally, full simulation must describe all cracks and dead channels as well as the correct noise patterns.
Though the full analysis of $H \rightarrow ZZ \rightarrow 4l$ will not be carried out using full simulation, some aspects of full simulation will be studied. Electron and muon reconstruction using full simulation and a comparison of full simulation and fast simulation of some aspects important to the discussion in this thesis, will be discussed.

6.1 Full simulation

Most important for the full simulation is that the detector is modelled in a correct and complete way. GEANT is a tool to visualize a particle interaction with a specific geometry. Every single, tiny detail in the detector design is implemented in the geometry. That is, every cable, all glue and all the material is included. Geant includes all the different types of interactions in a detector, such as radiation, multiple scattering, conversions of photons, and energy loss processes. This is done by following every particle as it passes through the detector, losing energy on its way while interacting with the material in the detector.

An important point is that the format of the full simulation output is the same as

for the later real, experimental data such that the reconstruction routines can be identical for the two streams.

ATLFAST differs from full simulation not only because it is a parametrization. It also runs the reconstruction.
In a real experiment, the output from the detector is a set of energy deposits, for example. It tells how much energy depositted in different parts of the EM Calorimeter, the leakage of energy into the Hadronic Calorimeter etc. The output also tells us where in the detector a particle has passed. We might for example have a set of hits in the ID and energy deposit in the EM Calorimeter. This information needs further treatment. When reconstruction is run, the information is translated into measured quantities. ATLFAST provides this information right away and also a set of high level physics objects, such as electrons, photons, muons and jets.

6.1.1 Electron reconstruction

The information from full simulation in ATHENA is stored in a combined ntuple called CBNT Athena. It provides information from several algorithms and contains a list of many variables with information from the reconstruction.
The information provided by the CBNT needs further refinement before the analysis can start. We need to construct high level physical objects from the set of hits, energy measurements etc.

The electron reconstruction in ATLAS starts with the identification of an electromagnetic cluster in the calorimeters, [27]. Cuts on the shower shapes in the first and the second sampling of the EM calorimeter and the leakage into the first sampling of the hadronic calorimeters are used to separate clusters produced by electrons or photons from clusters produced by jets.
The result from this is stored in the variable eg_IsEM, which is zero if the cluster survives the cuts. That is, electrons and photons have eg_IsEM=0 in the Ntuple. Since $\frac{E}{p} \approx 1$ for electrons, a cut on this value can be used to separate electrons from other charged particles. These cuts are as follows:

$$0.8 < \frac{E}{p} < 1.3,\ |\eta| < 1.37 \tag{6.1}$$

$$0.7 < \frac{E}{p} < 2.5,\ |\eta| > 1.37 \tag{6.2}$$

There are two tracking algorithms in the ATLAS software, xKalman and iPatRec. Here iPatRec is used. There is a clearly visible tail to the right in figure 6.1. The electron emits photons on its way due to bremsstrahlung processes. It can be shown that the angular distribution for photon emission is peaked in the direction of the electron. Because of this, the energy of the electron is correct reconstructed while the electron momentum is reconstructed too low. That is the reason for the tail to the right.

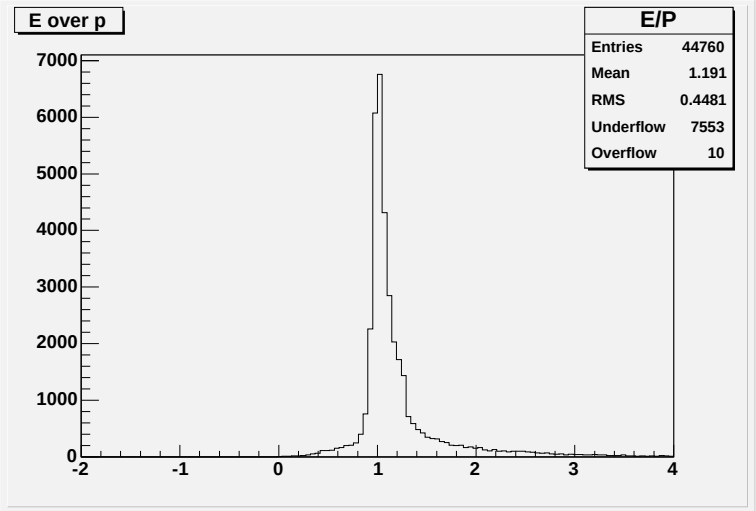

Figure 6.1: E over p for four clusters when a Higgs with mass 130 GeV has decayed. The clusters correspond to electrons. No cuts applied.

When it is demanded that the electromagnetic cluster should have a track in the ID, the E over p distribution becomes as in figure 6.2. To separate electrons from photons it is demanded that the energy deposit in the EM Calorimeter should have a matching track in the Inner Detector. This track should match the energy deposit both in space and in energy. That is, the tracks within a cone with $R = 0.07$ in the $\eta - \phi$-space are selected. The $\frac{E}{p}$ ratio should be ~ 1 when using the energy from the Calorimeter and the p_T that is calculated from the track information. The track should also be a good track with a small value of χ^2 and have several hits in the ID.

The electron efficiency is obtained by dividing the histogram of reconstructed electrons as a function of $|\eta|$ by that of the corresponding generated 'truth' electrons from PYTHIA. The cut on shower shape on reconstruction time is an efficient cut, according to [27]. To ensure isolated electrons from the MC-truth an isolation cut on $E_T < 5$ was applied with the egtruth_etIsol variable. This variable gives E_T found in the isolation cone around e/g position. In figure 6.3, a dip in the efficiency is visible in the region around $|\eta| = 1.5$. This is expected and corresponds to the transition between the central and the endcap region of the LAr calorimeter. It is also clear that the electron reconstruction efficiency is close to 0.9.
When the efficiency is plotted with ATLFAST in figure 6.4 two things become clear. First, the dip at $|\eta| = 1.5$ is absent, indicating that the fast simulation is not as detailed as full simulation. This is also evident from the shape of the distribution. The efficiency for ATLFAST is practically independent of $|\eta|$ while is not the case for full simulation. The efficiency is also lower. ATLFAST does not reconstruct leptons as efficiently as full simulation. In 6.4, the lepton reconstruction efficiency 0.9 is included.

The selection criteria for electrons in the ATLAS experiment are:

A detailed shower-shape analysis in the very fine-grained electromagnetic compartments

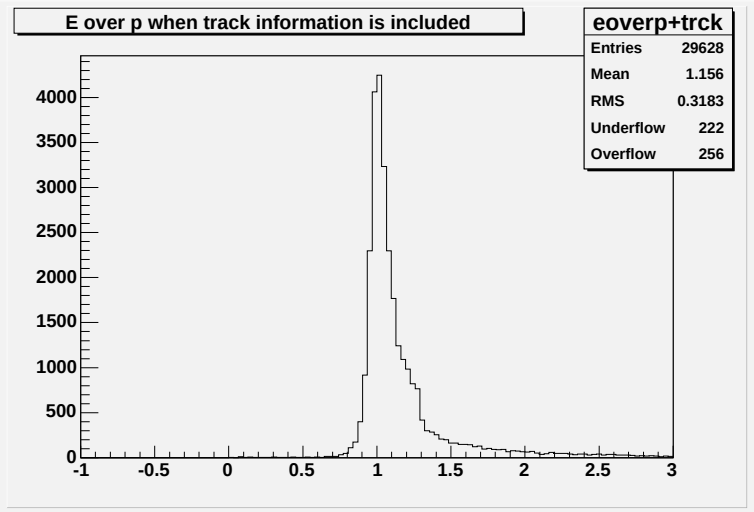

Figure 6.2: E over p when a corresponding track to the electromagnetic cluster is demanded. We see that the number of entries fall.

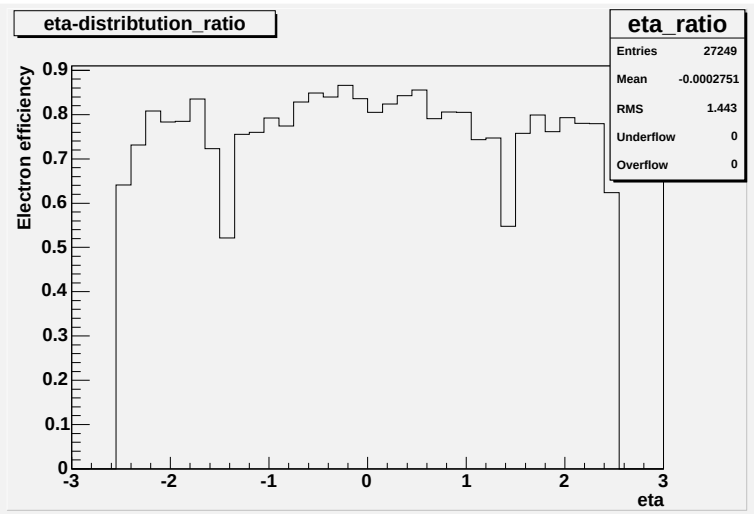

Figure 6.3: Electron efficiency as a function of $|\eta|$ when iPatRec has been used as tracking algorithm. This efficiency includes trigger efficiencies, geometrical acceptance and reconstruction efficiencies.

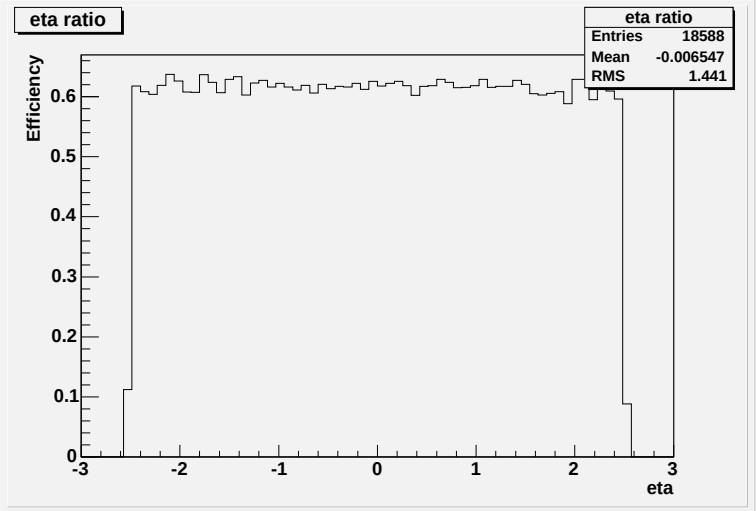

Figure 6.4: The electron efficiency as a function of eta obtained by ATLFAST. There is a lower efficiency whith ATLFAST over the whole pseudorapidity region and the reconstruction is not as detailed as with full simulation.

of the calorimeters, a search for high-p_T tracks and a match between the clusters and tracks. Further refinement is possible via the identification and correct treatment in case the electron has undergone Bremsstrahlung, the requirement of a transition radiation signal from the transition tracker (TRT) and the application of isolation criteria.

6.1.2 Muon reconstruction

The results shown for muons are from [27]. Athena contains two muon reconstruction packages, MuonBox and Moore/Muid. The selection criteria for muons are:

Muon: the muon selection will in a first step make use of the external muon spectrometer to determine the muon momentum and charge. A refinement of this information will then be obtained by searching for tracks in the Inner Detector and matching and combining these candidates with the muon track segment. Isolation criteria may also be applied, using for example information from the calorimeters.

Figure 6.5 shows the efficiency with which MuonBox finds muons as a function of $|\eta|$ for three different ranges of p_T with $p_T > 10$ GeV. This includes muons from B and D decays but not from $\pi-$decays and K decays. Muons from the latter can be found and reconstructed giving an efficiency of greater than one. However, an isolation cut will greatly reduce the number of muons from πs and Ks.
The plot shows that the efficiency is independent of p_T. The dip at $|\eta| = 0$ si due to gaps in the muon system for services. The efficiency is apart from this very good. However, the drop in efficiency for $|\eta| > 2$ is not understood, [27].

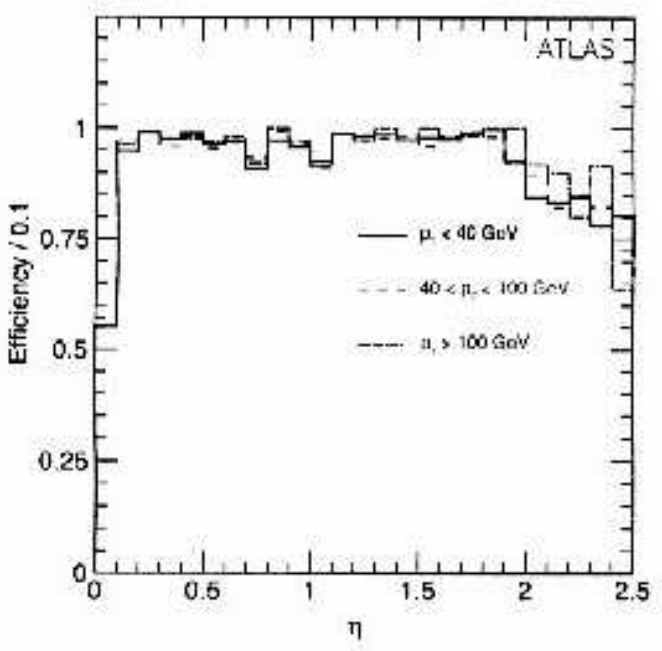

Figure 6.5: Muon reconstruction efficiency as a function of $|\eta|$ from MuonBox. From [27].

6.2 Detector Performance

When an electron with a certain energy, say 100 GeV hits the calorimeter, the measured energy will not in general equal exactly 100 GeV. There is a certain resolution for measuring the energy, or any other quantity. A slightly modified definition from the one found in [5] says:

Let z be the response of the detector when the quantity Z is being measured. The resolution is defined as the standard deviation σ_z of the distribution $D(z)$ in the measured quantity z for a monochromatic input distribution, $\delta(Z- < Z >)$.

When the energies and momenta of electrons and muons are measured, the detector's ability to measure these quantities precisely are important. It is also crucial to know the resolution of each measured quantity in the detector. Another point of interest is how well these aspects are simulated by the simulation software.

In [5] it was conducted a survey of the momentum resolution for electrons and muons at different momenta and different pseudorapidities. It is important to investigate the resolution for different momenta and different energies because $\frac{\Delta E}{E} \sim \frac{1}{\sqrt{E}}$ and $\frac{\Delta p}{p} \sim p$. To study the resolution at different pseudorapidities is important because the response and resolution is in general not the same in different parts of the detector.

Electron Resolution

Electrons with definite momentum was fired into the detector at different angles. It was shown that the momentum resolution gets better when the momentum increases. This is because the value of momentum is obtained from an energy measurement since $\frac{E}{p} \approx 1$. Since the resolution gets better for increasing energy, the momentum resolution gets better as well.
The measurement of electron energy and momentum in the ATLAS experiment will be carried out by a joint effort between the Inner Detector and the Electromagnetic Calorimeter.

Muon Resolution

Muon identification and reconstruction will be carried out by employing the Inner Detector and the Muon Spectrometer at ATLAS. Since the Muon Spectrometer is the sub-detector farthest from the collision point, the muons are subjected to multiple scattering, energy-loss fluctuations as well as the overall precision of the Spectrometer.

From figure 6.7 it is clear that the resolution in the muon momentum is dominated by different factors in different p_T intervals:

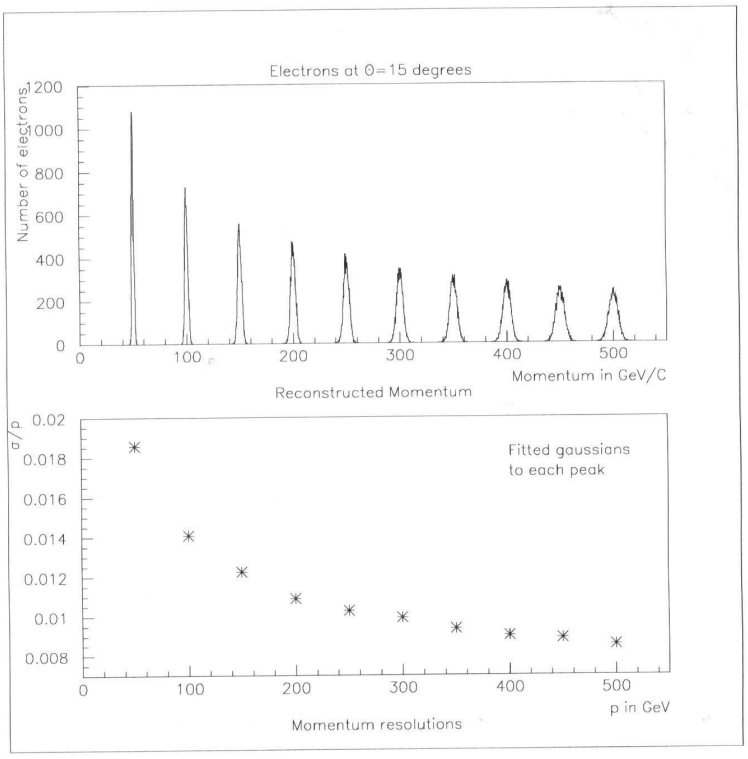

Figure 6.6: The momentum resolution for electrons as a function of momentum. The pseudorapidity is constant and equals 2.03. It is clear from the picture below that the momentum resolution gets better when the momentum increases. This is because the momentum can be calculated from the energy and $\frac{\Delta E}{E} \sim \frac{1}{\sqrt{E}}$ From [5]

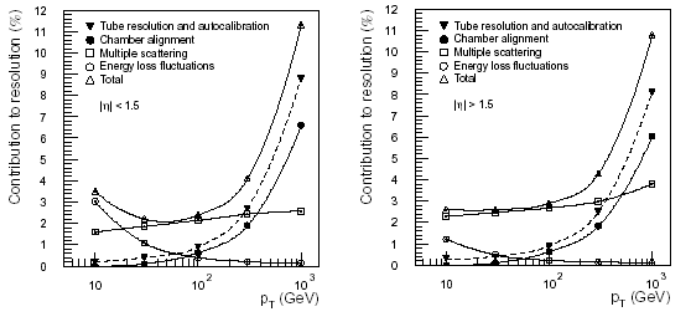

Figure 6.7: Contributions to the momentum resolution in the muon spectrometer. The values are averaged over $|\eta| < 1.5$ in the left figure and over $|\eta| > 1.5$

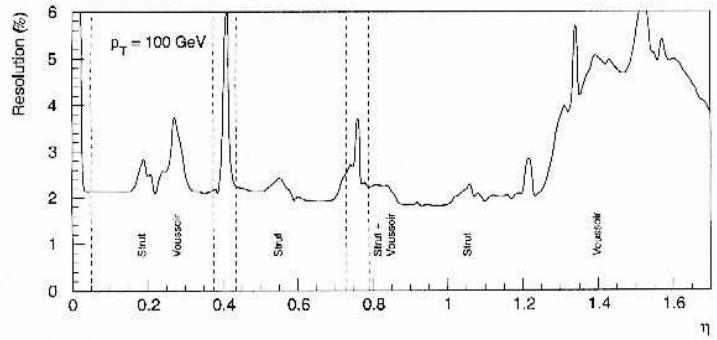

Figure 6.8: The transverse momentum resolution in the barrel-toroid region. Only the muon spectrometer is used here. From [7]

- p_T>300 GeV. The resolution is dominated by the precision of the magnetic field.
- 30 GeV <p_T < 300 GeV. The resolution is dominated by multiple scattering, hence the total amount of material traversed is vital.
- p_T<30 GeV, energy loss fluctuations in the calorimeter becomes important and dominates.

The effects of material obstructions and acceptance losses on the momentum resolution are clearly visible in figure 6.8. For example, many 'bumps' are visible. These correspond to values of η where the resolution is dominated by multiple scattering in voussoirs or struts of the barrel toroid, [7].

In figure 6.9 the performance of the muon spectrometer is plotted. For fixed values of p_T, the fraction of phase space over which the momentum resolution is better than a given value is shown. This figure illustrates that the momentum resolution of the muon spectrometer is better than 5% over 80% of the phase space for p_T between 10 GeV and 300 GeV.

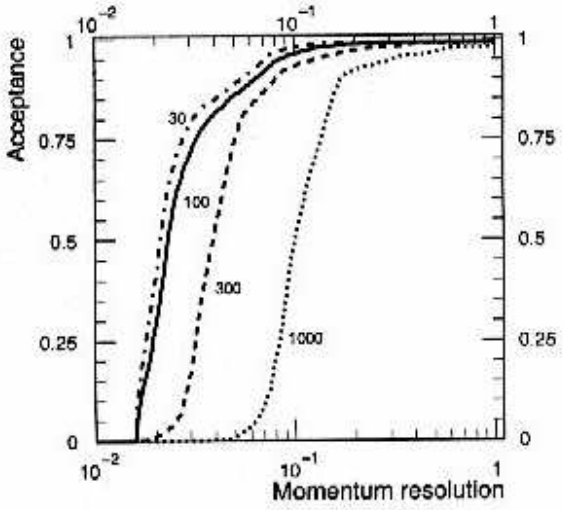

Figure 6.9: Correlation between acceptance and maximum momentum resolution. Only the muon spectrometer is used in the measurement. From [7]

Chapter 7

The analysis

This chapter describes the analysis. First, the signal (the process $H \rightarrow ZZ \rightarrow 4l$) and the background (all other processes with 4l in the final state) are reconstructed. In order to determine wether we can see the signature of a Higgs boson in the given mass range, we plot the invariant mass of the signal and the background. First, these are plotted in different histograms before they are plotted in the same histogram. From this S+B (signal+background) histogram, the significance is calculated for the signal. The significanse is a measure to which extent one can claim discovery of a new particle or not.

7.1 Introduction

The production of Higgs with PYTHIA is done by switching off all processes (msel=0) and then turning on the Higgs production setting the relevant ISUB numbers in the MSUB array. In this analysis, we are using ISUB=3, 102, 123, 124 to produce the Higgs. In addition, there are other, less important production channels. They are given by ISUB numbers 24, 26, 103, 121 and 122, and they have much lower branching ratio. The processes with ISUB numbers are listed in table 7.1. The production processes with a smaller branching ratio are summarized in table 7.2.

ISUB	PROCESS	$\sigma \times BR(mb)$	Fraction (%).
3	$f\overline{f} \rightarrow H$	2.661E-13	2.27
102	$gg \rightarrow H$	8.170E-12	69.82
123	$ff' \rightarrow ff'H(ZZfusion)$	7.740E-13	6.86
124	$ff' \rightarrow f''f'''H(W^+W^-fusion)$	2.063E-12	18.30

Table 7.1: The fraction of different Higgs production processes at a Higgs mass of 200 GeV.

These tables were made by generating 50000 events and comparing the cross section times branching ratio for Higgs decaying into two Z bosons times branching ratios for

ISUB	PROCESS	$\sigma \times BR(mb)$	Fraction (%)
24	$f\overline{f} \to ZH$	1.201E-14	0.11
26	$f\overline{f'} \to WH$	2.875E-13	2.55
121	$gg \to q\overline{q}H$	7.373E-14	0.65
122	$g\overline{q} \to q\overline{q}H$	5.071E-14	0.45

Table 7.2: The fraction of rare Higgs production processes at a Higgs mass of 200 GeV.

Higgsmass [GeV]	Cross section times branching ratio [mb]
200	1.118E-11
240	9.582E-12
280	7.865E-12
320	6.846E-12
360	6.718E-12
400	5.634E-12
500	2.802E-12
600	1.466E-12

Table 7.3: The production cross section times branching ratio of the Higgs boson for increasing Higgs mass. The branching ratio is also multiplied by branching ratio for Z decaying into leptons.

Z decaying into two leptons.
[1]

In a proton proton collider, the main production processes are 102, 123 and 124, i.e. gg, ZZ and WW fusion. Other processes of lower cross sections may be of interest, however, because of distinct final states which are easy to extract above the background. For example, in the case of $H \to b\overline{b}$, the direct production cannot be efficiently triggered nor extracted above the large QCD background. The associated production with a W or Z boson or a $t\overline{t}$ pair are the only possible processes to observe this signal. The leptonic decays of the W boson or semi-leptonic decyas of one of the top quarks provide an isolated high-p_T lepton for triggering and reduction of background. The Higgs-boson signal might thus be reconstructed as a peak in the invariant jet-jet mass spectrum of tagged b-jets.
Process 3 contains contributions from all quark flavours, but is dominated by the subprocess $t\overline{t} \to h^0$, i.e. by the contribution from the distribution of top quarks in the quark sea inside the proton. According to the PYTHIA manual, this process is known to overestimate the cross section for Higgs production as compared with a more careful calculation based on the subprocess $gg \to t\overline{t}h^0$, process 121. The difference between the two is that in process 3 the t and $\overline{t}$ are added by the initial-state shower, while in 121 the full matrix element is used. The price to be paid is that the complicated multibody

[1]The process with ISUB number equal to 103, $\gamma\gamma \to H$ has vanishing cross-section in PYTHIA and is switched off.

phase space in process 121 makes the program run slower. It would be double-counting to include the same flavour both with 3 and 121, [21].
The decay of the Higgs boson is controlled by the MDME switch. This switch makes it possible to turn on and off various decays channels for all particles. The decay of Higgs into two Z bosons is switched on and all other processes are switched off. Further on, each Z is allowed to decay into a lepton pair. The probability for Z decaying into leptons is the same for all flavours of leptons, around 3%.

We will only final states where the leptons come from Z bosons. That is, we will not take into consideration electrons and muons that come from tau lepton decay. Z decaying into taus will also be ignored.

$$\tau^+ \rightarrow \mu^+ + \nu_\mu + \overline{\nu_\tau} \tag{7.1}$$
$$\tau^- \rightarrow \mu^- + \overline{\nu_\mu} + \nu_\tau \tag{7.2}$$

The μ will decay further into electrons in the process

$$\mu^+ \rightarrow e^+ + \nu_e + \overline{\nu_\mu} \tag{7.3}$$
$$\mu^- \rightarrow e^- + \overline{\nu_e} + \nu_\mu \tag{7.4}$$

The tau can also decay directly into an electron. The probability that the tau will decay into an electrons is approximately the same as it will decay into a muon. The probability that a tau will decay according to one of the process above, is around 17%. Tau-leptons do not allow clean reconstruction of the Higgs mass peak since neutrinoes appear in the final state. The tau channel is also contaminated by large QCD background. Therefore we will not use final state with four electrons or muons originating from taus in reconstruction of the Higgs mass peak. States with four leptons coming from a Higgs decaying through a tau, could be considered as background. However, this background is rejected since the invariant mass of four leptons from this decay chain will not match the invariant mass of two Z bosons.

Let us consider the production cross-section times branching ratio for $H \rightarrow ZZ \rightarrow 4l$. We will denote this quantity B and define it as the production cross-section for Higgs, times the probability the Higgs will decay into two Z-bosons times the probability that one Z-boson will decay into 2 leptons squared.

$$B = \sigma \times Br(H \rightarrow ZZ) \times Br^2(Z \rightarrow ll) \tag{7.5}$$

where $l = e, \mu$.
In figure 7.1 B is plotted as a function of the Higgs mass. The shape of the plot reflects the fact that the production cross section for Higgs decreases for increasing Higgs mass, while the branching ratio for $H \rightarrow ZZ$ is approximately constant in the region of interest. The peak occurs where the full phase space of two real Z bosons opens up.
The plot is made using 30 runs with ATLFAST, two for every 5 GeV at low luminosity and 1000 events. B is plotted using the average of the two results at each point.

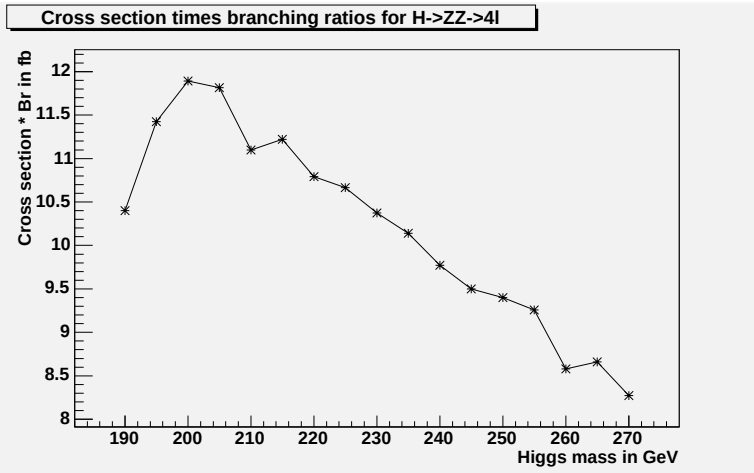

Figure 7.1: Cross-section times branching ratio for $H \rightarrow ZZ \rightarrow 4l$ as a function of Higgs mass at high luminosity.

7.1.1 Efficiency

The number of events in a histogram is given by the formula

$$N = \sigma L \epsilon \tag{7.6}$$

where N is the number of reconstructed events, σ is the cross-section and L is the integrated luminosity. ϵ is the efficiency.
The efficiency can be factorized into $\epsilon = \epsilon_{lepton} \times \epsilon_{cuts} \times \epsilon_{detector}$ where ϵ_{lepton} is the lepton reconstruction efficiency which is estimated to be 0.9 for each lepton in the ATLAS detector, [5]. ϵ_{cuts} is the efficiency of the cuts which are imposed and can be defined as

$$\epsilon_{cut} = \frac{events\ accepted}{events\ in\ total} \tag{7.7}$$

We will study the effect of cuts in great detail in the subsequent parts of this chapter. Of course we want high efficiency for signal and low efficiency for background.
$\epsilon_{detector}$ is the efficiency due to geometrical acceptance, ϵ_{geom}, trigger efficiency and other features of the detector and the data acqusition system.
To investigate the efficiency, a sample of 3930 events of $H \rightarrow ZZ \rightarrow 4l$ was generated. Table 7.4 shows how many events with four leptons that were reconstructed. We see that 2168 out of 3930 events are reconstructed with four leptons in the final state. This corresponds to an efficiency of 55.2%. In the remaining 1762 events one or more lepton is lost due to geometrical acceptance, trigger efficiency etc. For completeness, the effect of the cuts introduced in later sections is also included in table 7.4.

Figure 7.2 shows the number of final states with zero, one, two, three and four leptons in the final state.

It is important to note that ATLFAST does not include lepton reconstruction efficiency.

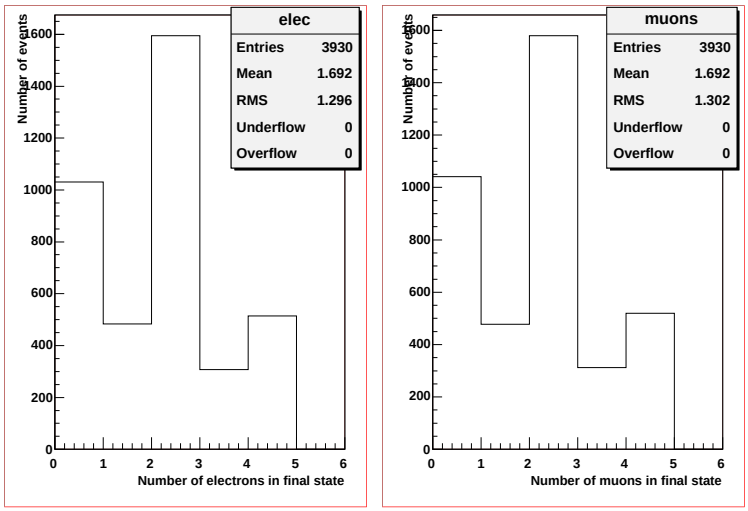

Figure 7.2: The lepton efficiency. The figure shows how many events in total with different number of leptons in the final state when a Higgs has decayed into four leptons.

Flavour	No cuts	One cut	Two cuts
4 electrons	514	511	383
4 muons	519	516	383
$2e, 2\mu$	1135	1123	838
Total	2168	2150	1604

Table 7.4: The capability of the ATLAS detector for reconstructing final states with four leptons from a Higgs boson with mass 320 GeV. The figures are the number of events with four leptons. 'One cut' refers to a cut on the p_T of leptons while 'two cuts' refers to an additional cut on the p_T of one of the Z bosons.

With reconstruction efficiency is understood the capability to identify a set of hits in the detector and energy measurements with a lepton. This is supposed to be 0.9 for every lepton. Consequently, each entry in table 7.4 should be multiplied with 0.9^4 to yield the correct number of accepted events.

Another point of interest is that ATLFAST does not handle for example pair production. It is not difficult to imagine an event where a Higgs has decayed into four leptons but where the leptons recovered are not the leptons from the Higgs. One or more leptons from the Higgs boson could for example be misidentified to be a part of a jet or an electron could be mistaken as a photon. If one or more electrons are then produced in pair production, we have an event with four leptons in the final state where not all leptons come from a Higgs. In this manner, events with more than four leptons can also be generated. From figure 7.2 we see that final states with more than four leptons do not occur with fast simulation. To study these things, full simulation is called for.
Another important issue, is that the detector's efficiency is a function of $|\eta|$. This sample corresponds to a Higgs with mass 280 GeV. With a more heavy Higgs boson for

example, the kinematics of the leptons would change and the sensitivity in that region of the detector could very well be different. However, it was shown in chapter six that ATLFAST's parametrization of the detector gives a lepton reconstruction efficiency constant in η.

To see how the background is reconstructed, we generate a sample of 45715 background events. From table 7.5 it is clear that only 14081 out of 45715 events are reconstructed which corresponds to 30.80%. To cut on the number of leptons is therefore a way to reduce the background since the fraction of kept events is smaller than for the signal. One reason that fewer background events are reconstructed with four leptons in the final state might be that background events tend to be minimum bias events with a higher probability to lose leptons down the beamline.

Flavour	No cuts	One cut	Two cuts
4 electrons	3507	3244	643
4 muons	3583	3407	718
$2e, 2\mu$	6991	6526	1281
Total	14081	13177	2642

Table 7.5: Reconstructed background events with four leptons in the final state. These numbers must also be multiplied with 0.9^4 to account for lepton reconstruction efficiency.

7.1.2 Definitions

Before the invariant mass of the signal is reconstructed, we need some definitions.

- Hard process: Initially two beam particles, in our case protons, are coming in towards each other. Normally each particle is characterized by a set of parton distributions, which defines the partonic substructure in terms of flavour composition and energy sharing. One shower initiator parton from each beam starts off a sequenze of branching, such as $q \rightarrow qg$, which build up an initial-state shower. One incoming parton from each of the two showers enters the hard process which is the head-on collision of these two partons. In the hard process a number of outgoing partons are produced, usually two, It is the nature of this process that determines the main characteristics of the event.

- Initial state radiation: Initial state radiation, ISR, is the emission of a photon or a gluon (or a massive vector boson) from one of the partons entering the hard process before the collision occurs.

- Final state radiation: Final state radiation, FSR, is the emission of a photon or a gluon (or a massive vector boson) from one on the partons in the hard process after the collision has taken place.

- Multiple interactions: the possibility that several parton pairs undergo hard interactions in a hadron-hadron collision, and thereby contribute to the overall event activity, in particular at low p_T.

We are going to reconstruct the invariant mass of four leptons coming from a Higgs boson of various masses. First, we switch off all physical effects, such as ISR, FSR, the width of the Higgs boson and multi-interaction. Then we turn these effects on and study how they affect the signal.
When we perform this part of the analysis, no attention will be paid to relative and absolute scaling of the histograms and we will use fairly large statistics. When we are going to calculate the signal significance, however, it is important that the histograms are drawn with correct relative and absolute normalization.

7.2 Reconstruction of the signal

When reconstructing the invariant mass of the Higgs-boson, events with four identified leptons are chosen. The leptons are required to be in the pseudorapidity range $|\eta| < 2.5$ with correct flavour and charge, i.e. the event should contain either two e^+e^- pairs, two $\mu^+\mu^-$ pairs or one e^+e^- pair and one $\mu^+\mu^-$ pair. Each lepton pair originates from a Z and hence the Z boson mass can be reconstructed by finding the correct pair of leptons. We will comment on this in later sections.

To reconstruct the Higgs mass, however, it is not necessary to know which leptons that originate from which Z. We know that when the background is neglected, all four leptons stem from the same Higgs boson. Therefore we use the formula for invariant mass to calculate the Higgs mass on the basis of the momenta and energies of the four leptons in each event.
The formula for the invariant mass of a particle that decays into four particles is

$$m_H = \sqrt{(\sum_{j=1}^{4} E_j)^2 - (\sum_{j=1}^{4} \mathbf{P_j})^2} \tag{7.8}$$

In order to calculate the significance of a potential discovery of the Higgs boson it is important to know what kind of curve that best fits the given distribution. The ATLAS TDR assumes that the distribution is best fitted with a Gaussian with a standard deviation which is a convolution of the Higgs width and the experimental resolution. In the following sections we will check this assumption.

In the next subsections, we are going to fit the mass distributions with various functions and it is appropriate to comment on the error in the width of the distributions in subsequent chapters. For a Gaussian distribution, the fractional standard deviation of s is approximately $\frac{1}{\sqrt{2n}}$ for n large, [31]. s is the standard deviation of the sample. So we have the following expression for the error in the standard deviation for a fitted curve:

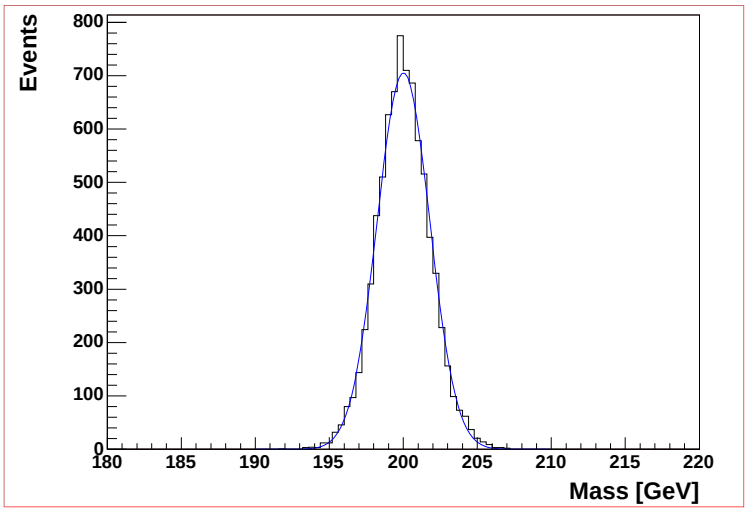

Figure 7.3: The invariant mass of four electrons originating from a Higgs boson with mass 200 GeV. The histogram is fitted with a Gaussian. All physical effects such as isr, fsr, multiple scattering and the width of the Higgs, are turned off. Refer to table 7.6 for the standard deviation for the fitted Gaussian

$$\Delta s = \frac{s}{\sqrt{2n}} \tag{7.9}$$

where n is the number of entries in a histogram. This number is in the subsequent sections fairly large, and the errors in the errors are omitted over the whole.

7.2.1 All physical effects switched off

The expression for the fitted distribution given in the TDR is given by

$$\sigma_m = \sqrt{(\frac{\Gamma_h}{2.36})^2 + (0.02 * m_H)^2} \tag{7.10}$$

where Γ_h is the intrinsic width of the Higgs boson and m_H is the Higgs-mass.[2]
Since all physical effects now have been switched off, this expression reduces to

$$\sigma_m = 0.02 * m_H \tag{7.11}$$

When the intrinsic width of the decaying particle is ignored, the resulting width of the mass plot is a function of experimental effects only. As discussed in chapter 2 on experimental methods, the energy and momentum resolution for electrons and muons is not a constant as a function of energy. The term $0.02 * m_H$ is an approximation of the detector effects that influences on the broadness of the distribution, [7].

[2]The relationship between the width (full width at half maximum), Γ, and the standard deviation, σ, is $\Gamma = 2.35\sigma$

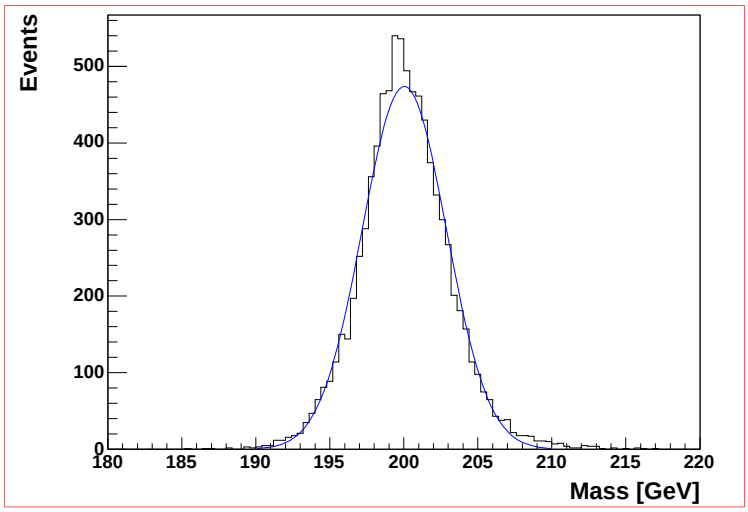

Figure 7.4: The invariant mass of four muons from a Higgs with mass 200 GeV. All physical effects are turned off. Note the the broader distribution compared with the electrons in figure 7.3. Refer to table 7.6 for the standard deviation of the fitted Gaussian.

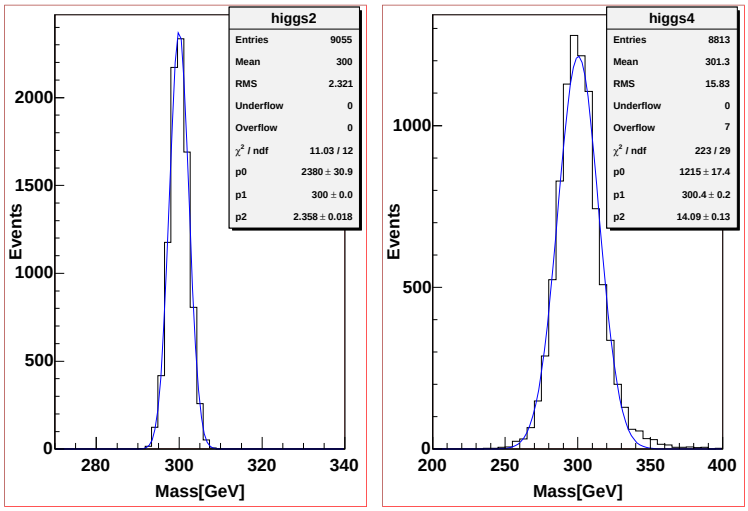

Figure 7.5: The invariant mass of four electrons and four muons from a Higgs boson with mass 300 GeV. Initial state, final state radiation is switched off as well as Higgs width and multiple scattering. The left figure shows the electrons while the right figure shows the muons. Refer to table 7.6 for the standard deviation of the fitted Gaussians.

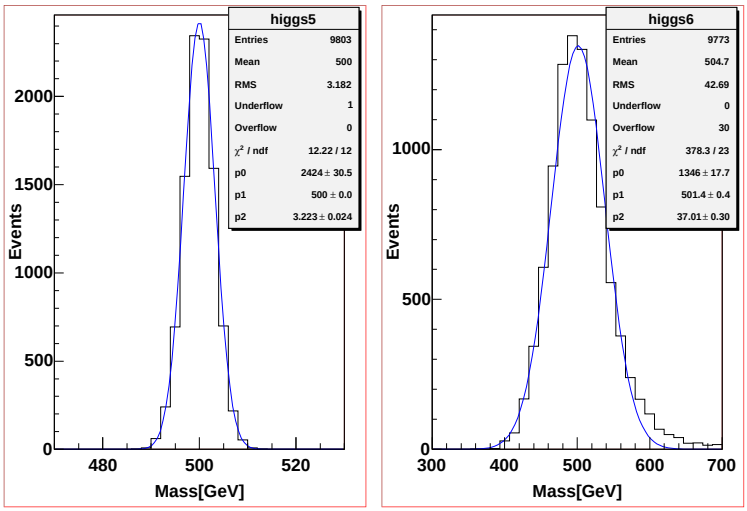

Figure 7.6: The invariant mass of four electrons and four muons from a Higgs boson with mass 500 GeV. Initial state and final state radiation is switched off as well as Higgs width and multiple scattering. Left corresponds to electrons and right to muons. Refer to table 7.6 for the standard deviation of the fitted Gaussians.

It is clear from figures $6.3-6.6$ that the width is different for electrons and muons. This is because the experimental resolution is very different when one measures the momenta and the energy of a particle.
The experimental resolution when measuring energy is given by

$$\frac{\Delta E}{E} \approx \frac{10\%}{\sqrt{E}} \oplus 1\%$$

while the experimental resolution when measuring momentum is given by

$$\frac{\Delta p}{p} \sim p$$

so it is clear that the relative uncertainty gets better when energy measurements are performed for increasing energy while the resolution gets worse when momenta measurement are performed at higher momenta, [7].
For electrons, the energy is measured in the electromagnetic calorimeter and the momentum is measured on basis of tracking. For muons the momentum is measured and the energy is calculated from the momentum.

The experimental resolution for electrons is for all Higgs masses comparable to [5] but the experimental resolution for muons is significantly bigger than in [5] and [7]. In order to investigate this, an approximate value of the experimental resolution for electrons and muons was calculated.
The starting point for these calculations was the energies and momenta for four electrons or four muons from the decay of a 500 GeV Higgs without any intrinsic width. One standard deviation for energy and momentum was added at the same time for each

m_H	$\sigma_{electron}$	σ_{muon}	$\sigma_{0.02*m_H}$
200	1.79	5.94	4
300	2.36	14.01	6
500	3.22	37.01	10

Table 7.6: The standard deviations from the fitted Gaussians in GeV. All physical effects except pure detector resolution are switched off. The TDR-parametrization of the detector resolution is shown for comparison.

lepton. In each case, the mass difference was calculated. The resolutions in energy, angles and momenta were taken from [7]. For each lepton, a mass difference was obtained and an approximate value for the detector resolution would then be the square root of the sum of the squared mass-differences.
For electrons, the experimental resolution was calculated to be ~ 3.8 GeV.
For muons, the resolution in energy and momentum was calculated to be ~ 28.8 GeV.
The formula used is presented in equation 7.12.

$$m_H^k = \sqrt{(\sum_{j=1}^{4} E_j + \Delta E_k)^2 - (\sum_{j=1}^{4} \mathbf{P_j} + \mathbf{\Delta P_k})^2} \tag{7.12}$$

where $k = 1, 2, 3, 4$.

$$\Delta \mathbf{P_j} = \sqrt{\left(\frac{\partial \mathbf{p_x}}{\partial |\mathbf{p}|}\mathbf{\Delta}|\mathbf{p}|\right)^2 + \left(\frac{\partial \mathbf{p_y}}{\partial \theta}\mathbf{\Delta}\theta\right)^2 + \left(\frac{\partial \mathbf{p_z}}{\partial \phi}\mathbf{\Delta}\phi\right)^2} \tag{7.13}$$

The components of the momentum are given in spherical coordinates.
These results are in reasonable agreement with the standard deviations in table 7.6 for the experimental resolution. See also appendix B.
To conclude: the resolution for the energy and momentum for electrons and muons as given in [7] lead to an approximate value for the standard deviation of the invariant mass plot which is in agreement with the standard deviations given in table 7.6.

7.2.2 Higgs width switched on

See table 7.7 for the width of the higgs boson as a function of mass. The width of the Higgs is calculated using HDECAY which is a program for calculating among other things, widths for Standard Model and Supersymmetric Higgs bosons.

When the Higgs width is included in the simulation, the distribution should have a width comparable to the convoluted width as given by equation 7.10. In figure 7.7 is plotted the sigmas of the fitted Gaussians as well as the sigmas expected from 7.10. However, when 7.10 was applied, $0.02m_H$ was replaced with the expressions for the

Higgsmass [GeV]	Width [GeV]
100	0.2598E-02
200	1.426
300	8.505
400	29.27
500	67.89
600	122.9

Table 7.7: The width of the Higgs boson for increasing Higgs mass.

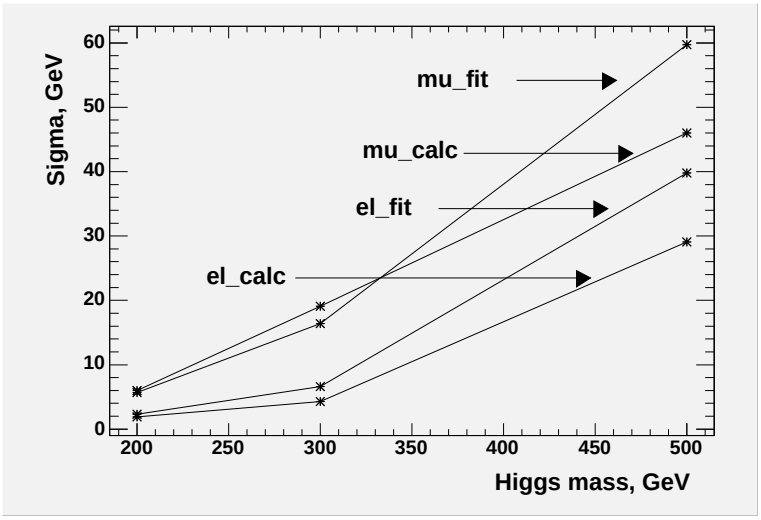

Figure 7.7: The standard deviations of fitted Gaussians as well as calculated widths.

experimental resolution obtained in the previous section.

Narrow particle states which are broadened significantly by experimental resolution will tend to have a Gaussian shape, while wide states for which the experimental resolution is less important may be more nearly Breit-Wigner shaped. A relatively light Higgs where the experimental resolution is the most important will therefore have a more Gaussian form than a heavier one where the Breit-Wigner form is more dominant.

From the plots 7.8 to 7.10 it is clear that the width increases compared to the plots when the intrinsic width was not included. It is also evident that the effect of increased Higgs' width is more important for a heavy Higgs.

We also see that there is a difference between electrons and muons. This is because the experiemental resolution can not be ignored compared to the intrinsic widht of the Higgs.

7.2.3 ISR and FSR switched on.

When we turn on initial state and final state radiation we allow for emission of photons and gluons from the incoming partons and from the partons after the collision.

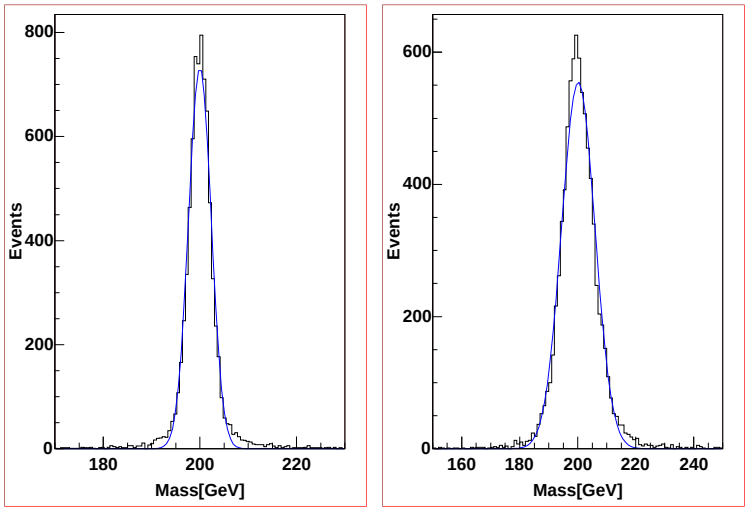

Figure 7.8: The invariant mass of four electrons and four muons from a Higgs with mass 200 GeV. Now the Higgs width has been included. The left figure corresponds to electrons while the right one is for muons. Refer to table 7.8 for the standard deviations of the fitted Gaussians

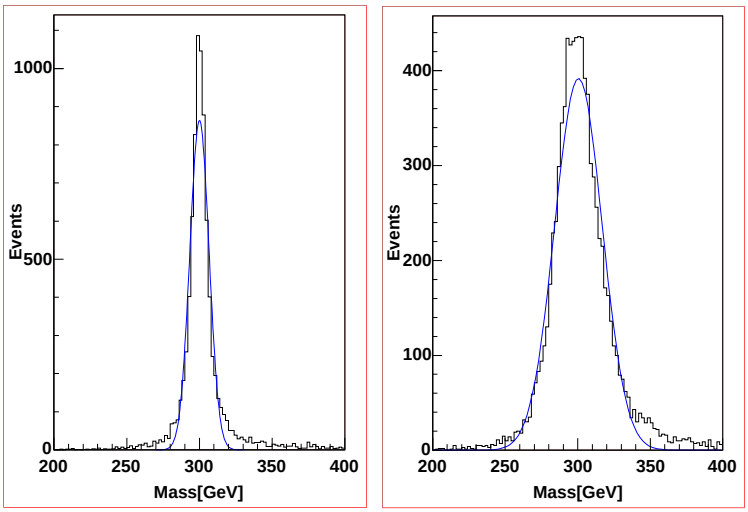

Figure 7.9: The invariant mass of four electrons and four muons from a Higgs with mass 300 GeV. The Higgs width is included. The histograms have been fitted with Gaussian distributions and we clearly see that the agreement is not too god anymore. As before electrons to the left and muons to the right. Refer to table 7.8 for the standard deviations of the Gaussians.

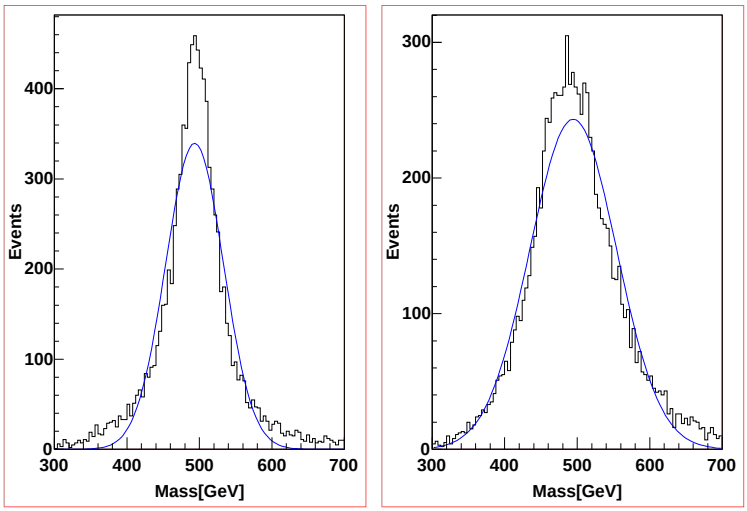

Figure 7.10: The invariant mass of four electrons and four muons from a Higgs with mass 500 GeV. The Higgs width is included and is more important than the experimental resolution. The Gaussian distribution is no longer a very good approximation to the histogram. Electrons to the left and muons to the right. See table 7.8 for the standard deviations of the Gaussians.

m_H	$\sigma_{electron}$	σ_{muon}
200	2.34	5.72
300	6.58	16.35
500	39.83	59.72

Table 7.8: The standard deviations from the fitted Gaussians in GeV. The intrinsic Higgs width has now been included in the simulation. Wee see that this affects the width of the fitted Gaussians and it is most prominent for heavy Higgs since the widht of the Higgs increases proportional to m_H^3 for heavy Higgs.

The ISR and FSR effects result in a slightly broader distribution. But the most pronounced effect are the tails that now appear because of ISR and FSR. These effects are most important for electrons because the cross section for emission of ISR and FSR is proportinoal to the inverse of the mass squared. The mass of the muon is approximately 200 times the mass of the electron. ISR and FSR are the most important effects for energy loss in matter for electrons and muons. For muons and other heavy particles, inelastic collisions with the atomic electrons of the material are the dominant reasons for energy loss.

7.2.4 All effects included

When the effect of multiple scattering is inlcuded in the simulation, this does not affect the mass distribution. This is clear from the values of the widhts in table 7.9 and table

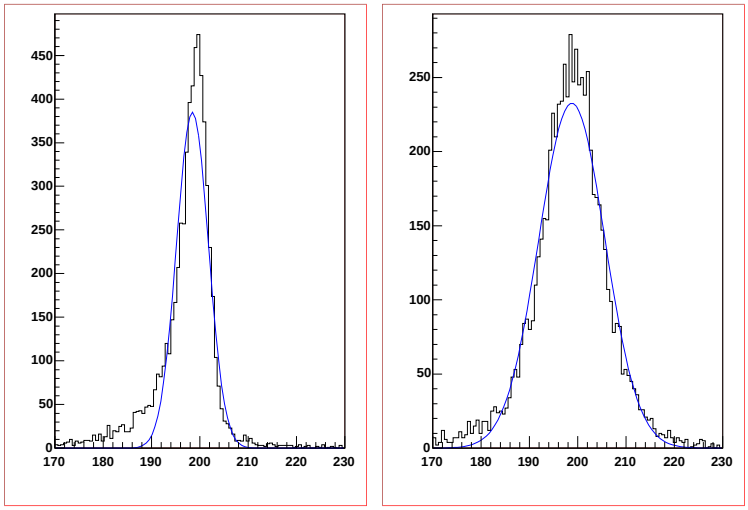

Figure 7.11: Invariant mass of four electrons and muons from a Higgs with mass 200 GeV boson when initial state and final state radiation have been added as well. We see that Gaussian distributions no longer fit very well and that the width of the fitted Gaussian increases. See table 7.9 for the sigmas of the fitted Gaussians.

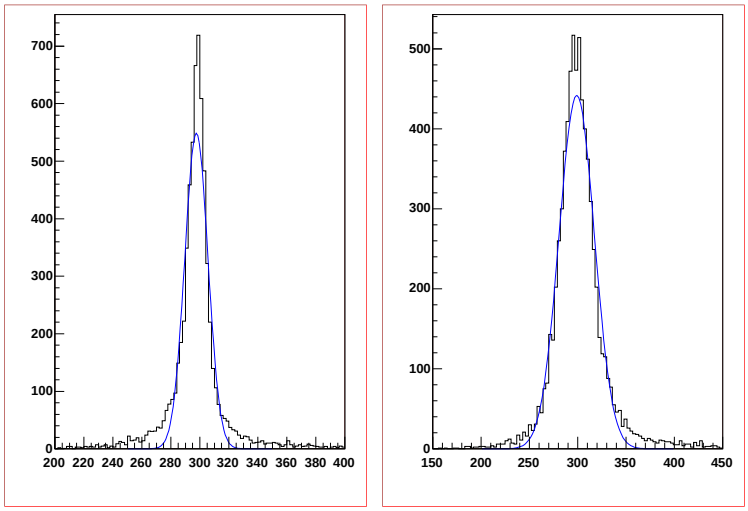

Figure 7.12: Invariant mass of four electrons and muons from a Higgs with mass 300 GeV boson when initial state and final state radiation have been added as well. We see that Gaussian distributions no longer fit very well and that the width of the fitted Gaussian increases. See table 7.9 for the sigmas of the fitted Gaussians.

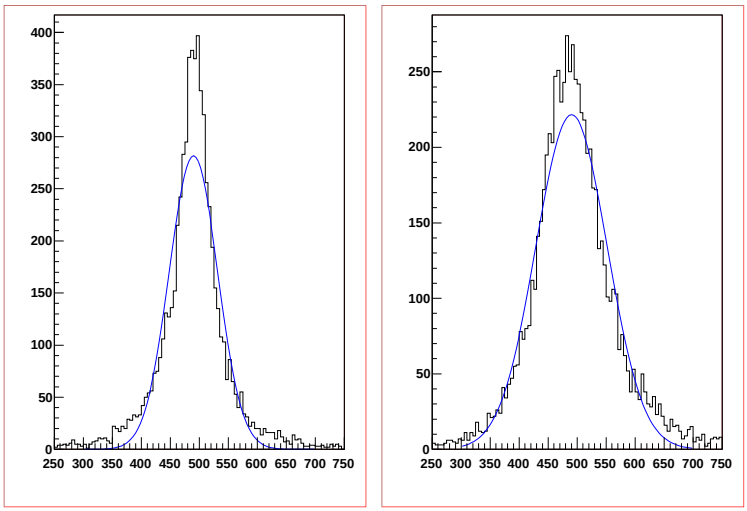

Figure 7.13: Invariant mass of four electrons and muons from a Higgs with mass 500 GeV boson when initial state and final state radiation have been added as well. We see that Gaussian distributions no longer fit very well and that the width of the fitted Gaussian increases. Refer to table 7.9 for the standard deviations of the fitted Gaussian distributions.

m_H	$\sigma_{electron}$	σ_{muon}
200	3.3	6.84
300	8.00	18.26
500	41.62	61.47

Table 7.9: The standard deviations from the fitted Gaussians. Now the ISR/FSR is also considered in addition to the intrinsic width of the Higgs in the simulation. We see a slighly broader distribution.

7.10.

7.3 Fitting of histograms

The purpose of this section is to determine what kind of curve which best fits the shape of the invariant mass plot of Higgs bosons of different mass.

It was seen in the previous section that the Gaussian distribution is not appropriate to fit the signal when we take into consideration initial state radiation, final state radiation and the intrinsic Higgs width. The Gaussian was only appropriate when these effects were neglected and only experimental effects occured.

When calculating the significance of a signal, the curve that best fits the histogram is important. It is therefore necessary to determine what kind of distribution this is. As

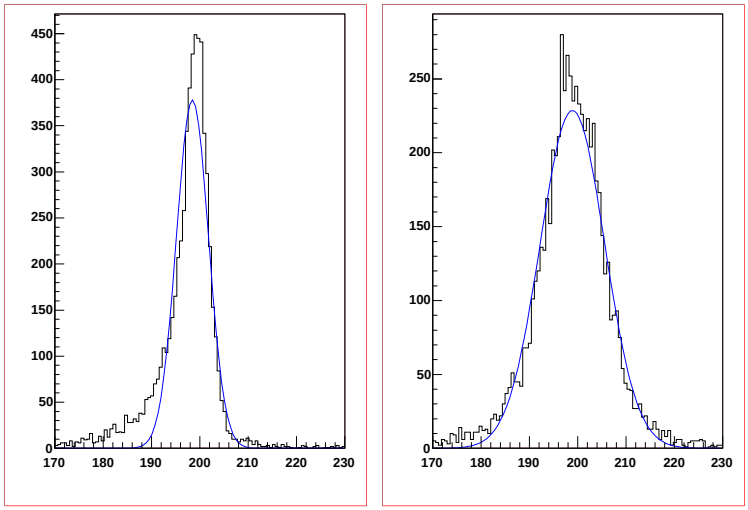

Figure 7.14: The invariant mass of a Higgs of 200 GeV when the experimental resolution, the intrinsic Higgs width, isr/fsr and multiple interaction are included. Refer to table 7.10 for the standard deviations of the fitted Gaussians.

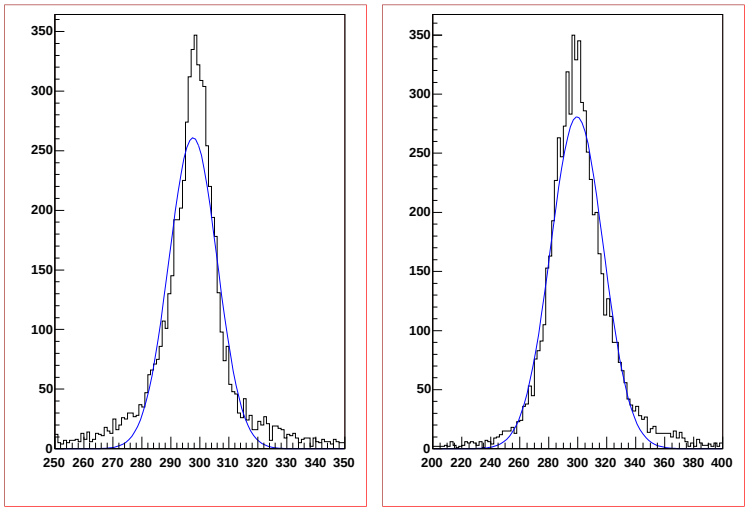

Figure 7.15: The invariant mass of a Higgs of 300 GeV when the experimental resolution, the intrinsic Higgs width, ISR/FSR and multiple interaction are included. Se table 7.10 for the sigmas of the Gaussians.

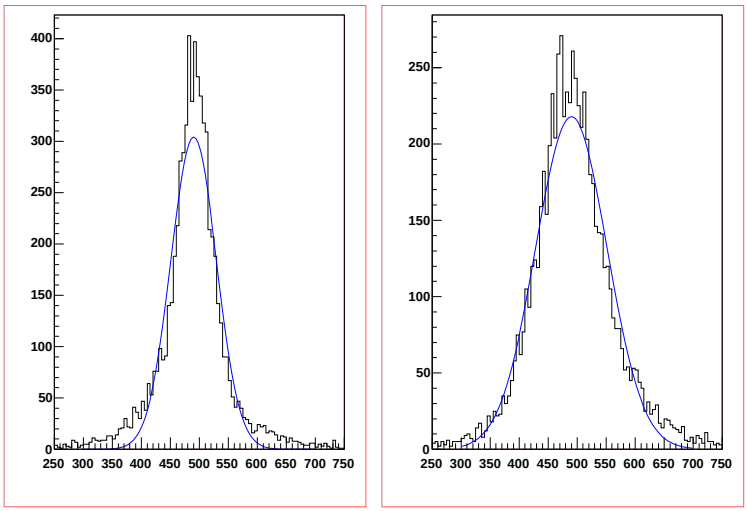

Figure 7.16: The invariant mass of a Higgs of 500 GeV when the experimental resolution, the intrinsic Higgs width, ISR/FSR and multiple interaction are included. In table 7.10 the sigmas of the Gaussians are listed.

m_H	$\sigma_{electron}$	σ_{muon}
200	3.32	6.66
300	8.32	18.21
500	39.18	61.45

Table 7.10: The standard deviations from the fitted Gaussians when all effects are included. The width in this table and in table 7.9 are the same.

was seen in section 6.2, a Gaussian distribution is the best choice when experimental effects are taken into account. The Breit-Wigner distribution takes into account the tails and the shape of the distribution if experimental effects are neglected. And indeed, a sum of a Gaussian and Breit-Wigner gives the best shape of the curve when fitting the histograms. This is not only due to a better χ^2/ndf for such a function, but is also reflected in a higher number of 'found' events when integrating a sum of Breit-Wigner and a Gauss, than when integrating only a Breit-Wigner or only a Gaussian.

Gaussian and Breit-Wigner distribution

The Gaussian (or normal) probability distribution function (p.d.f) of the continuous random variable x is defined by

$$f(x;\mu,\sigma^2) = \frac{1}{\sqrt{2\pi\sigma^2}} exp\left(\frac{-(x-\mu)^2}{2\sigma^2}\right) \tag{7.14}$$

where μ and σ^2 denote the mean and variance of the p.d.f

The Breit-Wigner p.d.f. of the continuous variable x is defined by

$$f(x;\Gamma,x_0) = \frac{1}{\pi}\frac{\Gamma/2}{\Gamma^2/4+(x-x_0)^2} \tag{7.15}$$

where the parameters x_0 and Γ correspond to the mass and width of a resonance particle.

An unstable particle may be characterized by its lifetime at rest, τ, or equivalently by its natural decay width $\Gamma = 1/\tau$. For heavy states, as the Higgs, that can not be directly observed, the lifetime is inferred from peaks in the mass distributions and it can be shown that the shape of these peaks is best described by the Breit-Wigner distribution.

In general, the particle will decay through a number of different channels. A heavy Higgs will for example in most cases decay into two Z bosons, two W bosons or a $t\bar{t}$ pair. The total decay width Γ is equal to the sum of the partial decay widths for the various channels.

In the plots in figures 7.17 and 7.18 all effects such as ISR, FSR and multiple scattering have been included and both electrons and muons are considered.[3] As will be explained later, when we calculate the significance we need both the fitting function of the signal and the fitting function of the background when both the cuts on the p_T of the leptons and the cuts on the p_T of the Z have been applied. Since the cuts depend on the Higgs mass, it is necessary to find these functions both for signal and background for the different Higgsmasses.

m_H	True	Int BW	eff_{BW}	χ^2/ndf BW	Int Gauss+BW	eff_{BWG}	χ^2/ndf BWG
200	949	855	0.9	60/52	875	0.92	44/51
240	1512	1338	0.88	86/56	1370	0.9060	60/56
280	1604	1411	0.88	111/65	1470	0.92	68/64
320	1504	1333	0.88	115/70	1360	0.90	90/69
360	1562	1379	0.88	124/68	1433	0.92	75/67
400	1362	1100	0.81	133/65	1150	0.85	95/64
500	730	583	0.80	90/45	622	0.85	44/44
600	387	296	0.76	31/26	328	0.85	23/25

Table 7.11: The table shows the relation between the true number of signal events and the number events recovered when integrating a Breit-Wigner distribution and a Breit-Wigner+Gaussian distribution in the mass window $\mu \pm 2 * \sigma$

[3] That is, we include all three channels, $4e, 4\mu$ and $2e2\mu$

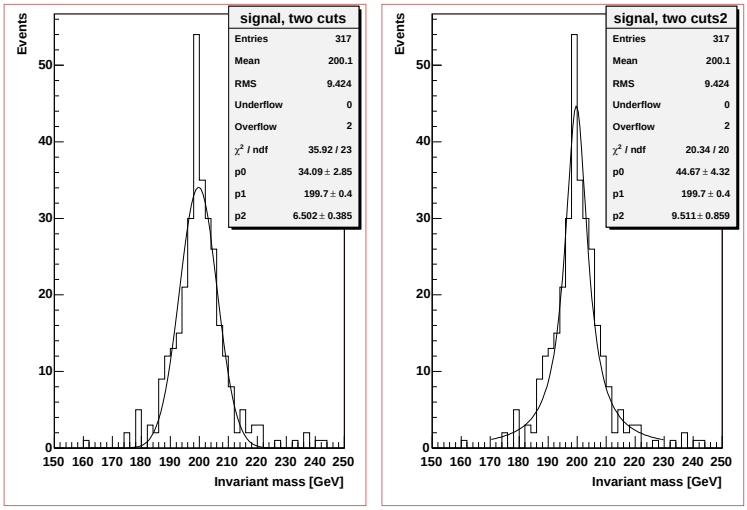

Figure 7.17: The signal from a 200 GeV Higgs. In the left figure the distribution is fitted with a Gaussian and in the right figure the distribution is fitted with a Breit-Wigner distribution. The Gaussian is broader than the Breit-Wigner, thereby including more of the events on the sides but the Breit-Wigner is higher and fits the tails of the distribution better.

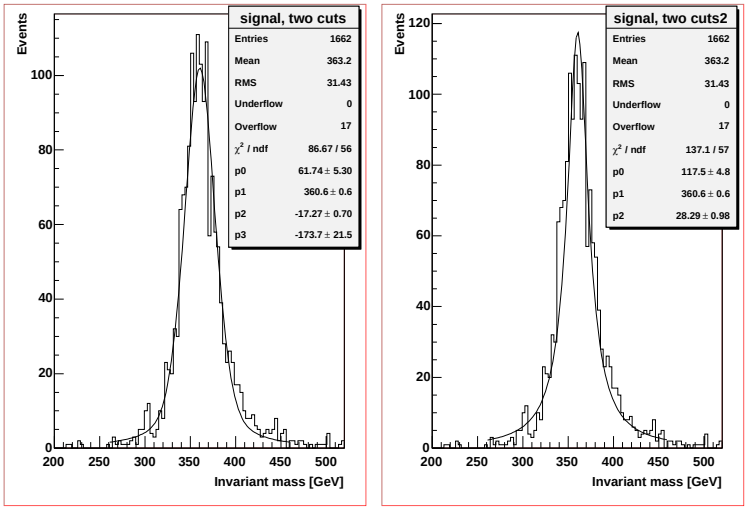

Figure 7.18: The signal from a 360 GeV Higgs. In the figure to the left the distribution is fitted with a sum of Breit-Wigner and a Gaussian distribution. In the right figure the distribution is fitted with a Breit-Wigner only. Since the value of χ^2/ndf is closer to one, this is a better fit to the histogram.

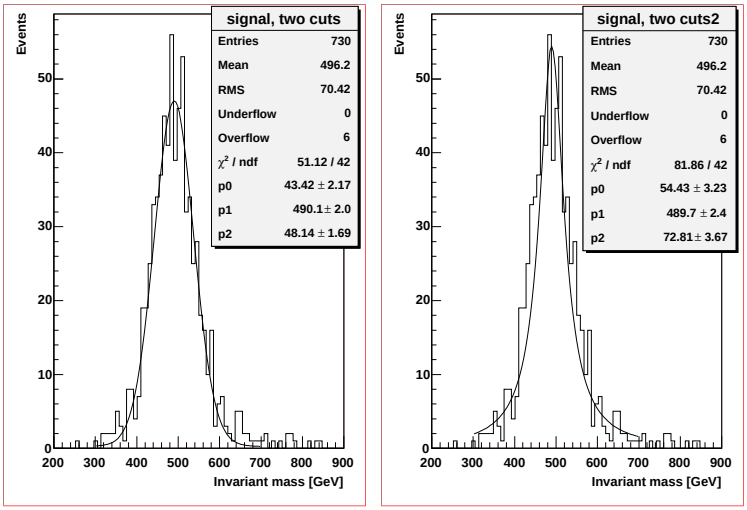

Figure 7.19: The signal from a 500 GeV Higgs. In the left figure the distribution is fitted with a Gaussian pluss a Breit-Wigner and in the left, the fit is a Breit-Wigner.

7.4 Background

For the $H \to ZZ \to 4l$ signal in the mass range $200 < m_h < 600$ GeV, the dominant background is the continuum production of two Z bosons through $q\overline{q} \to ZZ$ and $gg \to ZZ$ where the two Z bosons decay further into 4l. The total production cross-section times branching ratio is given in [10] as 44 fb for $m_{ZZ} > 200GeV$.
For 20000 generated background events, the production cross section times branching ratio was 70.63 fb. According to [5] and [10], the same cross section times branching ratio is 63.3 fb, which is 11% lower. The reason for this is other choices of default PDFs. [4] The choice of pdf is set by MSTP(51) and the default function is now CTEQ 5L, as opposed to CTEQ 3L which was the previous default function. Table 7.12 shows the cross sections for different choices of parton distribution functions.

Parton distribution function	Cross section [fb]
CTEQ 5L (leading order)	70.8
CTEQ 3L (leading order)	63.4

Table 7.12: The table shows the cross section for different choices of PDF's

The only way to generate the background in PYTHIA is through the ISUB=22 process, $q\overline{q} \to ZZ$. However, this is not the only way to produce two Z bosons in nature since gluons also contribute through $gg \to ZZ$. Therefore, the cross section for $q\overline{q}$ is multiplied by 1.3. according to [10] and [14].
The mass distribution for the leptons produced in $q\overline{q} \to ZZ$ is shown in figure 7.30. We

[4] PDF: parton distribution function. Is a parametrization of the energy and momentum distribution shared by the partons (quarks and gluons) in a hadron.

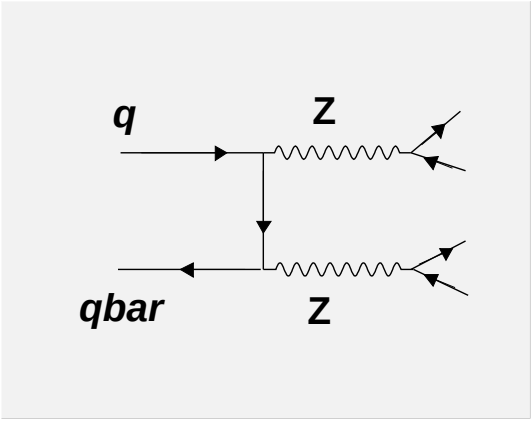

Figure 7.20: Feynman diagram of the irreducible $q\overline{q}$ background. The lines to the left corresponds to an incoming quark and an incoming anti-quark which each emits a Z^0 boson (the wavy lines). Each Z^0 decays into two leptons (the four lines to the right)

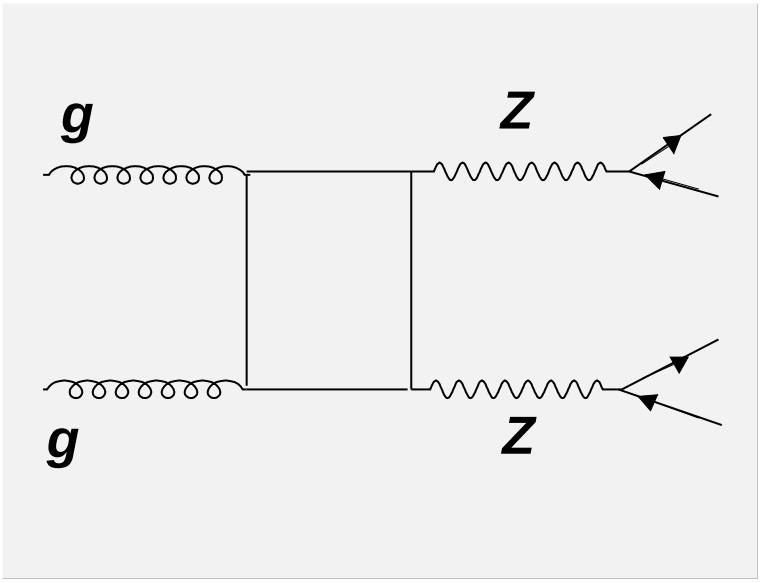

Figure 7.21: Feynman diagram of the irreducible gg background. Two incoming gluons emit two Z^0 through a box process.

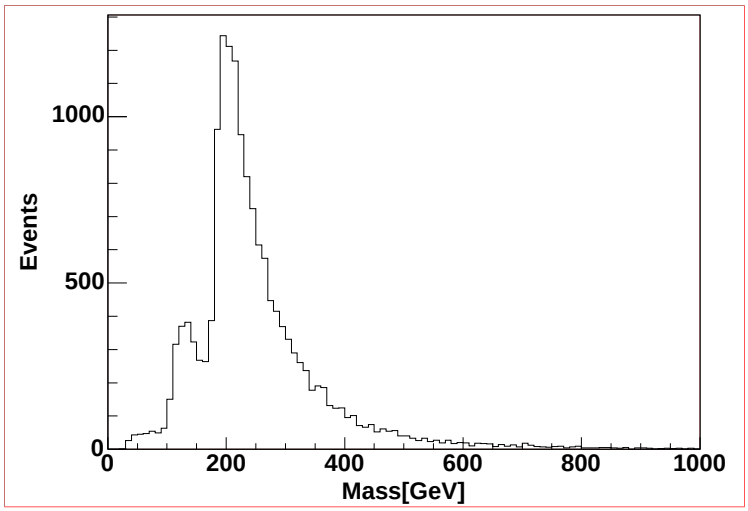

Figure 7.22: The invariant mass of four leptons originating from two background Z bosons. Note the characteristic peak at around 110 GeV. In this histogram, the invariant mass from all decay channels are included.

see in figure 7.22 a characteristic top at around 110 GeV. This is because PYTHIA includes the full interference between the γ^* and the Z^0 in the matrix elements. Therefore the progagators peak both around m_Z and when the mass $\rightarrow 0$. The latter divergence is solved by a lower cutoff (in CKIN(41) and CKIN(43)) at 12 GeV. Therefore there are three mass thresholds: one at 2*12 = 24 GeV, one at $12 + m_Z = 100$ and one at $2 * m_Z = 180$. In figure 7.23 the same process is shown, but now the interference between virtual gamma and the Z boson is turned off using MSTP(43) equal to 2.

From figure 7.22 it is also seen that the peak occurs at a value greater than the invariant mass of two Z bosons. In the matrix element for $q\overline{q} \rightarrow ZZ$ there is a pole for $E = 2\,m_Z$ since when the integration over the phase space is carried out the result is proportional to $p/E = \sqrt{1 - 4m_Z^2/E_{cm}^2}$ which clearly vanishes for $E_{cm} = 2m_Z$. However, this is to first order in perturbation theory, only. At this resonance energy, higher order corrections have to be taken into account and parton density functions, as well. To discuss this is beyond the scope of this text, but an examination of higher order terms will show that the peak occurs at values above $2m_Z$.

In order to find a suitable function to fit the background, several candidates were tried. When both the cut on transverse momentum of lepton and the cut on transverse momentum of the Z boson were applied, a polynomial was first tried since a polynom is very flexible and can fit several shapes if the degree is high enough.
However, it turned out that a Landau distribution was the best candidate for fitting the background when two cuts were applied.

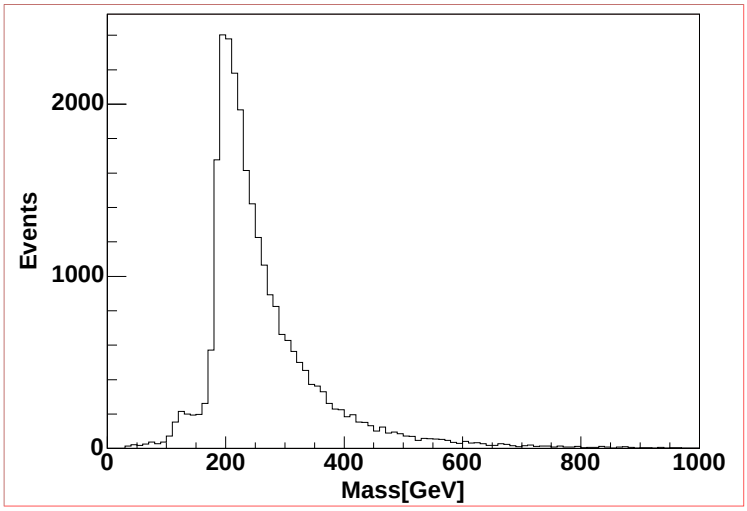

Figure 7.23: The invariant mass of four leptons originating from two background Z bosons. Interference effects are not included and the characteristic peak around 110 GeV is absent.

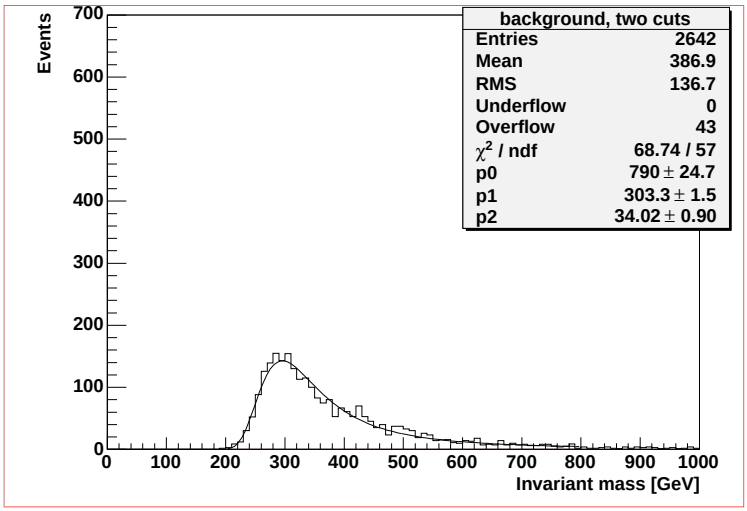

Figure 7.24: The background fitted with a Landau distribution

The Landau distribution

The Landau distribution is a probability density function that most often is used in describing the energy loss when a charged particle traverses a layer of matter of a given thickness, [12]. It is given by

$$f(\Delta;\beta) = \frac{1}{\xi}\phi(\lambda) \tag{7.16}$$

The function $\phi(x)$ is given by

$$\phi(x) = \frac{1}{\pi}\int \exp\left(-u\,log\,u - \lambda u\right) sin\pi u\,du \tag{7.17}$$

The LANDAU function in ROOT is given with mpv(most probable value) and sigma. The Landau function has been adapted from the CERNLIB routine G110 denlan.

7.5 Correct absolute and relative scaling

In this section we will use the cross sections and luminosity to derive the correct number of signal events and background events for one year of running with LHC at high and low luminosity. The expressions 'high' and 'low' luminosity will be clarified shortly.

We define the integrated luminosity as

$$L = \int \mathcal{L}dt \tag{7.18}$$

where $\mathcal{L}$ is the instantaneous luminosity.
If two bunches of protons containing n_1 and n_2 particles collide with frequency f, the instantaneous luminosity is approximately given as

$$\mathcal{L} = f * \frac{n_1 * n_2}{4\pi\sigma_x\sigma_y} \tag{7.19}$$

where σ_x and σ_y characterize the Gaussian transverse beam profiles in the horizontal and vertical directions.
Instantanous luminosity is often expressed in units of $cm^{-2}s^{-1}$ and tends to be a large number. It is a measure of how many particles that occupies a certain area at a given time.
The initial particle distribution at the source is often far from Gaussian, but, by the time the beam reaches high energy, a normal distribution is a good approximation, thanks to the central limit theorem of probability and diminished importance of space charge effects.

The design luminosity for LHC is $\mathcal{L}_{high} = 10^{34}cm^{-2}s^{-1}$. Two phases are foreseen for the LHC. During startup and the first months of running, LHC will be running at low luminosity $\mathcal{L}_{low} = 10^{33}cm^{-2}s^{-1}$. This reduces the huge pile up and is therefore attractive.

One year of high luminosity operation at LHC is equivalent to $\approx 100(fb)^{-1}$ of integrated luminosity which is seen by multiplying the instantanious luminosity by the number of seconds in a year and use the fact that $1b = 10^{-28}m^2$.
In order to calculate the expected number of Higgs decays through a certain channel a year, we need the cross-section and branching ratio for Higgs decaying according to this channel. PYTHIA is here used to get the cross section times branching ratio.
For a higgs-mass of 190 GeV the cross-section times branching ratio is 9.138 fb which gives 914 Higgs-events a year at high luminosity since $N = \sigma \times L$. For a higgs-mass of 230 GeV the cross-section times branching ratio is 9.457 fb. This translates into 946 Higgs-events a year at high luminosity.
The cross section for the background process $q\overline{q} \to ZZ \to 4l$ is 70.33 fb. And as previously mentioned, the only way to generate background events using PYTHIA is through this process. To also include the contribution from gluon fusion we multiplie the cross section by a factor 1.3. This gives a total cross-section of 91.429 fb and correspondingly ~ 9000 events.

7.6 Cuts

In order to minimize the irreducible background, a cut on the p_T-distribution of the four leptons is imposed. The two leading leptons are required to have transverse momenta [5] above 20 GeV, whereas the other two are required to have transverse momenta above 7 GeV. In the following these cuts will be called standard cuts.

In figure 7.25, 7.26 and 7.27 is shown the distribution of the transverse momentum for all four leptons both for Higgs-bosons with mass $m_H = 200$ GeV, $m_H = 320$ GeV and $m_H = 500$ GeV. The p_T plots include final states with four electrons, four muons and the di-electron/di-muon final state.
Now, these plots suggest that in order to reduce the number of background events, we impose a cut on the p_T as done in the TDR. And, indeed, when we apply the loose selection cuts on the background, the number of events is reduced with approximately 6.2%. When the same cuts are applied on the signal, the number of events is reduced by less than 1%. For any cut, the relative amount of lost background events should be more than for the signal.

Now, 7.25, 7.26 and 7.27 clearly show that when the four signal leptons come from a heavy Higgs boson, the distribution of transverse momentum is shifted towards larger values of p_T. This is not surprising since a heavy object has more energy and momentum to give to its decay products.
This suggests that the cut in the TDR on 20 GeV for the two leading leptons and 7 GeV for the other two is too loose. And, as can be seen in 7.29, when the Higgs mass increases, the minimum value of p_T of the hardest of the leptons, also increases.

[5] Transverse momentum: $p_T = \sqrt{p_x^2 + p_y^2}$

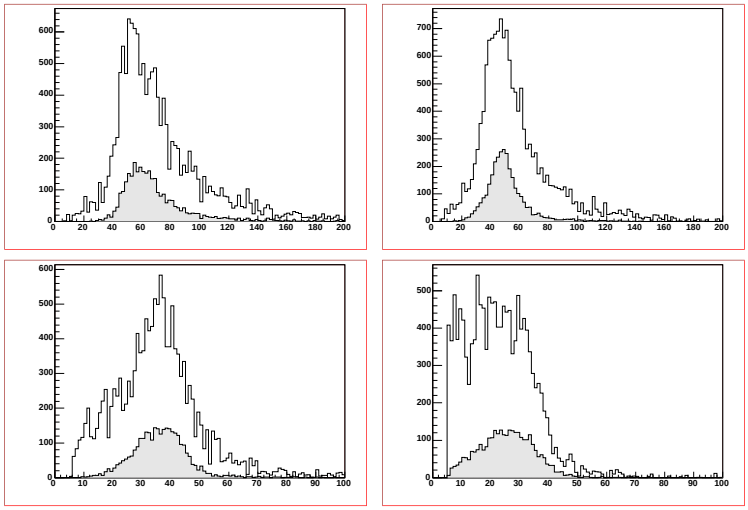

Figure 7.25: The p_T distribution of four leptons. The distributions of both background and signal are drawn. The shaded distribution corresponds to the signal which is the decay of a Higgs with mass 200 GeV. The units on the axis are 'number of events' on the y-axis and 'transverse momentum in GeV' on the x-axis.

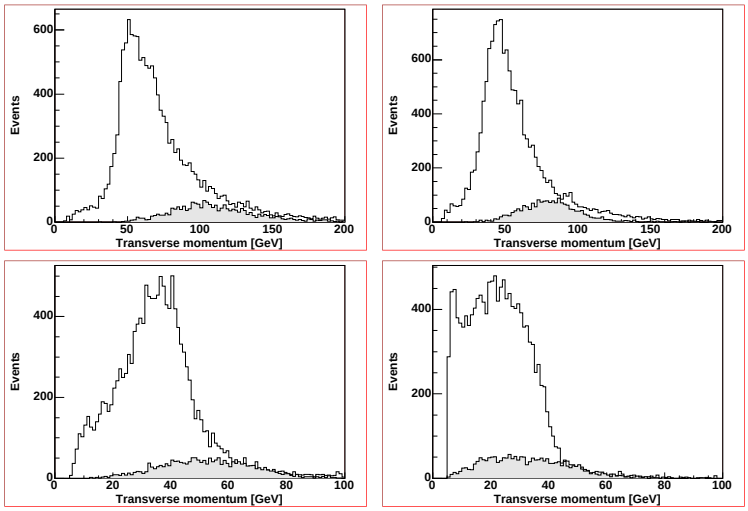

Figure 7.26: The p_T distribution of four leptons. The distributions of both background and signal are drawn. The signal leptons originates from a Higgs with mass 320 GeV. The signal corresponds to the shaded area. We see that the transverse momentum for the signal now is shiftet towards higher values of p_T.

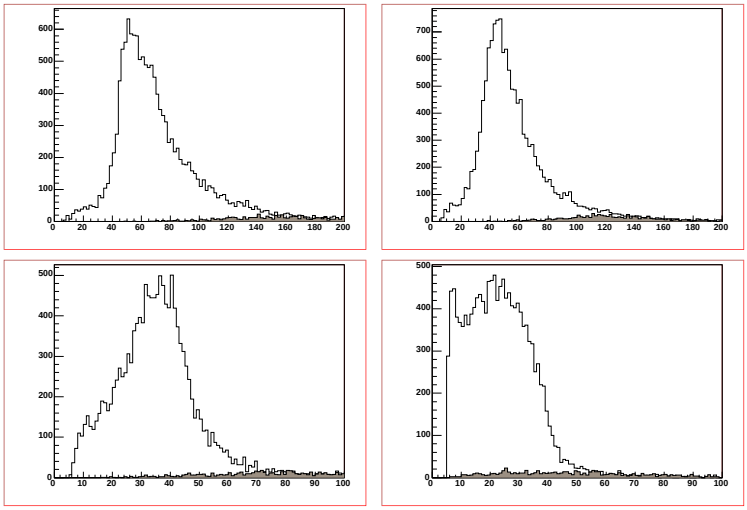

Figure 7.27: The p_T distribution of four leptons. The distributions of both background and signal are drawn. The signal leptons originate from a Higgs with mass 500 GeV. The signal corresponds to the shaded area. We see that the transverse momentum for the signal now is shiftet towards higher values of p_T. The reduced number of signal events due to decreasing cross section of Higgs production is clearly visible. The units on the axis are as in figure 7.26.

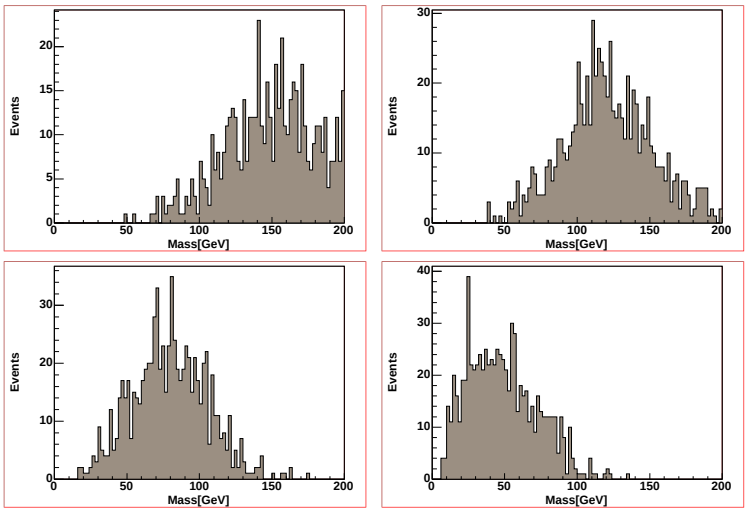

Figure 7.28: The p_T distribution of four leptons from a Higgs boson of mass 500 GeV. Only the signal is plotted and compared to figure 7.27 it is now easier to see the p_T distribution.

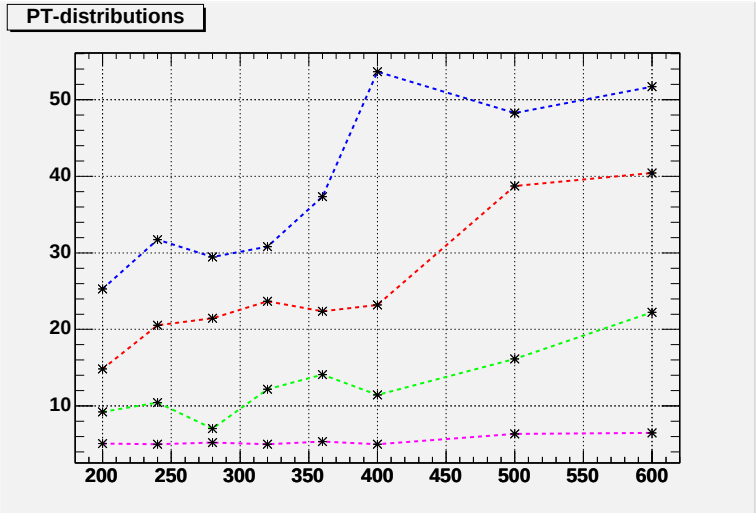

Figure 7.29: The lepton with smallest value of p_T as a function of Higgs mass. Only signal leptons shown. The blue line corresponds to the leading lepton, the read line corresponds to the next to leading lepton, the green line corresponds to the next to smallest value of p_T and the last line shows the lepton with smallest value of p_T. The units on the axes are 'Higgs mass in GeV' on the x-axis and 'p_T in GeV' on the y-axis.

To systematize the new cuts that are imposed on the transverse momentum, we summarize them in table 7.13. The table shows the minimum values of the transverse momenta for the four leptons for increasing Higgs mass. We now apply the standard

Higgs mass	New cut on p_T [GeV]	Cut 'name'
200	7, 7, 20, 20	Standard cut
240	7, 7, 20, 30	Cut 1
280	7, 7, 20, 30	Cut 1
320	7, 10, 20, 30	Cut 2
360	7, 10, 22, 35	Cut 3
400	7, 10, 22, 45	Cut 4
500	7, 15, 35, 45	Cut 5
600	7, 20, 40, 50	Cut 6

Table 7.13: Shown here is a table with the new cuts on the transverse momentum (GeV) and in increasing order. The cuts are named 'standard cut', 'cut 1', etc.

cut and the new cuts on the signal leptons for different masses and the background. Table 7.14 shows the ratio of leptons which is kept of the signal when we impose the standard cuts proposed by the TDR. Also included is the fraction kept when the new cuts are applied.
We see that that the effect on the number of signal events when the new cuts are applied is none. For any cut, the relative amount of lost background events should be more than for the signal. Since the introduction of new cuts, as seen in table 7.14, does not affect

the number of signal events compared to the standard cuts, this is a good idea if the amount of lost background is bigger in each case.

Higgs mass	Standard cuts (%)	New cuts (%)
200	98.74	98.74
240	98.49	98.49
280	99.17	99.17
320	99.36	99.36
360	99.47	99.47
400	99.42	99.42
500	99.74	99.74
600	99.51	99.51

Table 7.14: The table shows the fraction of leptons kept when we impose the Standard cuts and the New cuts on the signal. The numbers are in per cent.

When the standard cut and the new cuts are imposed on the background, it becomes clear that the number of background events is reduced by a much larger fraction than the number of signal events. This indicates that it might be a good idea to impose the new cuts. In table 7.15 is shown the fraction of background events kept when the standard cut and the new cuts are applied.

Kind of cut	Events kept in (%)
No cut	100
Standard cut	93.58
Cut 1	93.03
Cut 2	92.52
Cut 3	91.44
Cut 4	85.55
Cut 5	79.60
Cut 6	65.68

Table 7.15: The fraction of events kept when we impose the standard cuts and the new cuts on the background.

In figures 7.31, 7.32 and 7.33 are shown the signal above the background for some Higgsmasses. We see that it can be diffictult to identify the signal in some cases.
When the Higgs mass is around 200 GeV, the signal is on the top of the background and careful Monte Carlo simulations of the background is needed.
For a Higgs with mass 320 GeV, the signal is very easy to identify above the continuous background.
Since the cross section for Higgs production falls with increasing Higgs mass, the number of simulated events is reduced for increasing Higgs mass and the peak is more difficult to identify above the background as is the case in figure 7.33. Here a 600 GeV Higgs is plotted and is almost invisible above the background.

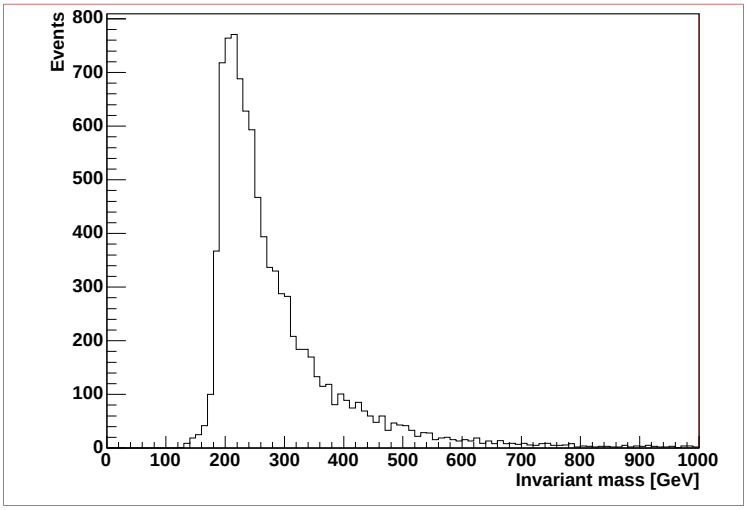

Figure 7.30: The distribution of invariant mass of four leptons from background events when the new cuts on transverse momentum have been applied.

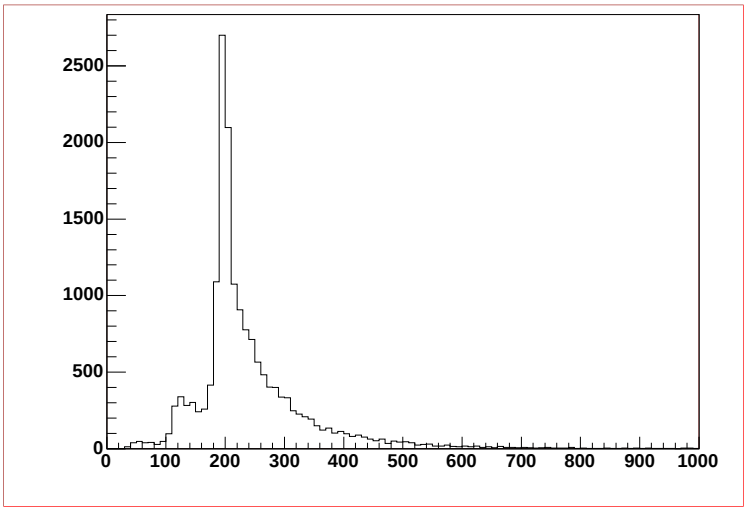

Figure 7.31: The signal plus background plotted for a Higgs boson with mass 200 GeV in the same hisogram. No cuts have been applied. The horisontal axis is 'invariant mass in GeV' and the y-axis is 'Number of events'. Since the Higgs mass corresponds to the peak in the background distribution, it is not easy to identify the signal above the background.

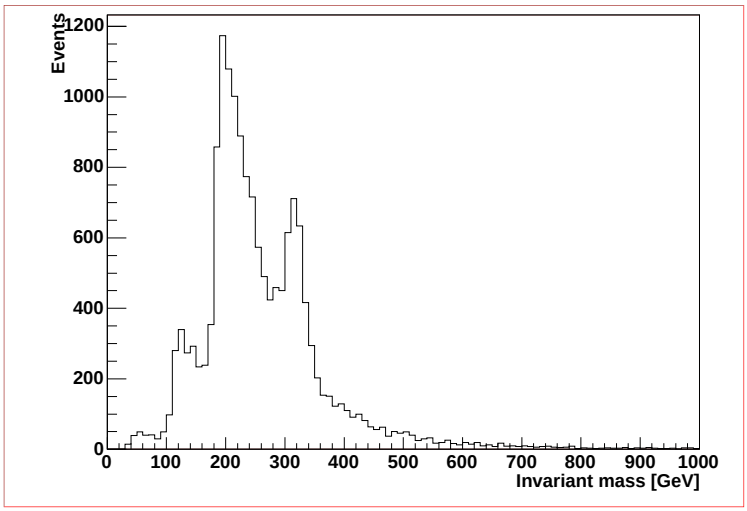

Figure 7.32: The signal plus background plotted for a Higgs boson with mass 320 GeV. No cuts have been applied.

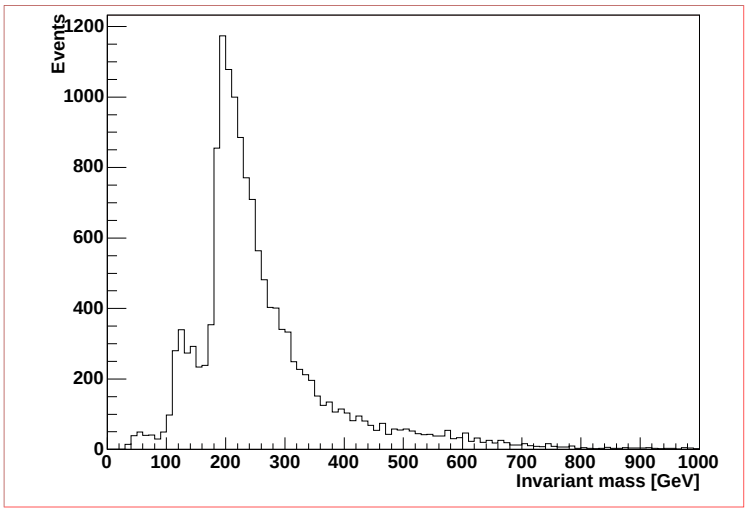

Figure 7.33: The signal plus background plotted for a Higgs boson with mass 600 GeV. No cuts have been applied. The signal is now almost invisible over the background. But compared with 7.32 it is possible to see 'something' above the background.

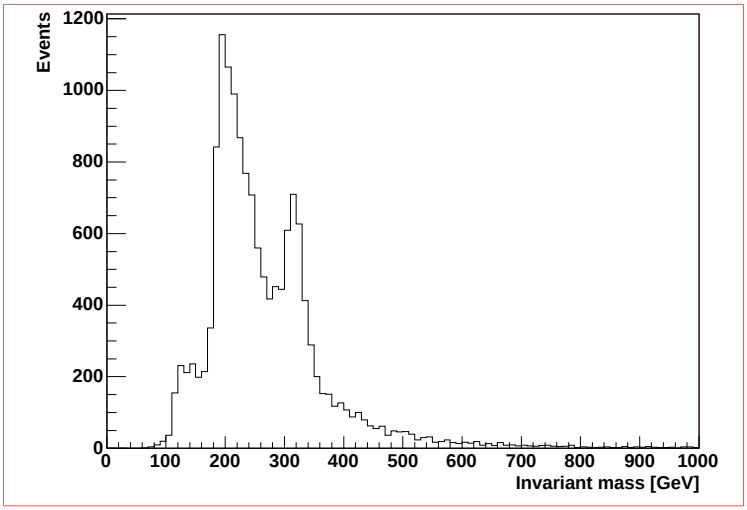

Figure 7.34: The signal and background plotted in the same histogram. The Higgs mass is 320 GeV. The standard cuts have been applied.

We now apply the standard cuts and the new cuts and see how these cuts affect the signal and background. We plot the signal and background in the same histogram again. In figures 7.34 and 7.35 the distribution for invariant mass for signal from a Higgs with mass 320 GeV and background is shown when the standard cuts and the new cuts are applied. From these figures, it is not easy to see wether the new cuts on the p_T-distribution of the leptons in the final state had any impact or not. This will not be clear, however, before the significance is calculated.

In figures 7.36 and 7.37 the standard cut and the new cuts are applied on the signal and background for a Higgs boson with mass 600 GeV. We see that it is difficult to identify the peak above the background even when the 'new' cuts are applied. This suggests that an additional cut is called for.

Since the Z-bosons from Higgs decays are produced through the two-body decay of a heavy object, background can be rejected by requiring that the transverse momentum of the harder of the two Z-bosons, $p_T^{max(Z_1,Z_2)}$, to be larger than a certain treshold value. It is therefore very important that we reconstruct in each event the correct value of the transverse momentum of the two Z bosons. In order to do that, it is necessary to find the correct combination of the leptons in each event that reconstruct the Z-bosons.

In the events where the two Z bosons have decayed into leptons of different flavour, electrons and muons, there are no difficulties finding the correct combination of leptons that reconstruct the two Z bosons. The decay channels are

$$Z \to e^+ + e^-$$
$$Z \to \mu^+ + \mu^-$$

The invariant mass of each Z boson is reconstructed by picking the muon and antimuon

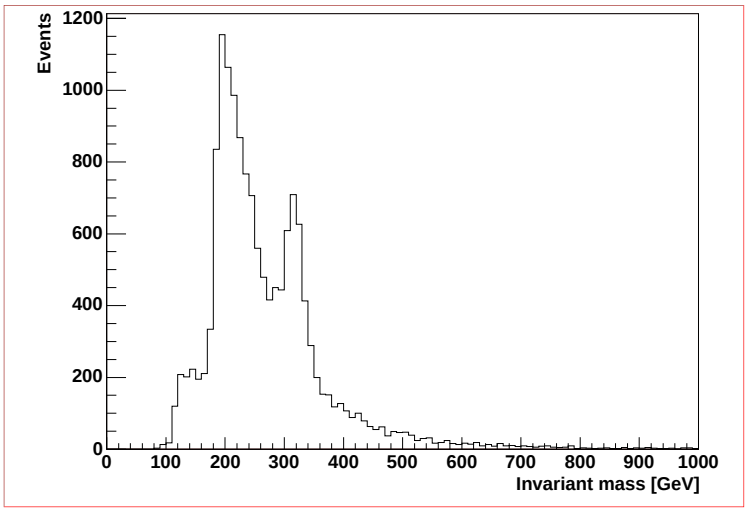

Figure 7.35: The signal plus background plotted in the same histogram. The Higgs mass is 320 GeV. The new cuts have been applied

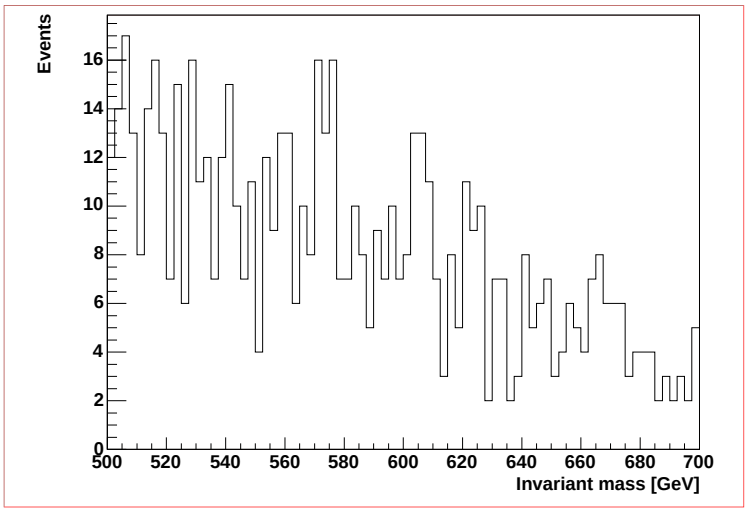

Figure 7.36: The signal plus background plotted in the same histogram. The Higgs mass is 600 GeV. The standard cuts have been applied and a cut on the invariant mass is applied to zoom in to the mass window of interest.

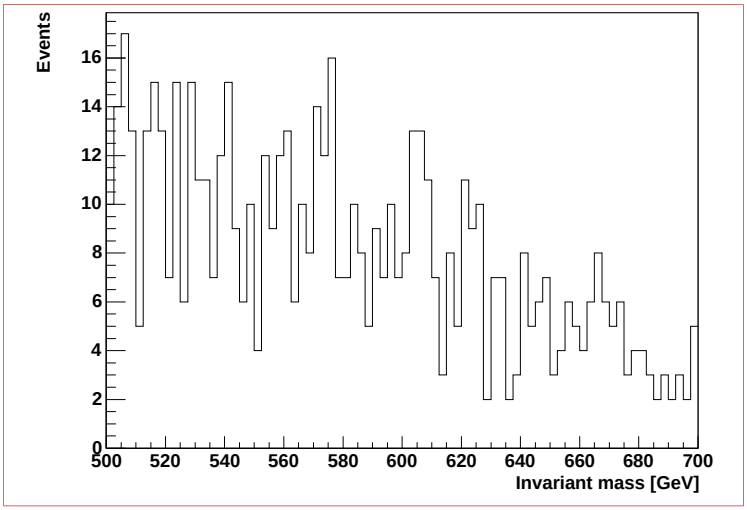

Figure 7.37: The signal plus background plotted in the same histogram. The Higgs mass is 600 GeV. The new cuts have been applied and a cut on the invariant mass is applied to zoom in to the mass window of interest. It is clear that there is almost no difference between this figure and figure 7.36. It is also clear that the signal is totally hidden by the background.

and the electron and positron and calculating the invariant masses in the two cases. In figure 7.38 we have reconstructed the invariant mass of the two Z bosons in the events where there are two electrons and two muons in the final state.

When both Z bosons decay into leptons of same flavour (that is, both Z decay for example into electrons) we face a problem of combinatorics. The reason is that there is not a unique way to combine the electrons and positrons to give two Z bosons. In each such event, given an electron, there are two positrons we can choose from in order to reconstruct the mass of the Z boson and also concerve charge and lepton number.

In figure 7.39 is plotted both correct and wrong combinations of the invariant mass of two leptons. We see a continuous, combinatorial background with a peak near the Z mass at approximately 91 GeV.

In order to reconstruct the invariant mass distribution of the Z bosons, it is necessary to pick the right electron and the right positron. To do this, we make use of the KFELE array. The arrays of energy and momentum are sorted by the absolute value of the total momentum. Therefore, a routine was written to identify the entries in the KFELE containing electrons and the entries containing muons. The same entries in the PXELE, PYELE and PZELE arrays correspond to the same particle. Then the invariant mass of the two combinations is calculated and the combination that minimizes a chi-square function is chosen.

The truth information from ATHENA version 7.0.3 has been changed in ATHENA version 8.0.5. Instead of knowing the energy, momenta and the mother of each lepton, ATHENA now provides the PDG ID, the transverse momentum, ϕ and η for every 'in-

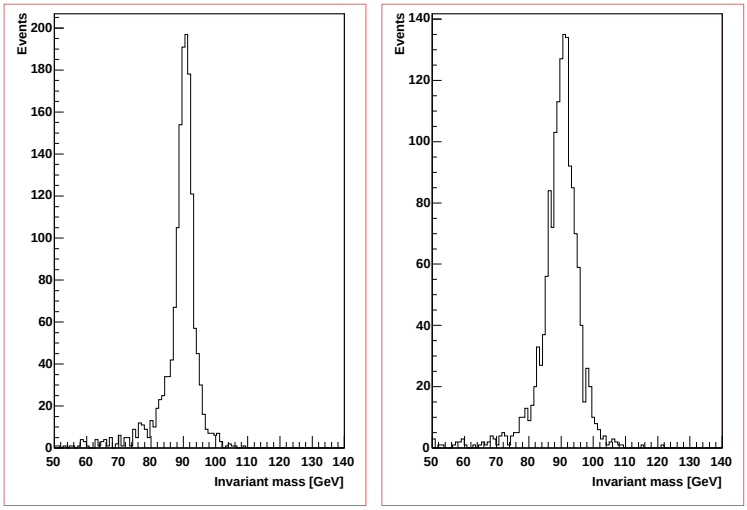

Figure 7.38: The invariant mass of the Z when one Z has decayed into electrons and one Z has decayed into muons. The figure to the left shows the reconstructed Z-mass from the electron/positron pair, while the figure to the right is the Z-mass from the muon/anti-muon pair.

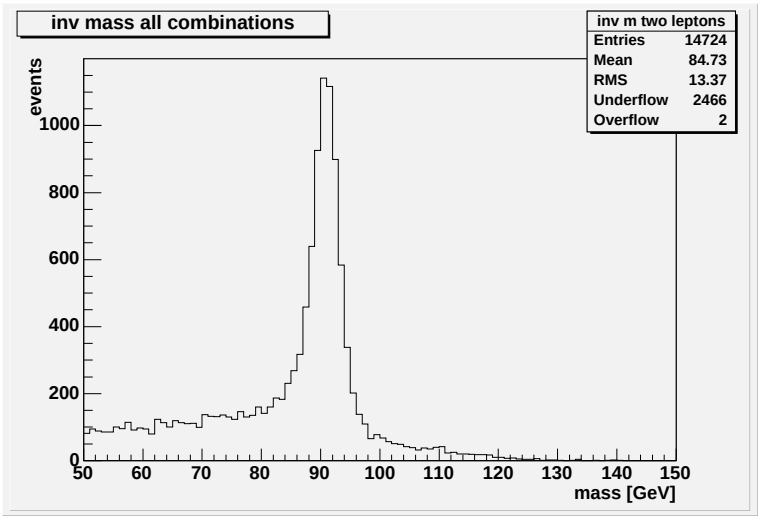

Figure 7.39: The invariant mass of two leptons. Both correct and wrong combinations are plotted in the same histogram.

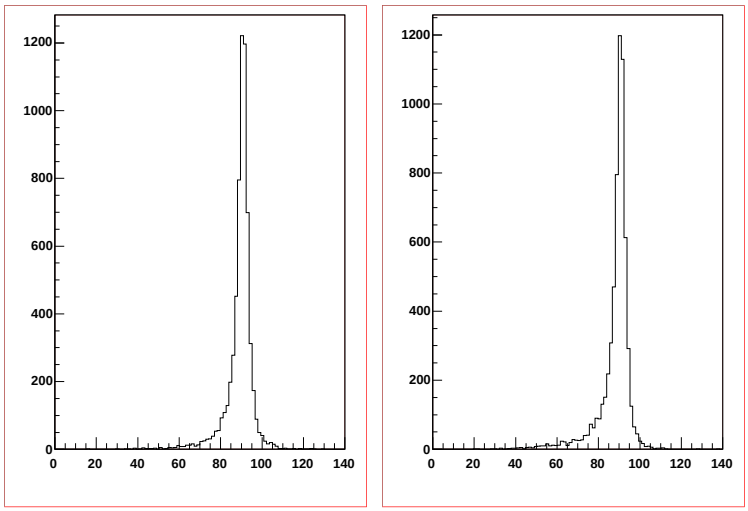

Figure 7.40: The invariant mass of the two Z bosons. The left Z boson has decayed into two muons while the Z boson in the right figure has decayed into two electrons.

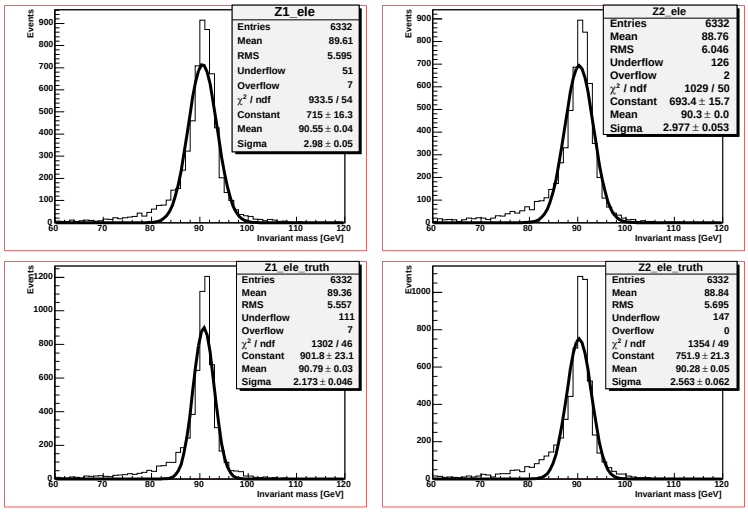

Figure 7.41: The invariant mass of both electron/positron pairs originating from one Z. In the plots below the correct combination is plotted and above, the combination that minimizes a χ^2 is plotted.

σ [GeV], reconstructed combinations	2.98	2.98
σ [GeV], true combinations	2.17	2.56

Table 7.16: The standard deviations in GeV of the fitted Gaussians to the reconstructed Z mass plot and the true Z mass plot.

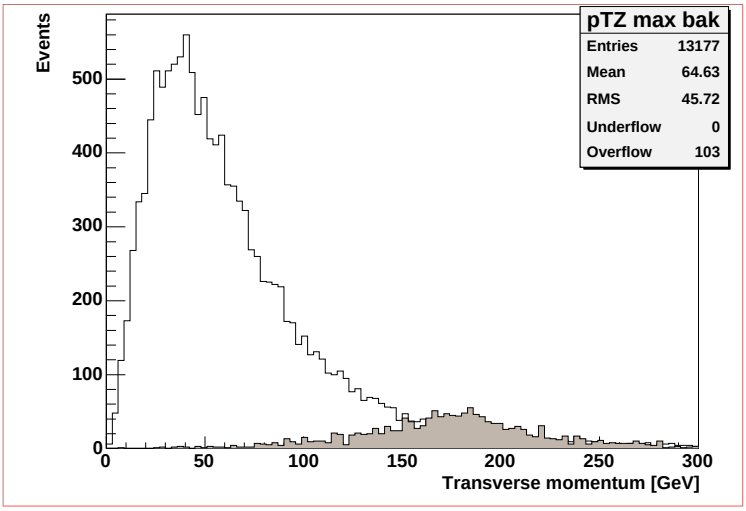

Figure 7.42: The distribution of the transverse momentum of the hardest of the Z bosons both for signal and background. The Higgs mass is 400 GeV and we clearly that the cut on the transverse momentum of the Z bosons is an efficient cut. The shaded area correspond to the p_T distribution of the signal.

teresting particle' such as leptons, photons and jets. From the provided information, the three components of the momentum for each particle are calculated as well as the energy.
When the mass plots are fitted with Gaussian distributions, the plots of correct pairs have a smaller standard deviation, see table 7.16.

In figure 7.42 the distribution of transverse momentum of the hardest of the Z-boson is plotted when the two Z bosons originate from a Higgs with mass 400 GeV. The standard cut on the p_T has been applied. It is clear from figure 7.42 that a significant amount of background is lost when we set a cut on the transverse momentum

The new cut on the transverse momentum of the leptons is strongly correlated with the cut on the transverse momentum of the Z boson. We see that the effect on the background by introducing the new cut in addition to the cut on the p_T of the Z is minimal. See figure 7.44. Because of this, we from now use the standard cut on the p_T of the leptons as well as the Z cut.

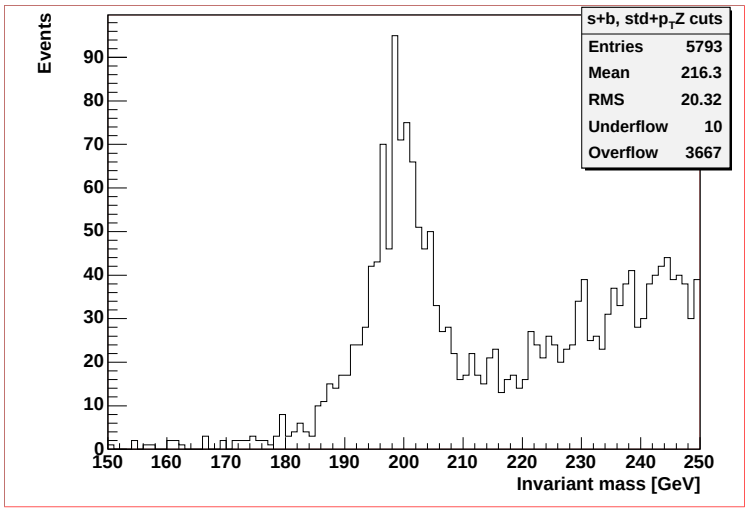

Figure 7.43: The signal plus background for a Higgs of mass 200 GeV. Both the cut on the transverse momenta of the leptons are applied as well as the cut on the p_T on the Z.

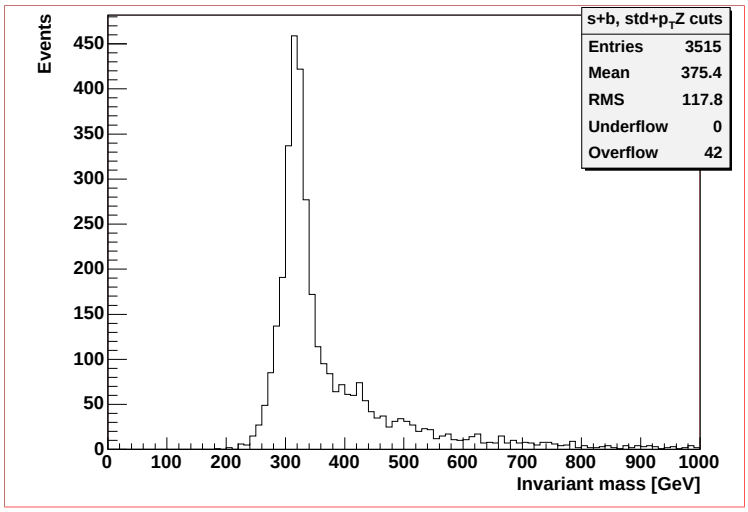

Figure 7.44: .The signal plus background plotted in the same histogram when the standard cut on the p_T of the leptons and the cut on the tranvserse momentum of the Z boson are used. Higgs mass = 320 GeV.

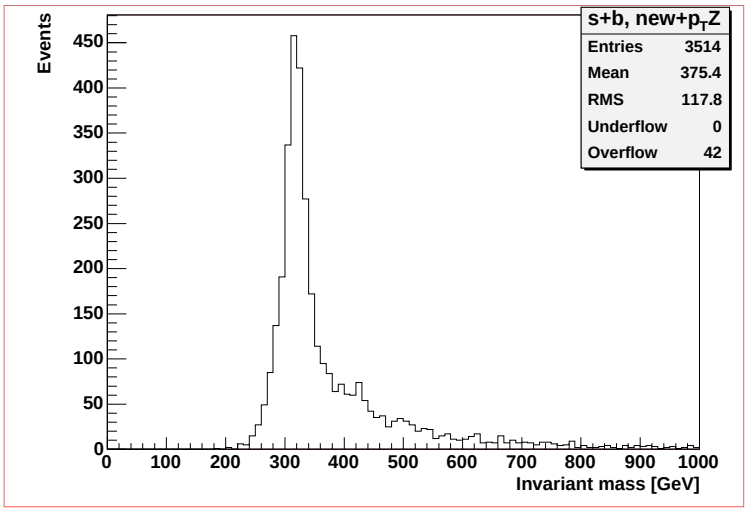

Figure 7.45: .The signal plus background plotted in the same histogram when the new cut on the p_T of the leptons and the cut on the tranvserse momentum of the Z boson are used. Compare with figure 7.44. The Higgs mass is 320 GeV.

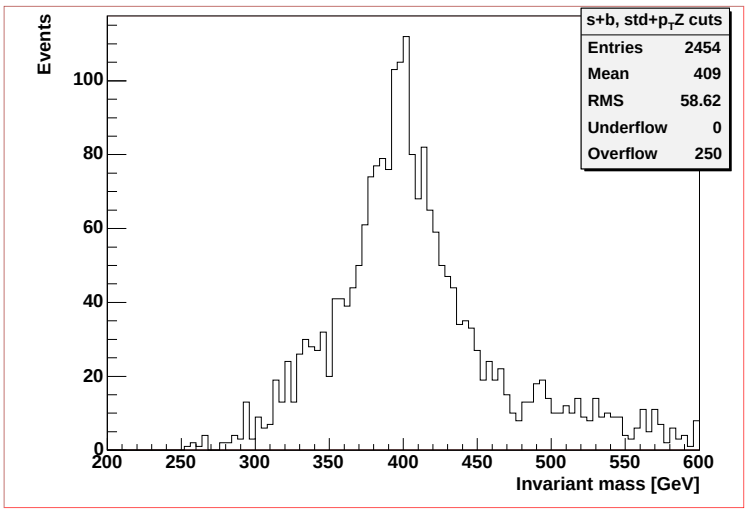

Figure 7.46: The signal plus background when mass of Higgs is 400 GeV. Compare with fig 7.51.

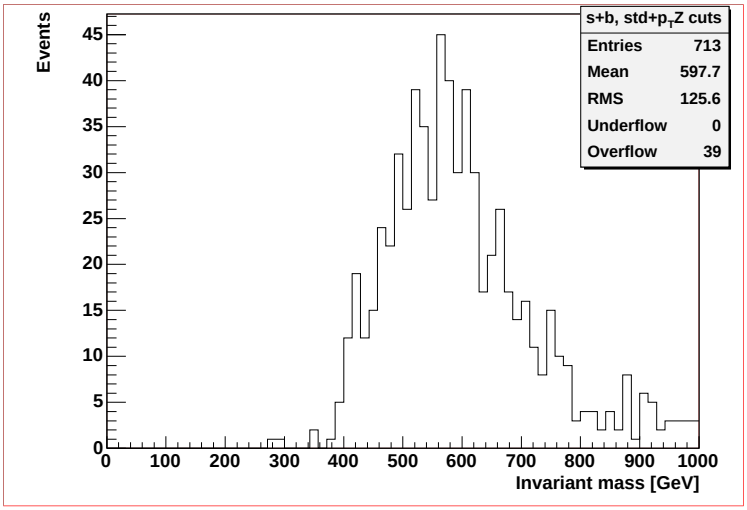

Figure 7.47: The signal plus background from a Higgs with mass 600 GeV. Cut on p_T Z is applied.

7.6.1 Further cuts

Cut on the angle between the letpons from the Z boson with highest p_T

In the centre of mass system of the Higgs boson, the two Z^0 bosons will be produced back to back and in the centre of mass system of a Z^0 boson the two leptons will also be produced back to back. This means that the angle between the leptons in this frame is 180 degrees.
The Z bosons are boosted and we use the Lorentz transformations to determine the relationship between an angle in the rest frame of a Z^0 and the laboratory system.

$$cos\theta = \frac{cos\theta' + \frac{v}{c}}{1 + \frac{v}{c} cos\theta'} \tag{7.20}$$

where θ' is the angle between the leptons in the rest frame of the Z^0-boson and the θ is the same angle in the laborary system. From 7.20 it can be seen than a greater boost gives a smaller angle in the lab frame since the value of $cos\,\theta$ increases when v increases. An efficient cut is to require the angle between the leptons from the hardest Z boson to be smaller than 90 degrees, as is seen from figure 7.48. This cut is appropriate only for intermediate Higgs masses. For $m_H = 200$ GeV, the cosine of the angle was chosen to be greater than -0.4.
For $m_H = 500$ GeV and $m_H = 600$ GeV, the cosine of the angle between the leptons was required to be greater than 0.5. See figure 7.49.

However, we might suspect a correlation. The two leptons are from a Z^0 with a large boost and hence a large p_T value. There might be a correlation between the cut on a large value of p_T of the Z^0 and the cut on the angles between the leptons from the same Z^0.

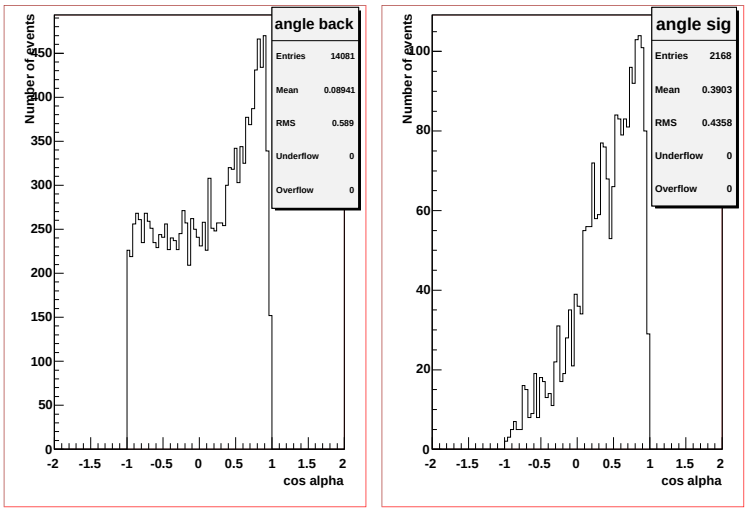

Figure 7.48: The distribution of angles between the leptons from the hardest of the Z bosons. The signal corresponds to a Higgs with mass 280 GeV. Both distributions for signal and background are shown. The background is shown in the left figure and the signal is plotted in the right figure. The value shown is the cosine to the angle.

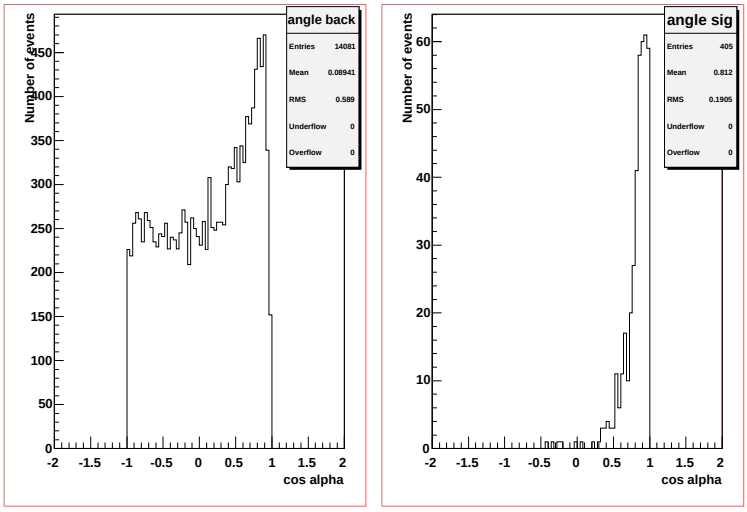

Figure 7.49: The same as figure 7.48, but now the mass of the Higgs boson is 600 GeV.

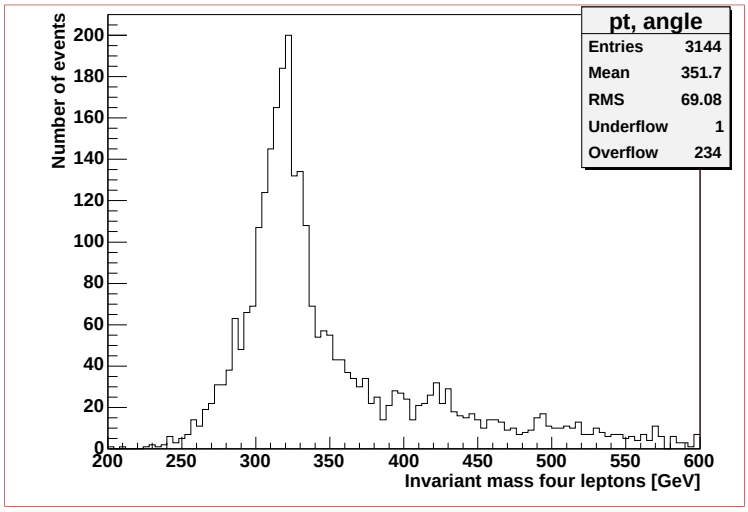

Figure 7.50: The invariant mass of four leptons when the cut on angle between leptons is applied. Compared with 7.44 the significance is expected to be somewhat higher.

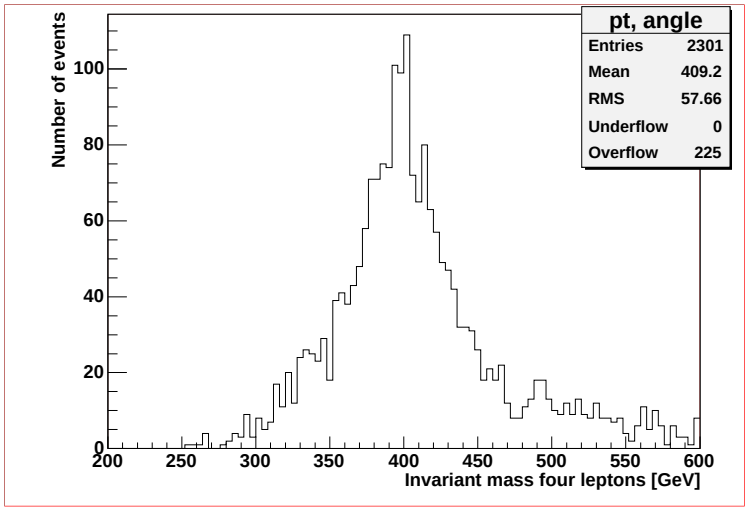

Figure 7.51: The invariant mass of signal and background for a Higgs with mass 400 GeV. The cut on angle between leptons is applied.

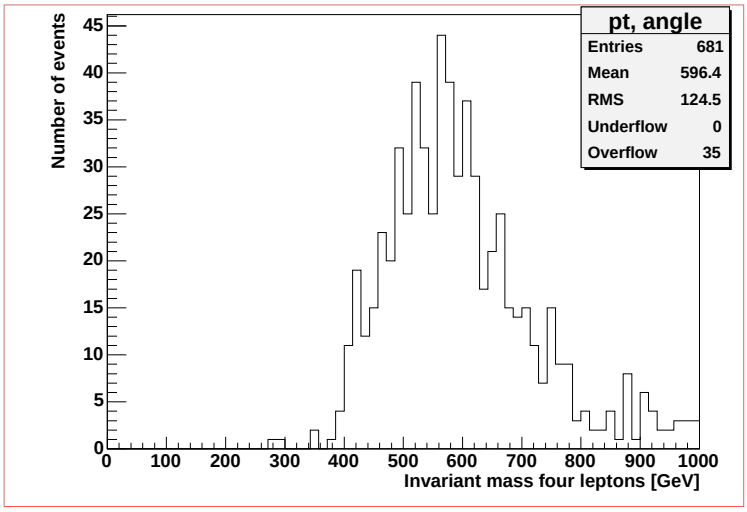

Figure 7.52: Invariant mass of signal plus background for a Higgs with mass 600 GeV. Cut on angle between leptons is applied.

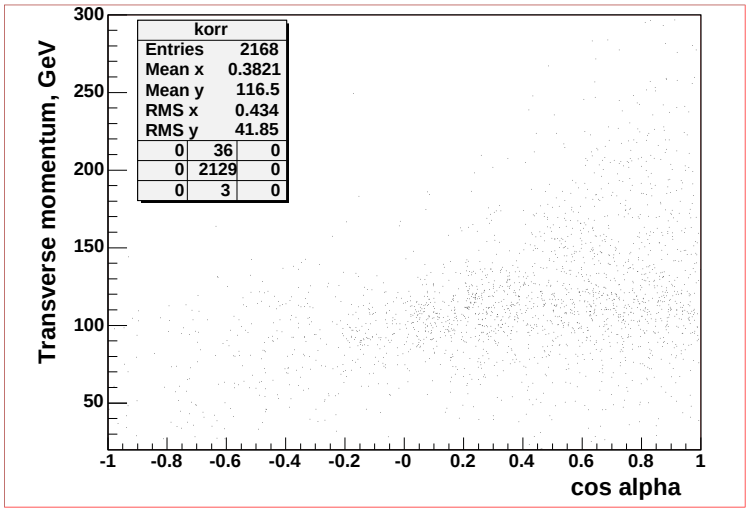

Figure 7.53: The correlation between the p_T of the hardest Z^0 boson and the angle between the leptons from the same boson, for a Higgs boson with mass 280 GeV.

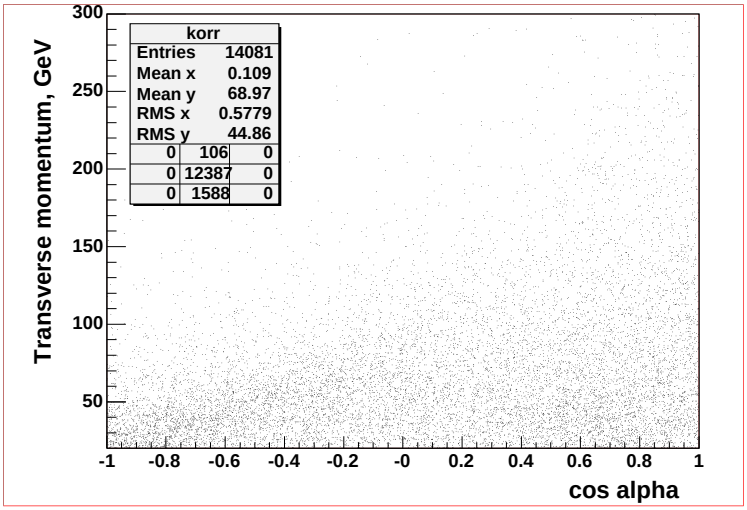

Figure 7.54: The correlation between the p_T of the hardest Z^0 boson and the angle between the leptons from the same boson from the background events. From the plot it is clear that the hardest Z^0 in the background events generally have a lower value of p_T and that the hardest Z^0 does not generally have a small angle between its decay products. However, when the value of p_T increases, the opening angle decreases in this case, too.

Cut on the angle between the planes defined by the decaying leptons

The two leptons from the same Z boson define a plane and from the momentum vectors of these two leptons, the normal vector to each plane is calculated.
To see wether a cut on the angle between these normal vector could be imposed, the distribution of this angle is plotted for the signal and background in figure 7.56. A correlation plot between the p_T of the hardest Z^0 and the angle is presented in figure 7.55. We see from this plot that there is not a very strong correlation between the p_T and the angle. However, figure 7.56 shows that there is no obvious value for the angle to place the cut. No matter where we place the cut, a large fraction of the signal disappears.

This becomes clear from figures 7.57 and 7.58 where the number of events becomes rather small, so the efficiency becomes low.
Therefore, when calculating the significance of the signal, this cut will not be included because of the great loss of efficiency.

7.6.2 Summary of cuts

In this section, the effects of all the cuts are summarized. We see how the different cuts affect the number of signal events and background events for different Higgs masses.

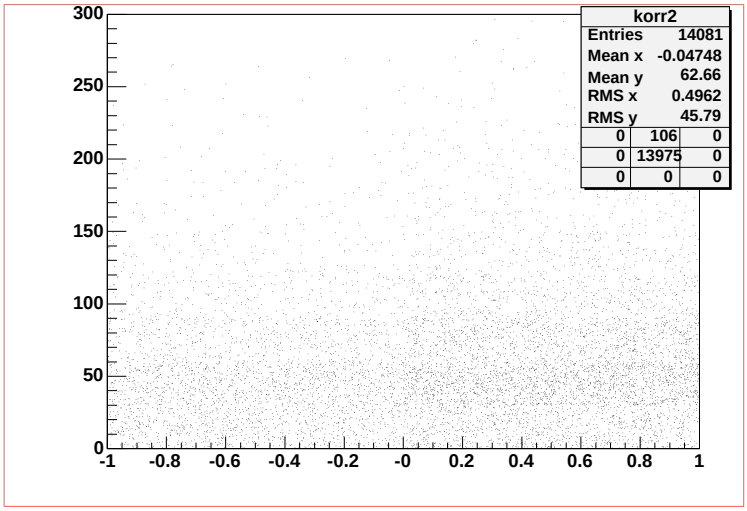

Figure 7.55: Correlation between the p_T of the hardest Z^0 boson and the angle between the normal vectors of the planes defined by the decaying leptons. We see no correlation between high p_T and the value of the cosine of the angle.

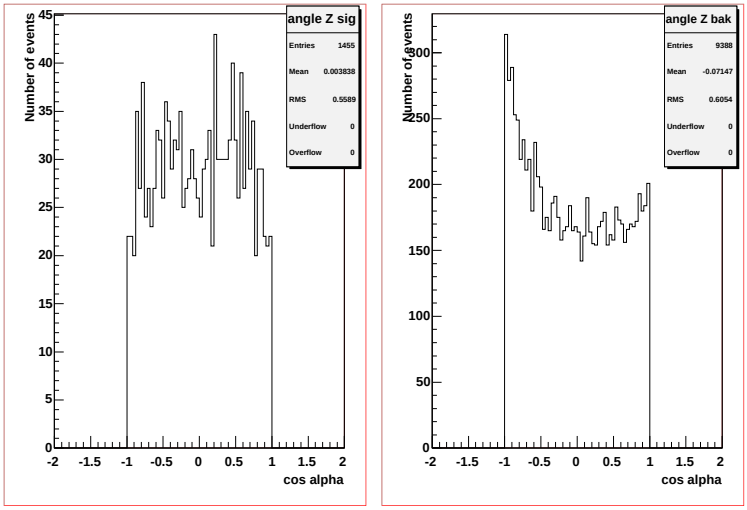

Figure 7.56: The distribution of angles between the normal vectors to the planes of the leptons when the two Z^0 bosons have decayed. The signal corresponds to a Higgs with mass 280 GeV. The signal is to the left while the background is in the right box.

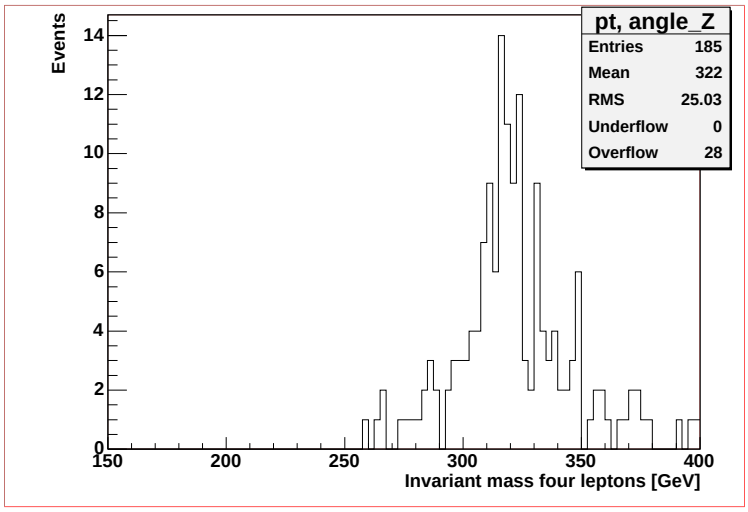

Figure 7.57: When the cut on the angle between the decaying planes is applied, the number of events left becomes rather small. $m_H = 320$ GeV.

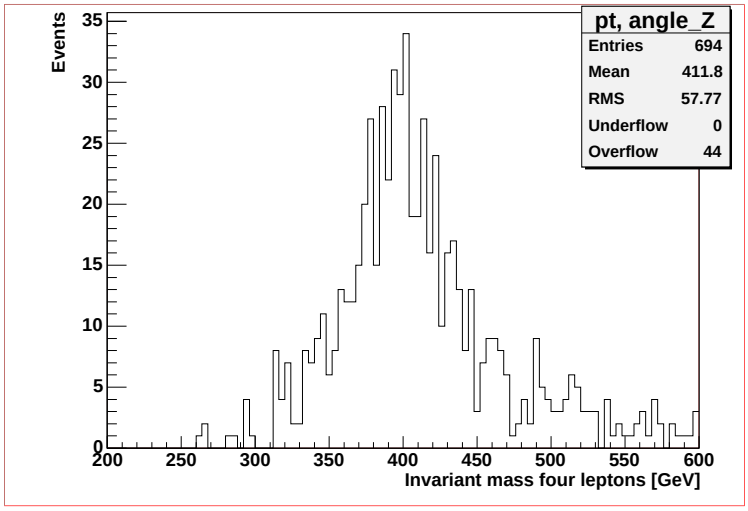

Figure 7.58: The signal plus background in the same histogram when the Higgs mass equals 400 GeV and all cuts are applied.

m_H	No cuts	NLEP=4	$p_T lep$	$p_T Z$	Angle lep	Angle Z
200	5600	3008	2970	949	683	52
240	4800	2621	2593	1512	1196	429
280	3930	2168	2150	1604	1440	494
320	3423	1877	1865	1504	1421	122
360	3360	1893	1883	1562	1501	507
400	2820	1554	1545	1288	1260	414
500	1400	770	768	650	646	211
600	733	405	403	328	326	113

Table 7.17: The number of signal events for different higgs masses left when successive cuts are applied.

m_H	No cuts	NLEP=4	$p_T lep$	$p_T Z$	Angle lep	Angle Z
200	45715	14081	13177	4844	3527	150
240	45715	14081	13177	3583	2821	750
280	45715	14081	13177	2642	2198	574
320	45715	14081	13177	2011	1723	63
360	45715	14081	13177	1517	1333	346
400	45715	14081	13177	1166	1041	280
500	45715	14081	13177	642	593	158
600	45715	14081	13177	385	355	89

Table 7.18: The number of background events for different higgs masses left when successive cuts are applied.

7.7 Calculating the significance

The significance of the signal is an important quantity. It tells wether there is a signal present in the histogram or not. It could be that what appears to be a signal is only statistical and random fluctuations of the background.
We therefore need a quantitive measure to determine when we can say that there is a signal. We typically say we have conclusive evidence for a signal if the number of entries in a peak is five times more than the estimated error in what is taken as background events.
The starting point of the significance calculation is a histogram which contains both signal and background in correct absolute and relative scaling. The histogram can be obtained from simulation when real data do not exist, or from data in a real experiment.

We will calculate the significance for three different situations. First, the significance is calculated when only the p_T cut on the leptons is used. Secondly, when the cut on the p_T of leptons and the cut on the p_T of the hardest Z^0 boson are applied. The significance will lastly be calculated when the additional cut on the angle between the leptons from the hardest of the Z boson is introduced. We will not include the cut introduced on the

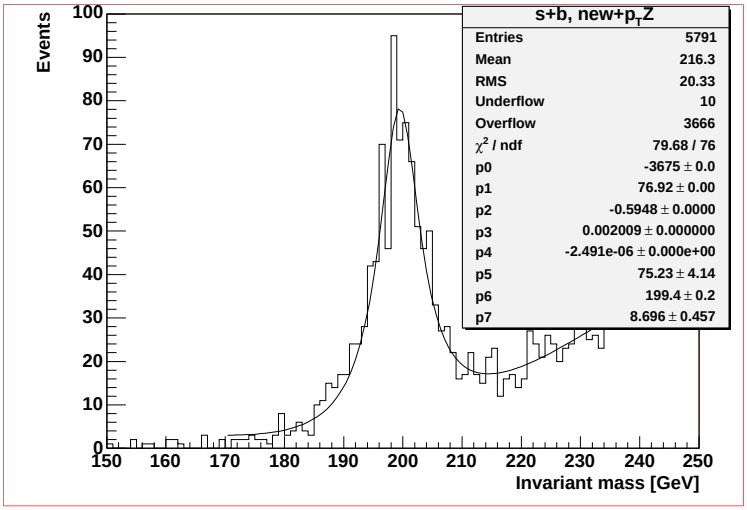

Figure 7.59: The signal from a Higgs with mass 200 GeV plus background when both p_T cuts are applied. The signal and background is fitted with a sum of a Breit-Wigner and a fourth degree polynomial. It is clear that the Breit-Wigner and a polynomial do not fit the shape of the signal and background too well.

angles between the planes of the leptons from the Z^0-decay.

7.7.1 The counting method

The easiest and most straightforward aproach of finding the significance of the signal is with the counting method. First, we fit the S+B histogram with a Gaussian, Breit-Wigner or a sum plus an exponential, polynomial or another function, where the Gaussian/Breit-Wigner is an approximation of the signal and the other function is an approximation of the background.

To find the number of signal and background events, we integrate the fitting function in the S+B histogram in a given mass interval. To get the corresponding number of events, the obtained number (which is the area under the function) is divided by the bin-width. The number of background events under the fitted background function is substracted in the same mass interval. The formula for calculating the significance is

$$S = \frac{N_{S+B} - N_B}{\sqrt{N_B}} \tag{7.21}$$

where S is the significance, N_{S+B} is the total number of events in the mass interval and N_B is the number of events under the fitted curve of the background.

The mass window is a symmetrical interval around the mean value of the fitted Gaussian:

$$\mu \pm \sigma\xi \tag{7.22}$$

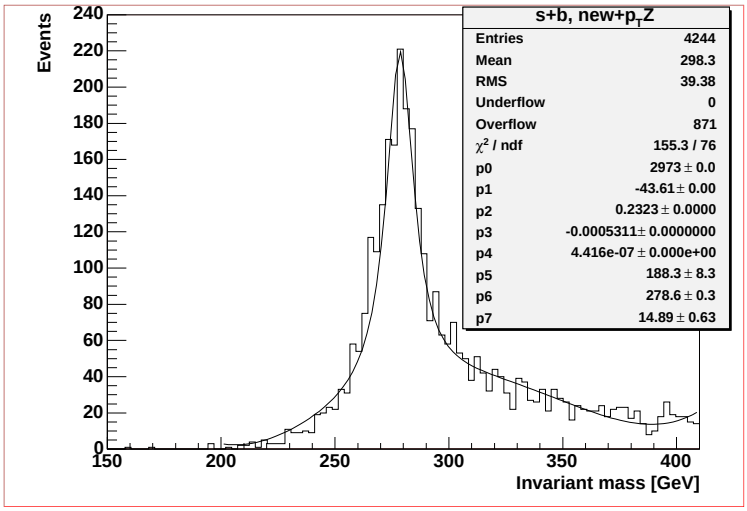

Figure 7.60: The signal from a Higgs with mass 280 GeV plus background when both p_T cuts are applied. The signal and background is fitted with a sum of a Breit-Wigner and a fourth degree polynomial. Also here it is clear that the shape of the contour is not too well described by the Breit-Wigner and the polynomial.

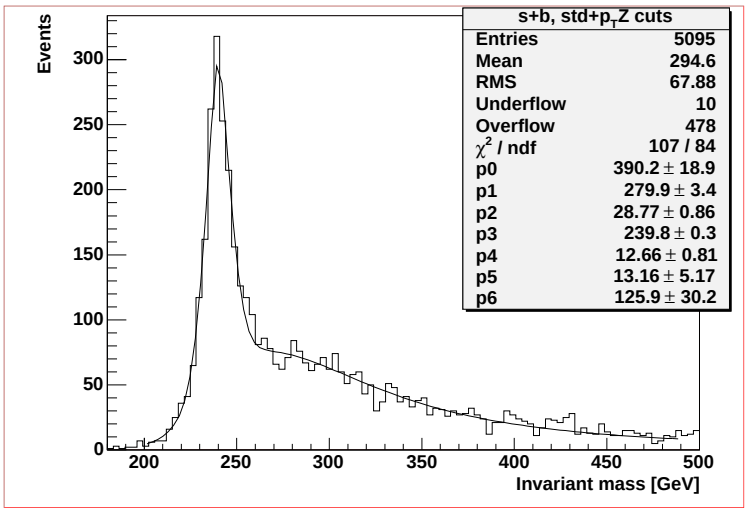

Figure 7.61: The signal plus background in the same histogram when the two p_T cuts have been applied. $m_H = 240$ GeV. The distribution has been fitted with a sum of a Gauss and a Breit-Wigner for the signal and a Landau distribution for the background.

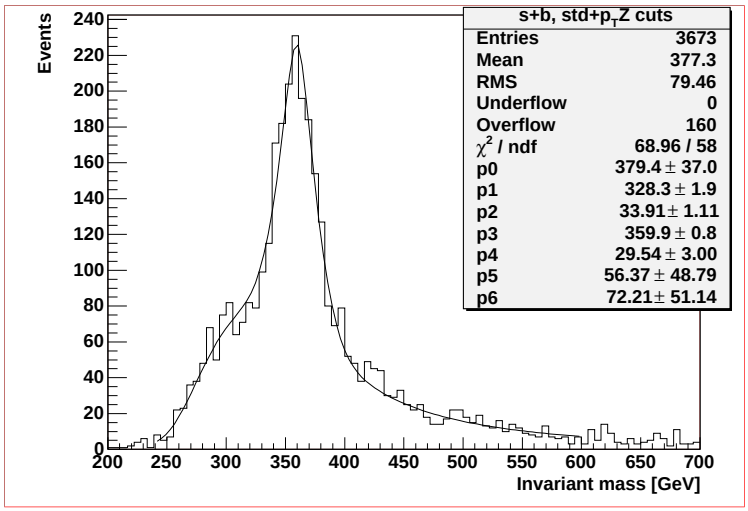

Figure 7.62: The signal plus background in the same histogram when the two p_T cuts have been applied. The distribution has been fitted with a sum of a Gauss and a Breit-Wigner for the signal and a Landau distribution for the background. m_H=320 GeV.

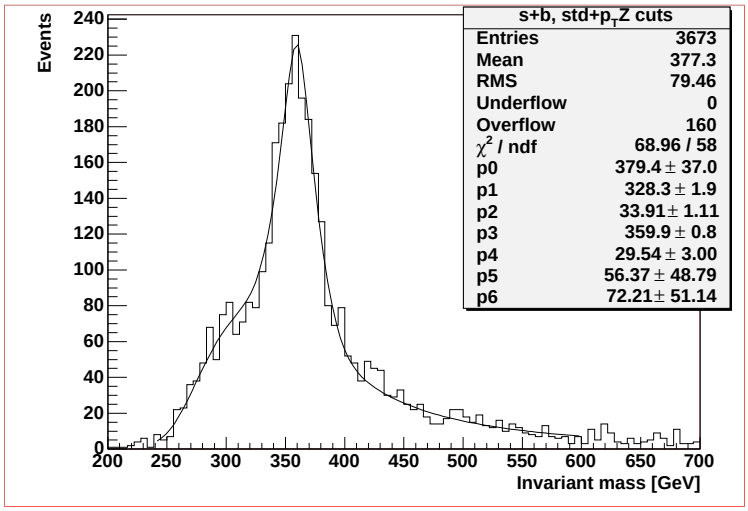

Figure 7.63: The signal plus background in the same histogram when the two p_T cuts have been applied. The distribution has been fitted with a sum of a Gauss and a Breit-Wigner for the signal and a Landau distribution for the background. m_H=360 GeV.

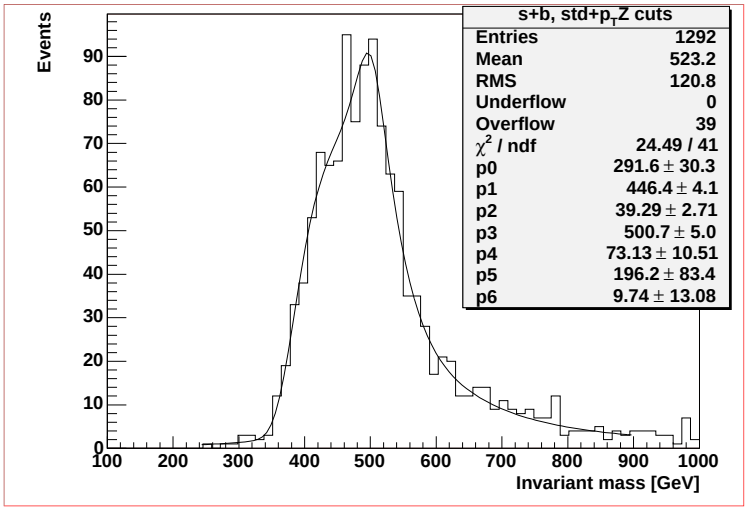

Figure 7.64: The signal plus background in the same histogram when the two p_T cuts have been applied. The distribution has been fitted with a sum of a Gauss and a Breit-Wigner for the signal and a Landau distribution for the background. m_H=500 GeV.

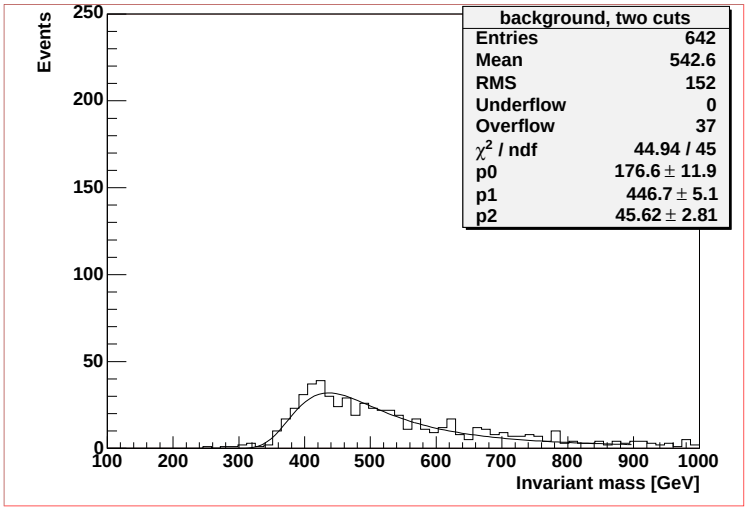

Figure 7.65: The background fitted with a Landau distribution. The cuts on the background are optimized for a Higgs with mass 500 GeV. Two cuts have been applied, the p_T cuts on leptons and the Z.

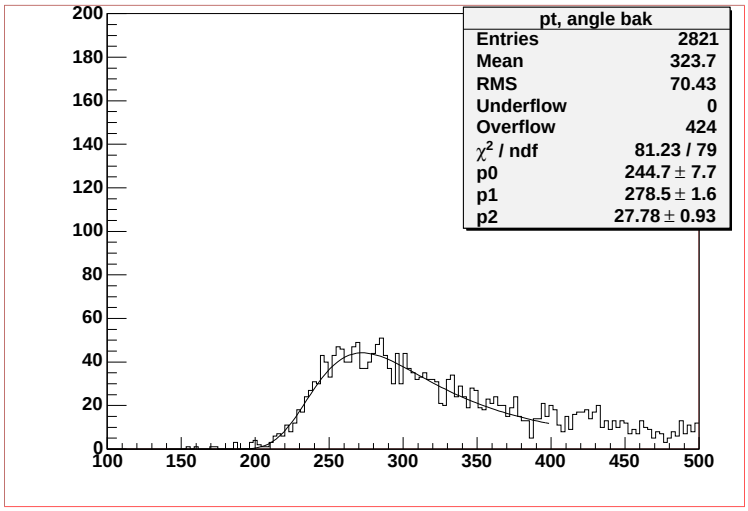

Figure 7.66: The background fitted with a Landau distribution. The cuts on the background are optimized for a Higgs with mass 240 GeV. Now three cuts have been applied, the p_T cuts on leptons and the Z, as well as the cut on the angle between the leptons from the hardest of the Z bosons. We see a god agreemnt between the histogram and the fitted curve.

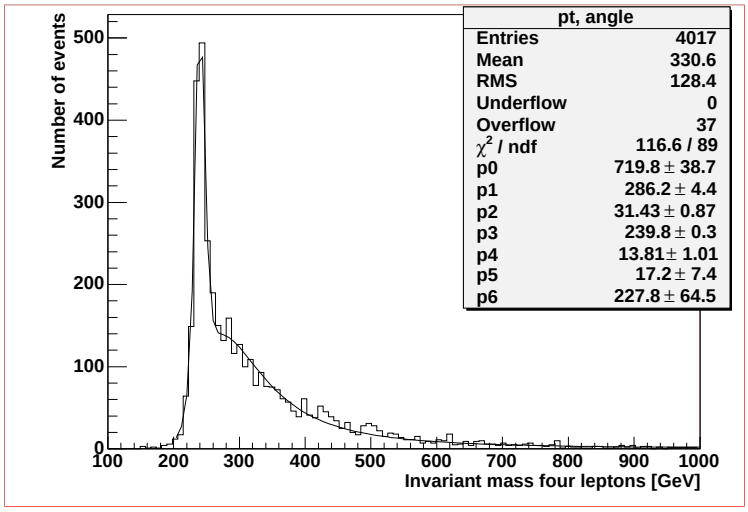

Figure 7.67: The signal plus background in the same histogram fitted with a sum of a Breit-Wigner, Gaussian and Landau distribution. The cuts on the background are optimized for a Higgs with mass 240 GeV. Three cuts have been applied, the p_T cuts on leptons and the Z, as well as the cut on the angle between the leptons from the hardest of the Z bosons.

where σ is the standard deviation of the fitting function. The only parameter that varies freely here, is the window parameter ξ. It is for every mass of the Higgs boson chosen in a way that maximises the significance.

The number of signal events, N_S can be treated as a Poisson variable with mean ν_S and the number of background events can be treated as a Poisson variable with mean ν_B. Suppose these means are without errors. The total number of events $N_{S+B} = N_S + N_B$ is therefore a Poisson variable with mean $\nu = \nu_S + \nu_B$. The probability to observe n events is thus

$$f(n; \nu_S, \nu_B) = \frac{(\nu_S + \nu_B)^n}{n!} \exp\left[-(\nu_S + \nu_B)\right] \tag{7.23}$$

Suppose now that an experiment has been carried out that finds n_{obs} events. In order to quantify our degree of confidence in the discovery of a new effect, i.e. $\nu_S \neq 0$, the probability to observe n_{obs} events or more from background alone is calculated. This is given by, [12]

$$P(n \geq n_{obs}) = 1 - \sum_{n=0}^{n_{obs}} \frac{\nu_b^n}{n!} e^{\nu_b} \tag{7.24}$$

Since the number of events is a Poisson distributed variable, the variance equals the mean, and hence the standard deviation (the error) is given by $\sqrt{\nu}$. Therefore, the error of the number of events in a given bin, equals the square root of the number of events in the bin.
This explains the formula for significance. If the number of 'extra' events exceeds five times the error in the expected background, we claim discovery for a new particle.

Goodness-of-fit

We begin with a histogram with the observed x value with N bins. Suppose the number of entries in bin i is n_i, and the number of expected entries due to the fitting function is ν_i. The most commonly used goodness-of-fit test is based on Pearsons χ^2 statistic

$$\chi^2 = \sum_{j=1}^{N} \frac{(n_i - \nu_i)^2}{\nu_i} \tag{7.25}$$

Since χ^2 is a function of random numbers (discrepancy between measured and expected number of events in a bin), it is itself a random variable. If the data $(n_1, .., n_N)$ are Poisson distributed with mean values $(\nu_1, .., \nu_N)$ and if the number of entries in each bin is not too small ($n_i \geq 5$) one can show that the test statistic 7.25 will follow a χ^2 distribution for N degrees of freedom.
Since the standard deviation of a Poisson variable with mean ν_i is equal to $\sqrt{\nu_i}$, the χ^2 statistic gives the sum of squares of the deviations between observed and expected values, measured in units of the corresponding standard deviations. Since the expectation value of the χ^2 distribution is equal to the number of degrees of freedom, the ratio χ^2/N should be approximately one.

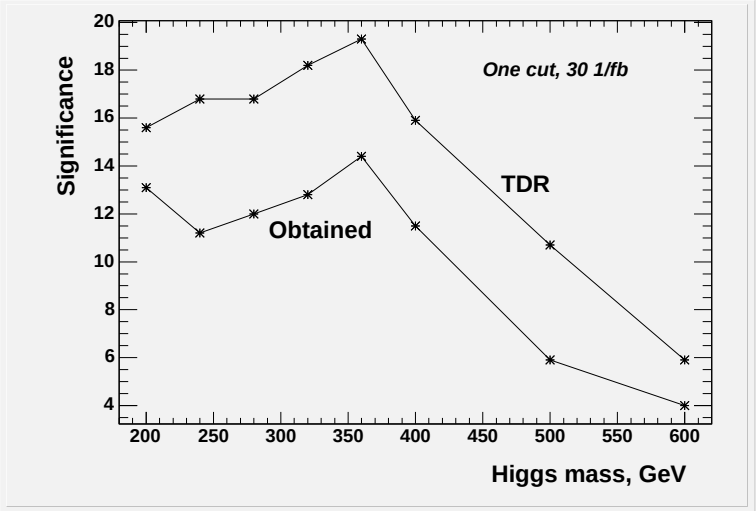

Figure 7.68: The significance obtained by the TDR for 30 fb^{-1} and the result from this thesis when only the p_T cut on the leptons are imposed. The result obtained here, denoted 'obtained', are somewhat lower due to changes in the cross sections.

7.7.2 Results and discussion

In this section, the results are given. The significances are presented for different masses and different cuts, see table 7.19. A comparison with [5] and [7] is also done.
In [7] the significances are presented when only the p_T cut on the leptons is applied, and for $30 fb^{-1}$ and for $100 fb^{-1}$ when the p_T cut on the Z^0 is applied as well. In [5], the significances are given for $100 fb^{-1}$ and only the p_T cut on the leptons.
The significances presented for an integrated luminosity of $100 fb^{-1}$ are obtained from a simple rescaling of the significances presented for $500 fb^{-1}$.

Higgs mass [GeV]	200	240	280	320	360	400	500	600
$S/\sqrt{B}$, one cut, $30 fb^{-1}$	13.1	11.2	12.0	12.8	14.4	11.5	5.9	4.0
$S/\sqrt{B}$, one cut, $100 fb^{-1}$	23.6	18.3	21.6	23.0	22.3	20.7	10.6	7.1
$S/\sqrt{B}$, two cuts, $100 fb^{-1}$	36.3	29.8	29.9	33.1	29.9	24.4	17.8	9.8
$S/\sqrt{B}$, two cuts, $500 fb^{-1}$	59.1	63.3	64.9	61.9	65.6	59.1	32.1	28.1
$S/\sqrt{B}$, three cuts, $500 fb^{-1}$	67.2	56.8	63.2	61.0	65.8	59.1	40.2	28.6

Table 7.19: The significance of the signal for different Higgs masses and when the different cuts are applied. None of the TDR significances are listed here.

We will now dicuss the significances obtained for one cut and two cuts here and in [7]. The significances obtained in this thesis in the case of one cut are found to be a little lower than in [5] and [7]. In [7], PYTHIA 5.7 has been used which operates with a bigger value of the cross section for the signal and lower value for the cross section for the background than in this thesis.

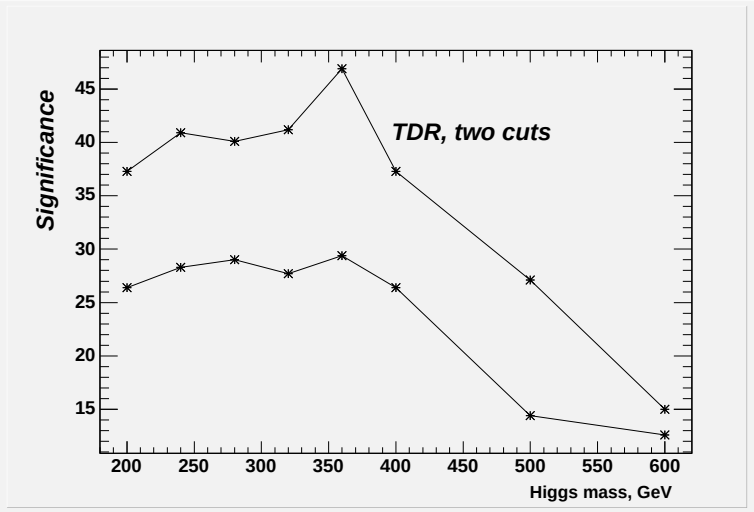

Figure 7.69: The significance from the TDR (above) and obtained here (below) when the p_T cut on the leptons and the Z^0 are applied. The figure corresponds to one year of high luminosity, $100(fb)^{-1}$.

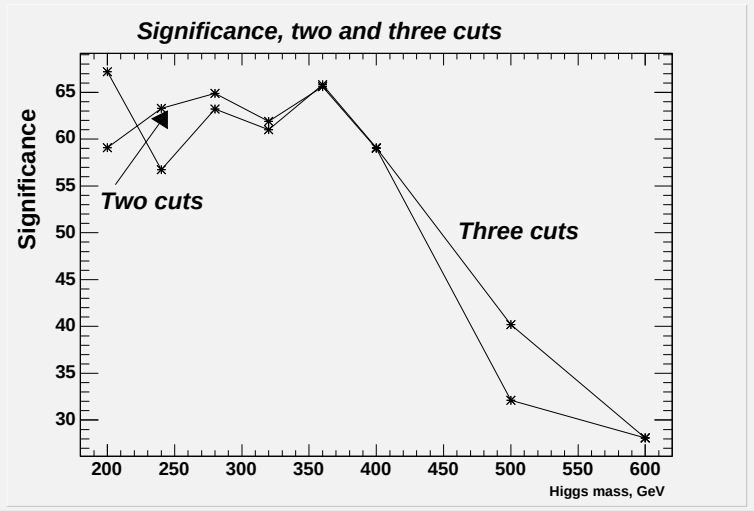

Figure 7.70: The significance obtained when the p_T cuts on the leptons and the Z^0 are applied, denoted 'two cuts'. When the cut on the angle between the leptons is applied as well, a slightly better significance is obtained for some masses.

The values here for the cross section for the signal are $\sim 10\% - \sim 30\%$ lower. For the background, the value of the cross section used in this thesis is $\sim 10\%$ higher.

If we consider the changes in the cross sections, we can make an estimate of how the significances obtained can be scaled to compare with the TDR-results. The results presented here can be multiplied by ~ 1.3 compared to [7]. Besides this, two things are important. The first is that [7] assumes a Gaussian distribution and operates with a 90% efficiency in a mass window of $\pm 1.64\sigma$. This is too optimistic. However, in table 7.11 it was also shown that when the integration procedure was employed $\sim 10\%$ of the signal was lost due to inaccuracies. Some lost significance is regained by keeping this in mind. When this is done, the results are comparable. This can seen from figure 7.68.

In the case where two p_T cuts are introduced, the results obtained here and in the TDR can be compared when we take into account the factors mentioned above. In figure 7.69 the significances obtained here and in the TDR are compared when the two p_T cuts are imposed. The integrated luminosity corresponds to $100(fb)^{-1}$. If the significances obtained in this thesis are multiplied with ~ 1.3, to account for the changes in cross section, we see that much of the lost significanse is regained. When adjusting for the too optimistic TDR result, and the lost efficiency due to integration, even more efficiency is regained.

From figure 7.70 it is seen that the significance is slightly improved when imposing the new cut on the angle between the leptons produced by the hardest of the Z^0 bosons. However, the extra cut did not make a very big difference, due to the correlation between the angle and the p_T.

7.7.3 Discovery Limit

Having found the signal efficiencies, the discovery limit might be calculated for different Higgs masses. The limit is calculated from the expected number of background at some integrated luminosity. When the number of observed events passes the exclusion limit, it can no longer be treated as a fluctuation of the background and when it reaches the discovery limit, a signal is surely seen. Both the required number of events for discovery and the discovery luminosity might be calculated to estimate how long the experiment has to run before discovery. By assuming a mass hypothesis and finding the number of background events in the appropriate mass range, formula 7.6, $N_{s,\,disc} \geq 5\sqrt{bg}$, is used to calculate the required number of signal events before $5\,\sigma$ is reached. In figure 7.71, the discovery limit as a function of Higgs mass is plotted for $200\,GeV < m_H < 600\,GeV$. By using $L_{disc} = \frac{N_{s,\,disc}}{\sigma_s}$ the discovery luminosity is estimated. L_{disc} for several Higgs boson masses is shown in figure 7.72. Since one year of high luminosity corresponds to $100(fb)^{-1}$, we see that the Higgs boson in this mass range will be discovered within a year, using $H \to ZZ \to 4l$ only.

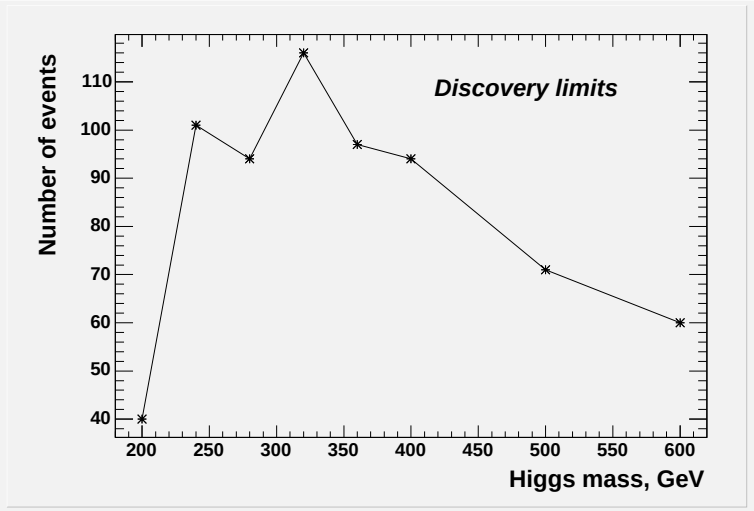

Figure 7.71: The discovery limits as a function of Higgs mass.

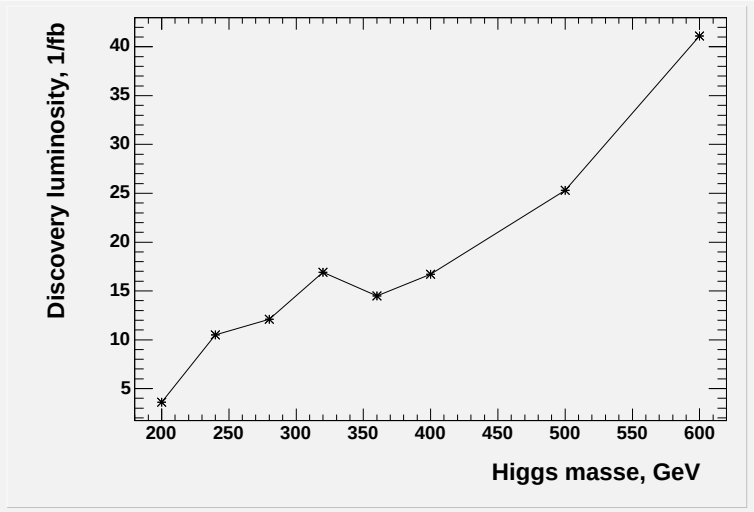

Figure 7.72: The discovery luminosity in $(fb)^{-1}$ as a function of Higgs mass. The Higgs boson will be disovered within on year of full luminosity.

Chapter 8

Conclusions and outlook

In this thesis a study of $H \rightarrow ZZ \rightarrow 4l$ has been presented. The simulation software was PYTHIA on generation level and ATLFAST on detector level. The study was carried out using ATHENA 8.0.5.

The signal and background was first considered separately. It was shown that a sum of Breit-Wigner distribution and a Gaussian distribution best fits the signal mass distribution. For the background, the process $q\overline{q} \rightarrow ZZ \rightarrow 4l$ was generated by PYTHIA. Since PYTHIA does not offer $gg \rightarrow ZZ$, the cross section was multiplied with 1.3 to account for this additional contribution to the background. It was also studied what function that best fits the background when both the cuts proposed by the TDR are applied and the result was that a Landau distribution is the function that gives the best $\chi^2/n.d.f.$

The signal plus background was then generated and drawn in the same histogram for a variety of Higgs masses. The cuts proposed by the TDR were imposed on signal and background to improve the signal to background ratio. To calculate the significance, the signal plus background was fitted with a sum of Breit-Wigner, a Gauss and a Landau distribution. To find the number of signal and background events, the signal+background function was integrated in a certain symmetrical window around the mean value of the simulated signal. To maximise the significance, the range of this symmetrical window was considered separately in each case. The significance was defined as $S = N_s/\sqrt{N_b}$.

The significance was found to be a little lower compared to both [5] and [7]. The reason for this is that the cross sections have changed for Higgs production in PYTHIA 6.1 compared to PYTHIA 5.7 used in [7].
The same cross sections for Higgs production were used in this thesis as in [5]. However, the cross section for background was increased by $\sim 10\,\%$ in this thesis, due to a change in default PDF in PYTHIA.
In [5] and [7] the signicance was estimated by the same formula as in this thesis, but the number of events was found by counting the number of events in a mass window $\pm 1.64\sigma$ around nominal Higgs mass and not by fitting and integrating as done here. The number of events found when integrating is generally lower than found by counting.

The effect of a new cut on the angle between the leptons decaying from the hardest Z-boson was also studied and the significance was seen to improve for all Higgs masses. When this third cut was imposed, the discovery luminosity was also plotted and it was shown that the Higgs boson can be found after less than one year of running at LHC using only the channel discussed in this thesis, if $200\,GeV < m_H < 600\,GeV$, of course.

The existence of the Higgs boson remains the most important prediction of the standard electro-weak theory which has not yet been verified by experiment. When (if) found, the properties of the Higgs particle and its couplings to other particles will have to be determined experimentally. Any deviations from the predictions of the Standard Model will point towards a more complicated Higgs sector than the one described by the Standard Model. And, since the LHC reaches energies beyond the scale of the SM we will in near future see what new physics that hide at higher energy regimes. Different models have been proposed, but only future will show what scenarios emerge at higher energies when the LHC starts.

Appendix A

Higgs simulation Parameters

- PYTHIA 6.221, ATHENA 8.0.5, Hdecay 2.0, ROOT 3.10/01 were used in this thesis.
- In the jobOptions-8.0.5 file, a number of parameters were set:
  - To generate Higgs production, the following parameters were set:
    "pysubs msel 0",
    "pysubs msub 3 1",
    "pysubs msub 102 1",
    "pysubs msub 103 1",
    "pysubs msub 123 1",
    "pysubs msub 124 1"
  - For Higgs decay with subsequent decays of the Z^0 bosons to four leptons:
    "pydat3 mdme 225 1 1",
    "pydat3 mdme 182 1 1",
    "pydat3 mdme 184 1 1"
  - For production of the background process:
    "pysubs msub 22 1"
  - Isr/fsr switches:
    "pypars mstp 61 0",
    "pypars mstp 71 0"
  - Treatment of interference between Z^0/γ^*
    "pypars mstp 43 2"
  - Multiple interactions:
    "pypars mstp 81 0",
    "pypars mstp 82 0"

  - Higgs width:
    "pypars mstp 110 25",
    "pypars parp 110 0.0000001"

- To ensure wanted detector simulation, some parameters were set in AtlfastAlgs/Atlfast_CBNT.txt:

  - GlobalEventDataMaker.Luminosity = 1 or 2;
  - MuonMaker.MuonSmearKey = 3;

  The first parameter sets the luminosity while the second ensures combined detector effort for muons reconstruction

Appendix B

Experimental resolution

In chapter 7, it was discussed how the experimental resolution could be calculated by adding one standard deviation in energy and momentum for each lepton and subsequently take the square root of the sum of the squared mass differences.
The reason it is important to add one standard deviation in energy and momentum at the same time, is that an energy measurement and a momentum measurement is correlated. For muons, the energy is calculated from the momentum. For electrons, there is a momentum measurement from tracking and an energy measurement from the EM calorimeter, but the error in momentum goes like the error in energy above some energy because $E \approx |p|$.
The spread in the mass distribution was calculated using the following expressions:

$$m_H^k = \sqrt{(\sum_{j=1}^{4} E_j + \Delta E_k)^2 - (\sum_{j=1}^{4} \mathbf{P_j} + \mathbf{\Delta P_k})^2} \tag{B.1}$$

and

$$\Delta \mathbf{P_j} = \sqrt{\left(\frac{\partial \mathbf{p_x}}{\partial |\mathbf{p}|} \mathbf{\Delta} |\mathbf{p}|\right)^2 + \left(\frac{\partial \mathbf{p_y}}{\partial \theta} \mathbf{\Delta} \theta\right)^2 + \left(\frac{\partial \mathbf{p_z}}{\partial \phi} \mathbf{\Delta} \phi\right)^2} \tag{B.2}$$

where $k = 1, 2, 3, 4$ and the components of the momentum are given by

$$p_x = p \, sin\, \theta \, cos\, \phi \tag{B.3}$$
$$p_y = p \, sin\, \theta \, sin\, \phi \tag{B.4}$$
$$p_z = p \, cos\, \theta \tag{B.5}$$

The partial derivatives are calculated in ordinary manner. The numerical values for $\Delta\phi$ and $\Delta\theta$ were found in the TDRs.

For electrons:

- $\Delta E \sim \sqrt{E}$

and figure 4-19 on page 115 in [7], volume 1, determines the resolution as a function of energy. The angular resolutions are found on page 110-111 of [38].

For muons: The energy is calculated from $E = \sqrt{p^2 + m^2}$. This gives $\Delta E = \frac{p}{E}\Delta p$ and it can be shown that $\Delta p \sim p^2$. On page 60 of [7], volume 1, the angular resolution for muons can be found and the resolution in momentum can be found in figure 6-17 in the same.

Bibliography

[1] CERN, *The Higgs Boson*, [online] May 2. 2002
`http://www.exploratorium.edu/origins/cern/ideas/higgs.html`

[2] CERN, *The ATLAS experiment*, [online] July 2004
`http://atlasexperiment.org`

[3] F. Halzen and A. Martin, *Quarks and Leptons*, John Wiley & Sons, Inc, ISBN: 0-471-88741-2 (1984)

[4] U. Egede, *The search for a standard model Higgs at the LHC and electron identification using transition radiation in the ATLAS tracker*, Department of Physics, Lund University (1998), ISBN: 91-628-2804-5

[5] B. A. Mohn, *An ATLAS simulation study of Higgs and radions in the* $h(\phi) \to ZZ \to 4l$ *channels*, Cand. Scient. Thesis in Experimental Particle Physics, Department of Physics, University of Bergen (2003)

[6] M. E. Peskin, D. V. Schroeder, *An Introduction to Quantum Field Theory*, Westview Press, 1995

[7] ATLAS Collaboration, Detector and Physics Performance - Technical Design Report, Vol. 1 & Vol. 2, CERN/LHCC/99-15 (1999)

[8] F. Mandl and G. Shaw, *Quantum Field Theory*, John Wiley & Sons (1996)

[9] Particle Data Group, K. Hagiwara *et. al. Review of Particle Physics*, The American Physical Society, 2002

[10] E. Ricther-Was *et. al.* ATLAS Internal Note (1995)[Phys-NO-048]

[11] Matej Batic, *Seminar The Higgs boson*, Ljubljana 2004

[12] Glen Cowan, *Statistical Data Analysis*, Clarendon Press, Oxford, 1998

[13] W.R. Leo, *Techniques for Nuclear and Particle Physics Experiments*, Springer-Verlag, 1994

[14] T.Matsuura, J.J. van der Bij, *Characteristics of Leptonic Signals for Z Boson Pairs at Hadron Colliders*, DESY 91-004, 1991

[15] M. Herrero, *The Standard Model*, arXiv:hep-ph/9812242 v1, December 1998

[16] Bjarte Mohn, Bjarne Stugu, *Corrections to the discovery potential for finding the Standard Model Higgs in the four lepton final state*, ATL-PHYS-2004-014, May 2004

[17] John J. Brehm, William J. Mullin, *Introduction to the structure of matter*, John Wiley & Sons (1989)

[18] Kippe, H, *A simulation study of SUGRA and GMSB signatures in the ATLAS detector at LHC, CERN.*, Cand.Scient thesis, University of Oslo, June 2001

[19] Fuskeland, U.I., *Simulation of a search for the Standard Model Higgs boson in the $H \to \gamma\gamma$ channel at LHC/ATLAS*, Cand.Scient thesis, University of Oslo, June 2002

[20] Peter Zeiler Skands, *L-violating Supersymmetry, Implementation in PYTHIA and LHC discovery potential*,
Thesis for the degree Candidatus Scientiarum in Physics, Niels Bohr Institute, July 2001

[21] T.Sjøstrand, L.Lønnblad, S.Mrenna, P.Skands, *Pythia 6.2, Physics and Manual*

[22] Fabiola Gianotti, *Collider Physics: LHC. Lectures given at the European School of High-Energy Physics, Casta Papiernicka* ATL-CONF-2000-001, 26/04/2000

[23] Rene Brun, Fons Rademakers, *ROOT, Users Guide 3.05*, June 2003

[24] Else Lytken, *Prospects for Slepton Searches with ATLAS*
Thesis for the degree of dr.phil in Physics, Niels Bohr Institute, October 2003

[25] A.Djouadi, J.Kalinowski, M.Spira, *HDECAY: a program for Higgs Boson Decays in the Standard Model and its Supersymmetric Extension*

[26] ATLAS Collaboration, Muon Spectrometer - Technical Design Report, CERN/LHCC/97-22, (1997)

[27] M. Biglietti et.al, *Full Supersymmetry Simulation for ATLAS in DC1*, ATL-PHYS-2004-011

[28] Richard Steward, *ATLAS Software and Higgs Searches via Weak Vector Boson Scattering at the LHC*, 1^{st} Year Transfer Report,
Department of Physics and Astronomy, University College London

[29] Sigve Haug, *Polynomial Discrimination and Weighted Counting in a Standard Model Higgs Boson Search*,
Dissertation for the Degree of Dr.Scient, 2004

[30] André Sopczak, *Complete LEP Data: Status of Higgs Boson Searches*, arXiv:hep-ph/011208v1, 5.th December 2001

[31] G.L. Squires, *Practical Physics*, Cambridge University Press, 1985

[32] L. La Rotonda, E.Meoni, F.Cerutti, *Search for the Standar Model $H \to ZZ^* \to 4\mu$ with multivariate techniques and GEANT3 based detector simulation*, August 2004

[33] B.Mellado, S.Paganis, W.Quayle, Sau Lan Wu, *Analysis of $H \to ZZ \to 4l$ at ATLAS*

[34] Simonetta Gentille, *Search for Higgs Bosons with the ATLAS detector*, ATL-PHYS-2004-009

[35] B.Mellado, G.Unal, Sau Lan Wu, *Higgs Production Cross-Sections and Branching Ratios for the ATLAS Higgs Working Group*

[36] Eilam Gross, Michael Riveline, *Observing the Higgs decay into 4 electrons with the ATLAS detector at the LHC*, September 2004

[37] Ian Hinchliffe, John Womersley, *High Transverse Momentum Physics at the Large Hadron Collider*, LBNL-38997

[38] ATLAS Collaboration, *INNER DETECTOR TDR*,
ATLAS TDR 4, CERN/LHCC/97-16, ISBN 92-9083-102-2 30 April 1997